Design and Experimentation of Composite Packages for Optical Sensor to Measure Strain in Mechanical Structures

Svetlana Spitsina

A Thesis

in

The Department

of

Electrical and Computer Engineering

Presented in Partial Fulfillment of the Requirements
For the Degree of Master of Applied Science
(Electrical and Computer Engineering) at
Concordia University
Montreal, Quebec, Canada

February, 2009

Your file Votre référence
ISBN: 978-0-494-63224-6
Our file Notre référence
ISBN: 978-0-494-63224-6

ABSTRACT

Design and Experimentation of Composite Packages for Optical Sensor to Measure Strain in Mechanical Structures

Svetlana Spitsina

In non-destructive health monitoring of composite materials optical sensors have been shown many advantages compared to the piezoelectrical transducers and electrical strain gauges. Some of their properties include light weight, tiny structures, remote sensing, electro-magnetic interference, and more importantly they are immune to any hazardous environment, particularly they can withstand a high temperatures up to over 1000° C, and they are immune to electro-magnetic interference. They can be easily embedded inside the materials like composites with minimum effect on their original structure.

The light weight of composite materials makes optical sensors embedded in composite package very suitable for many applications including airspace industry. The composite packages can be tailored to achieve desired mechanical characteristics. Moreover, they can be applied as extra protection for embedded fiber optics.

In this work, phase-modulated sensor, Michelson interferometer, was fabricated and embedded in composite package. Then the package was glued on an aluminum substrate. The resultant structure was used to measure strain in the aluminum substrate.

The comprehensive study was performed in evaluating different lay-ups of the

composite package in order to find the best match between the composite materials and the substrate in term of stiffness. ANSYS simulations were performed to study the influence of the resin pocket on the strain transmission to the optical sensor, dependence of the thickness of the adhesive layer on the strain readings on the composite package and on the optical sensor. The results of the simulations showed that optical sensor within resin pocket created by the resin and carbon fiber will give small alteration in strain readings between composite material and optical fiber. Static tensile tests were investigated on different lay-ups of the laminate, adhesives, composite materials, and thickness of the adhesive layers. Difference in strain readings between aluminum and optical sensor were smaller due to good transmission of the strain through epoxy adhesive layer with thickness a 100 μm. The most successful lay-ups for composite package were [90/90/F(0)/90/90] for CYCOM5276-1 and for NCT301 - [90/90/F(0)/90/90] and [-60/60/F(0)/60/-60]. The results showed that composite packages with less stiffness in x direction demonstrated better performance.

ACKNOWLEDGEMENTS

Special thanks are given to Dr. Mojtaba Kahrizi of Electrical and Computer Engineering Department, and to Dr. Suong V. Hoa of Mechanical Engineering Department, for their supervising and devoting instructions during the entire project.

I thank and acknowledge the technical assistance I received from Dr. Ming Xie, Mr. M. Mourtazov, .Mr. Heng Wang, Mr. D, Cree, Dr. B. Zhang, Dr. Ramin Banan Sadeghian, Dr. B. Hraimel. I would also thank Dr. M. Pugh, and Dr. X. Zhang for facilitating to use their labs to carry some of the experiments done in this work.

I would like to give special appreciation for my mom and my son who were helpful and understanding during the time of my work.

TABLE OF CONTENTS

LIST OF FIGURES

LIST OF TABLES

CHAPTER 1

INTRODUCTION

Overview of composite packages, sensors for mechanical structures for damage detection, fiber optic sensor technologies, and clarification of the context arrangement in this thesis will be presented in this chapter.

1.1 Composite packages

Previous research in the field of composite packages was conducted with the aim to protect the optical sensors, and improve their outputs. A patent was published by Alexander L. Kalamkarov and Stephen Bruce Fitzgerald [1] for creating the composite package for optical sensor. Composite carrier was elongated rod including fiber optic strain gauge embedded during the pultrusion process, during the curing of the resin within the heated die. Shape can be curved or has other non-linear form by using fiber holder with predefined lateral cross-sectional form. The structure can be reinforcing bars or prestressing tendons for bridges and other types of construction. Figure 1.1 illustrates this composite carrier assembly.

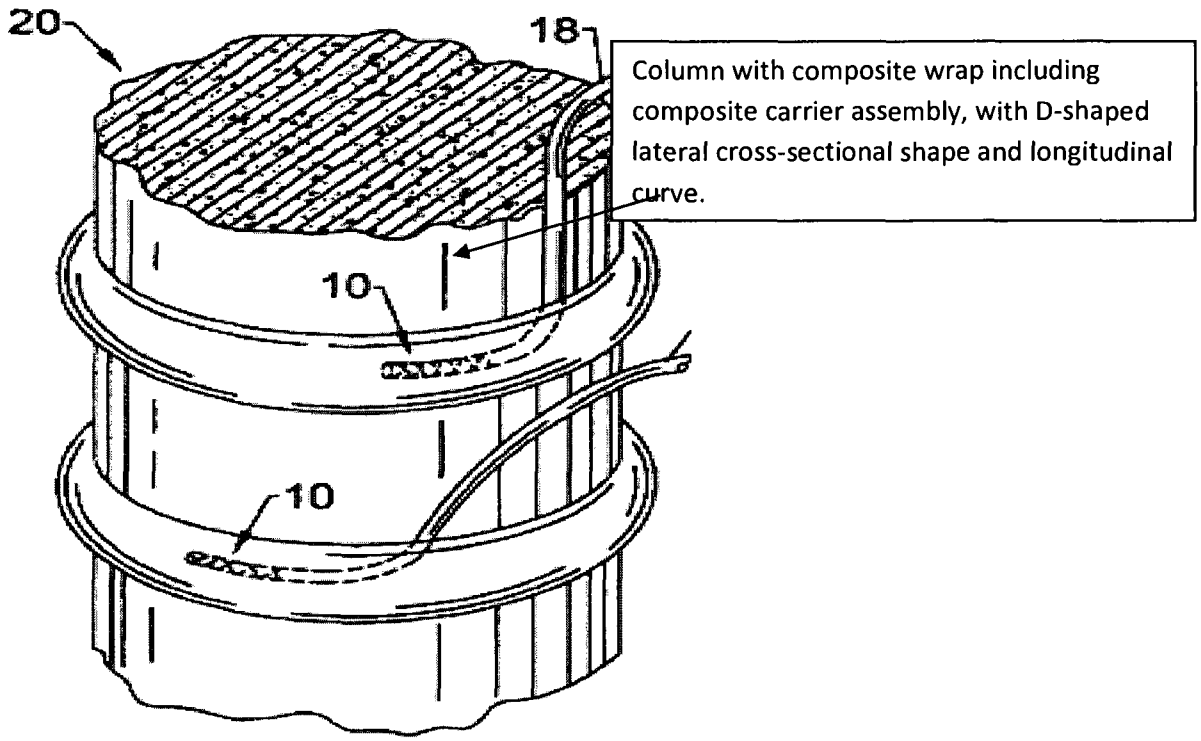

Figure 1.1. Application for composite carrier assembly with embedded optic sensor: 10) a composite carrier assembly within structural element; 18) optical fiber extended outwardly; 20) D-shaped structural element [1].

This composite carrier assembly has disadvantages. First disadvantage is decreased efficiency; the bending of the sensor is the reason for power loss. Second disadvantage is high cost, all assembly was connected together and if one sensor is out of order all assembly should be changed, a lot of composite material was used to fabricate the assembly for mechanical structure. Third disadvantage is versatility, the rod with optical sensors cannot be applied on mechanical structures with different surface geometry, it can be applied only on flat construction surfaces. The next patent was published by Peter

C. Ogle, CIDRA Corporation [2]. Package from a resin system with KEVLAR fiber reinforcement consisted of layer of contrahelically wound braided reinforcement at 45° angle and further reinforced with fiber placed in parallel with optical sensor. Wrap resisted the changes in wavelength shift due to the changes in temperature. The package was stiffer than optical fiber, and optical fiber followed the changes due to temperature in this athermal packaging which had a negative coefficient of thermal expansion - $8*10^{-6}$/°C. Primarily, optical sensor embedded in parallel with reinforcement. Then layer of contrahelically wound braided reinforcement at 45° angle to optical fiber. Reinforcement provided stiffness to bending of the optical fiber with Bragg grating and contracts in length as the temperature increases to maintain the center wavelength of light reflected by Bragg grating within tolerable limits. Reinforcement can be Kevlar or graphite, because they have negative coefficient of thermal expansion. Packaging was 1.5 mm in diameter and 50 mm long. Coefficient of thermal expansion can be tailored by changing the angle of the contrahelically wound fibers and the amount of longitudinally disposed fibers in athermal-packaging design.

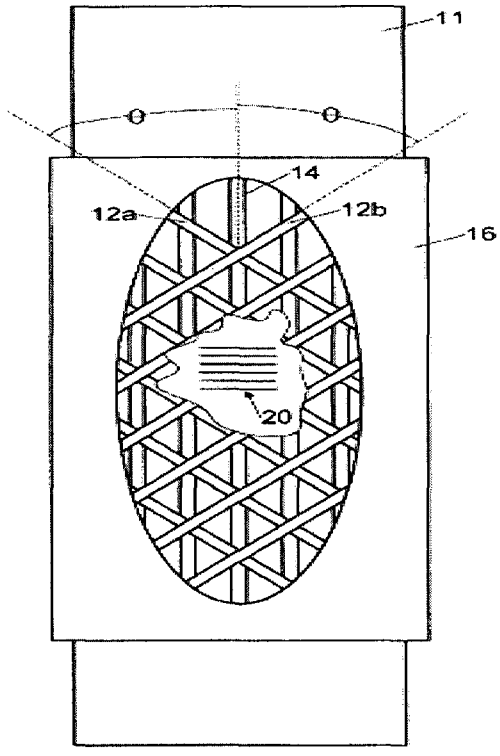

Figure 1.2. Athermal packaging with optical sensor inside: 11 is optical fiber; 12a and 12b are contrahelically wounded braided reinforcement at θ angle; 14 is reinforcement along the optical fiber; 20 is Bragg grating; and 16 is athermal packaging [2].

One of the disadvantages of this package is that fabrication of such package is complicated due to the small size. Finally, D. Roberts in his paper [3] described packaged fiber Bragg grating optical sensor which is used in oil and gas industry. Optical strain gauge embedded inside glass/epoxy composite carrier was used for riser monitoring on the deep water applications in the Gulf of Mexico, to record the shape of flowline buckle

regions, to determine fatigue and remaining lifetime; in addition, sensing carrier with embedded optical sensor recorded pressure measurements of flowlines. This sensor has been fabricated specifically for described application and cannot be used in other applications due to specific shape. B. Glisic and D. Inaudi [4] proposed sensing tape which consists of glass fiber thermoplastic composite and polyimide coated optical fiber. Optical, microscopic, and mechanical tests illustrated good performance but improvements in fabrication should be done in order to control the placement of the optical fiber to avoid optical losses. Mechanical tests showed good agreement in measuring strain between sensing tape and micrometer, and that sensing tape can be used as deformation sensor. On-site tests on rails (surface installation) and high-pressure vessels (embedding) confirmed the adequate sensing performance of the sensing tape and its applicability in real conditions. The glass fiber composite is more fragile than carbon fiber reinforcement and will be worn out faster than proposed package from composite material with carbon fiber reinforcement. In addition the weight of the glass fiber is higher than the weight of the carbon fiber. This mechanical characteristic will be important in airplane industry and in space applications.

1.2 Different types of sensors

Sensors that detect damages in mechanical structures can be electrical, optical, mechanical, and acoustical. Extensiometer is the mechanical sensor that provides low resolution. It is bulky, and difficult in applications. Piezoelectric transducers and electrical strain gauges are usually applied for health monitoring of mechanical structure.

However, these sensors have disadvantages such as corrosion and electro-magnetic interference.

1.2.1 Acoustic emission sensor.

Acoustic emission, AE, piezoelectric sensor is the sensitive sensor used for health monitoring of the structure. The active element of a piezoelectric transducer is a thin disk of piezoelectric material which converts mechanical deformation into electrical voltage. The disk is metalized on both faces for electrical contact, and mounted in a metal cylinder to provide electromagnetic interference shielding. The piezoelectric ceramics used in AE transducers are made of small crystals of titanates and zirconates which are mixed with other materials, molded to the desired shape, and fired in a kiln. The ceramic material is then made piezoelectric by poling, which is the process of heating the material above its Curie temperature while the material is in a strong electric field. The piezoelectric transducer should be attached to the material with minimum loss at the transducer-material interface using the thin films of grease, oil, or epoxy adhesive. The coupling medium must be sufficiently viscous to support the shear motion. The purpose of a couplant is to insure good contact between two surfaces on a microscopic level. Bonding agent should be able to hold the sensor on [5]. M. Liu *et al* [6] explored properties of the piezoelectric material adhesively bonded to aluminum structure. They evaluated effect of the length of the crack, thickness of adhesive and thickness of piezoelectric layer on crack driving forces. Simulations showed that under cyclic electric potential loading the crack propagation reached a steady state as the crack moved out of the edge zone, and a

thicker adhesive layer reduced the apparent interface toughness. Three-dimensional analysis showed larger energy release rate values than that of plane strain solution due to the bending deformation in the out-of-plane direction.

Piezoelectrical transducer with built-in preamplifier, R15I-4851, is one of the examples of narrow band piezoelectrical transducer which is used for composite structures such as thermoset and thermoplastic. Figure 1.3 represents the integral preamplifier AE sensor.

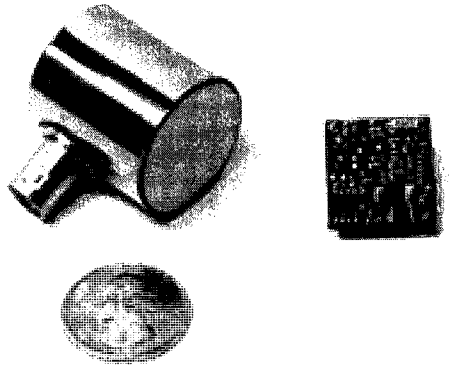

Figure 1.3. Integral preamplifier AE sensor/Physical Acoustic Corporation/.

1.2.2 Electrical strain gauge.

Electrical strain gauge is another sensor used in non-destructive health monitoring. Electrical strain gauge measures strain of the mechanical structure using dependence of resistance variations due to induced strain. Figure 1.4 shows schematics of electrical strain gauge.

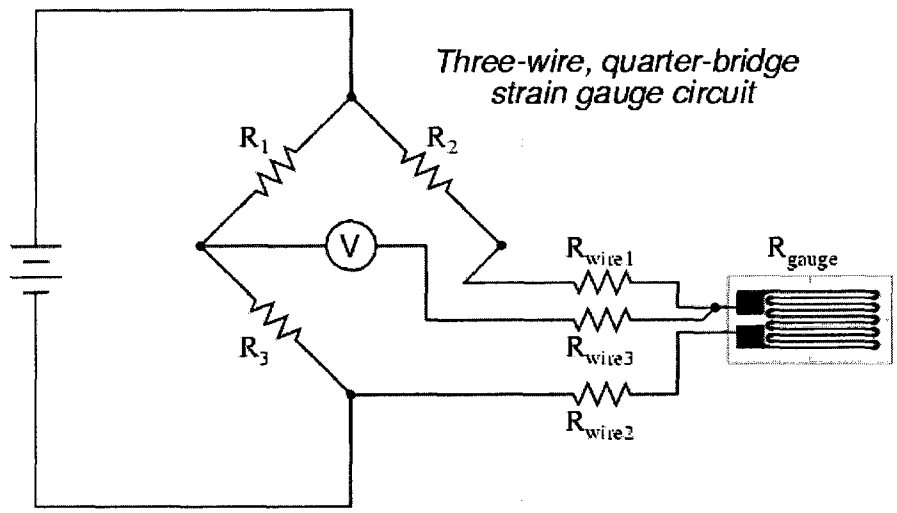

Figure 1.4. Electrical strain gauge [7].

Strain gauges convert mechanical motion into electrical signal. Gauge factor, GF, is the strain sensitivity. Strain gauge sensitivity is proportional to change of the resistance divided by initial resistance and inversely proportional to mechanical strain. Strain gauge readings depend on the temperature, adhesive, material, and bonding to the surface.

1.2.3 Optical sensors.

Optical sensors have light weight, immunity to electro-magnetic interference, capability for distributed and multiplexed operation, high sensitivity and accuracy, and dynamic range. Different types of optical sensors can be applied to the mechanical structure to measure strain where the relationship between stress and optical effect is applied (stress-optic law). However, optical sensors are fragile and need to be protected. Embedded optical sensors can be solution for industrial applications. But embedding of

optical fiber alters properties of the fiber and composite structure where fiber was embedded, and special processing conditions are required for material fabrication. Influence of optical fiber embedded inside composite material was investigated by I. Balać *et al* [8] where theoretical results for optical fiber embedded inside laminate under transverse loading showed that optical fiber did not generate significant stress, and could be used as sensor embedded inside composites without significant decrease of the host structure's strength. Neglecting strain in z-direction yields 2D plain strain case, and due to the symmetry a quarter of the analytical model was used. Numerical calculations with data for single mode optical fiber embedded inside 1mm thick composite, graphite/epoxy, for applied stress in x-direction were compared with finite element method (FEM). Optical and graphite fibers were aligned in the same direction. Results for radial and tangential normal stress, along x and y axes showed that embedded optical fiber increase to 40% stress in its vicinity for transversal loading. Peak values were observed in some distance from the interface between optical fiber and composite host. However, results showed that optical fiber did not generate significant stress, and could be used as sensor embedded inside composites without significant decrease of the host structure's strength.

Different designs of the lay-up in smart structures were fabricated and tested for embedded optical sensors, and optimal laminate was where layers of composite were in the same direction as optical fiber.

Alternative way is fabricating the packaged sensor network which could be applied on the mechanical structure in order to detect cracks. Packaged optical sensor is capable to detect mechanical strain and acoustic emissions.

1.3 Fiber optic sensors

Fiber optics became very popular since the optical fiber started to be affordable. Optical fiber is the main component in communication and sensor networks. Moreover, it is an environmentally clean solution for telecommunication and sensor applications. Optical fibers can be multimode or single-mode type. Single mode fibers have more loss due to propagation of light into the cladding, causing evanescence wave to occur. Commonly, single-mode fiber has a core with 8 to 10 micrometers diameter. Single-mode fiber transmits infrared laser light at 1300 nm and 1550 nm wavelengths with minimum loss [9]. Cladding in optical fiber provides internal reflection because its reflective index is slightly less than reflective index in core. Buffer coating is protective plastic coating that protects fiber from damages and moisture. Figure 1.5 presents single fiber structure including core, cladding, buffer, and jacket.

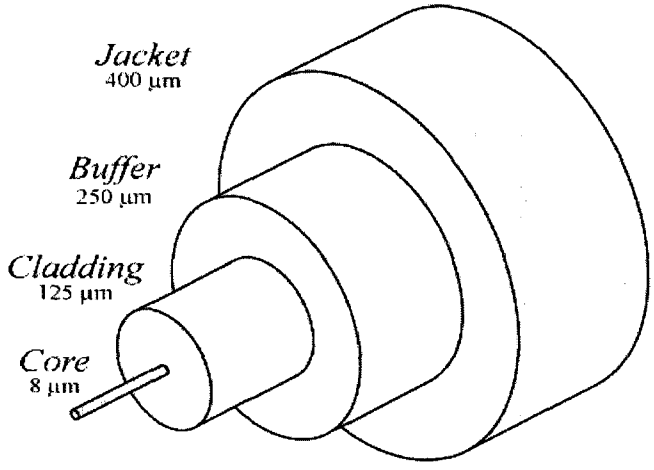

Figure 1.5. Single-mode fiber structure [10].

Plastic fibers have the biggest diameter around 1 mm and transmit visible lights. A multimode fiber has a core with typically 62.5 micron in diameter and usually transmits infrared light at 850 nm to 1300 nm [9]. Fibers can be multimode or single mode. The multimode fibers may have step index or graded index of refraction. Singlemode fibers have step index of refraction. Figure 1.6 illustrates structural properties of various types of optical fibers such as index of refraction, light propagation inside the fiber and input and output pulse.

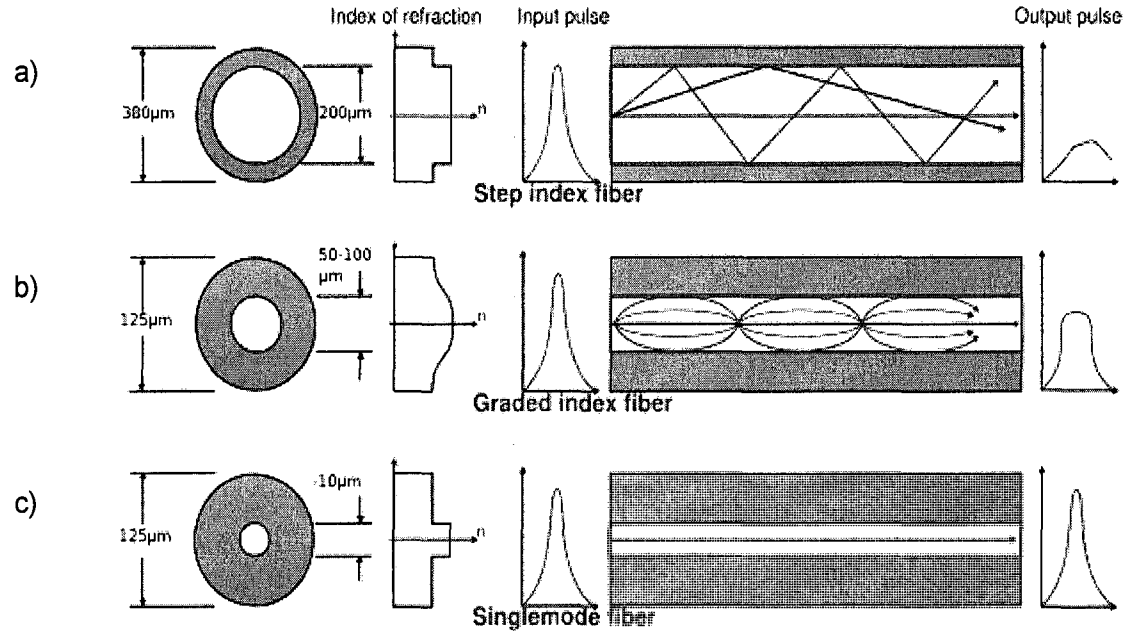

Figure 1.6. Optical fibers: a) multimode step index fiber; b) multimode graded index fiber; c) single mode step index fiber [11].

Fiber optical systems were developed rapidly in the last decade due to the numerous advantages like small size, passive, low power, resistant to electromagnetic interference, high sensitivity, wide bandwidth, and environmental insensitivity, low cost, absence of Joule heating effects as in electrical strain gauges. Fiber optic sensors replace recently traditional sensors for sensing rotation, acceleration, electric, magnetic field measurement, temperature, pressure, acoustics, vibration, linear and angular position, strain, humidity, viscosity, and chemical concentration measurements. Optical fiber sensors measure environmental conditions such as strain, temperature, magnetic, and electric fields, acoustic waves, and chemical concentrations by determining the induced changes in the intensity, phase, wavelength, polarization, time domain characteristics and modal content caused by such external phenomena. Some of the examples of optical sensors are intensity-modulated and phase-modulated (Mach-Zehnder, Michelson, Fabry-Perot, Sagnac, and FBG, fiber Bragg grating) sensors. Optical sensors can be extrinsic and intrinsic devices. Extrinsic device is where light exits the fiber, interacts with the environment, and re-enters the fiber. Intrinsic device is where light remains within the fiber along the entire operations.

Variety of the optical sensors is available for health monitoring of the mechanical structures. The descriptions of the different type of the sensors, their sensitivity, various detection schemes, and tradeoffs between them were presented by T. G. Giallorenzi *et al* [12].

Various types of sensors are summarized as follows:

- Intensity based sensors include numerical aperture sensors, linear position sensors, sensors based on total refraction, evanescence based optical sensors, microbend fiber sensors, Figure 1.7 illustrates these sensors.

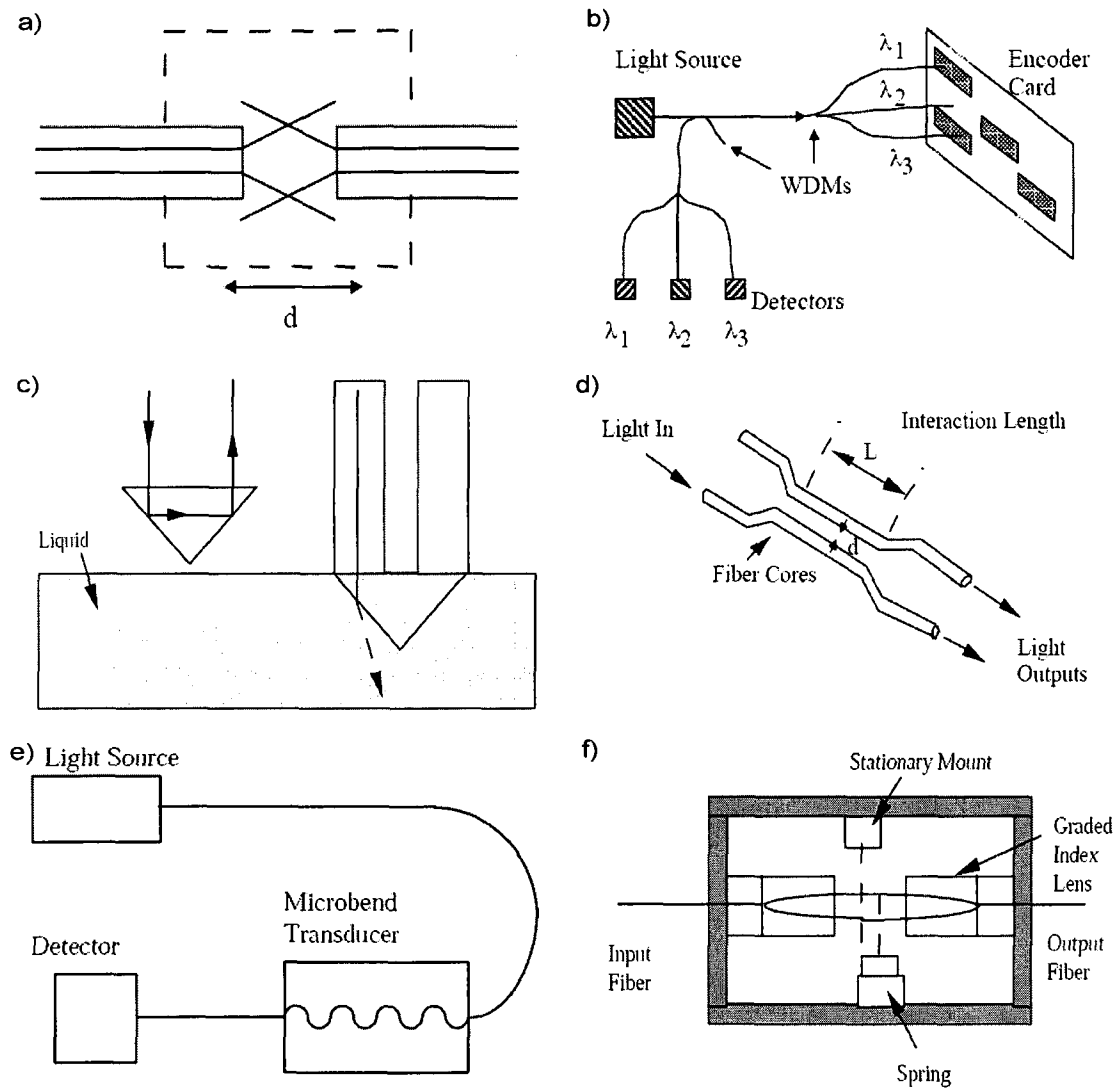

Figure 1.7. Intensity-modulated sensors: a) numerical aperture sensor; b) linear position sensor; c) sensor based on total internal refraction; d) evanescence based fiber optic sensor; e) microbend fiber sensor; f) grating based intensity sensor with graded index lens [13].

Numerical aperture sensor measures vibration: two tips of fiber placed with distance "d" with aligned cores. When vibration appears cores are misaligned and output power will be smaller than before, higher misalignment - higher power loss. Linear position sensor based on wavelength division multiplexing decodes position by measuring the presence or absence of reflective patch at each fiber position as the card slides by via independent wavelength separated detectors. Time division multiplexing can be used for linear position sensor where different lengths of the fiber are applied. The output will reflect the net result of the position on encoder card where time delay corresponds to different fiber. Next intensity sensor is sensor based on total internal refraction. It detects presence or absence of the liquid. Reflective prism reflects the light back to the fiber but light will leak into liquid when liquid level hits reflective prism [13]. Evanescence based fiber optic sensor detects temperature, pressure, or strain. Cross coupling of light between two fiber cores appears when temperature, pressure, or strain influences on fiber. The distance between fibers increases and the amount of cross coupling decreases. Microbend sensor can be used instead of evanescence based fiber optic sensors. Bent fiber has the radius which exceeds the critical angle to confine the light inside the core, and light penetrates the cladding. Grating based intensity sensor with graded index lenses measure vibration or acceleration via shutter effect. The input light is collimated into a parallel beam with graded index lens (quarter pitch lens) and passes to output graded index lens (0.29 pitch lenses) which focus the light into core of the output fiber. One of the gratings is fixed and another one moves. The intensity output will be changed due to the change in position of the moving grating [13].

- Spectrally based fiber optic sensors include sensors based on blackbody radiation, absorption, fluorescence, etalons and dispersive gratings, Figure 1.8 shows these sensors.

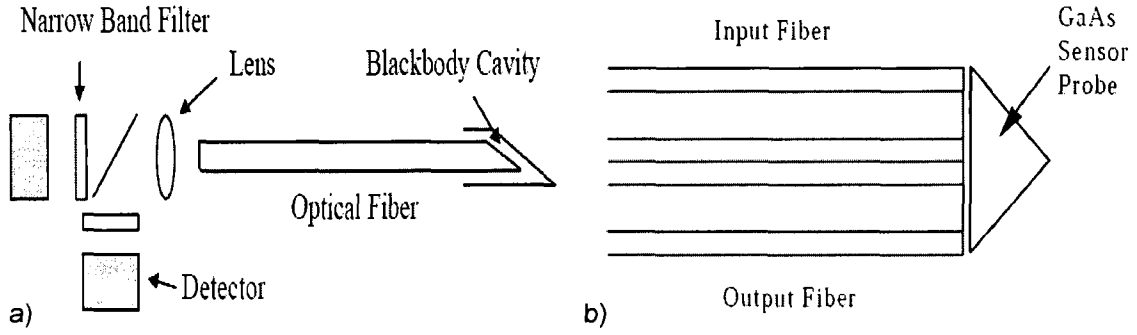

Figure 1.8. Spectrally based fiber optic sensors: a) blackbody sensor; b) absorption based sensor [13].

Blackbody sensor detects temperature due to cavity glows and acts as light source. For each temperature output intensity is different. Absorption based sensor is temperature sensor as well. GaAs sensor probe, broadband source and input, output fibers are components of this optical sensor. The effect where transition wavelength of GaAs depends on temperature is used in this sensor.

- Phase-modulated sensors such as Mach-Zehnder, Michelson, Fabry-Perot, and Sagnac interferometers. The idea of the phase-modulated sensors is the use of two single-mode fibers where one fiber is the sensing and another is the reference. The change of the phase in sensing fiber is used to measure a phase shift due to environment perturbs. The following schematic, Figure 1.9, represents the optical sensors.

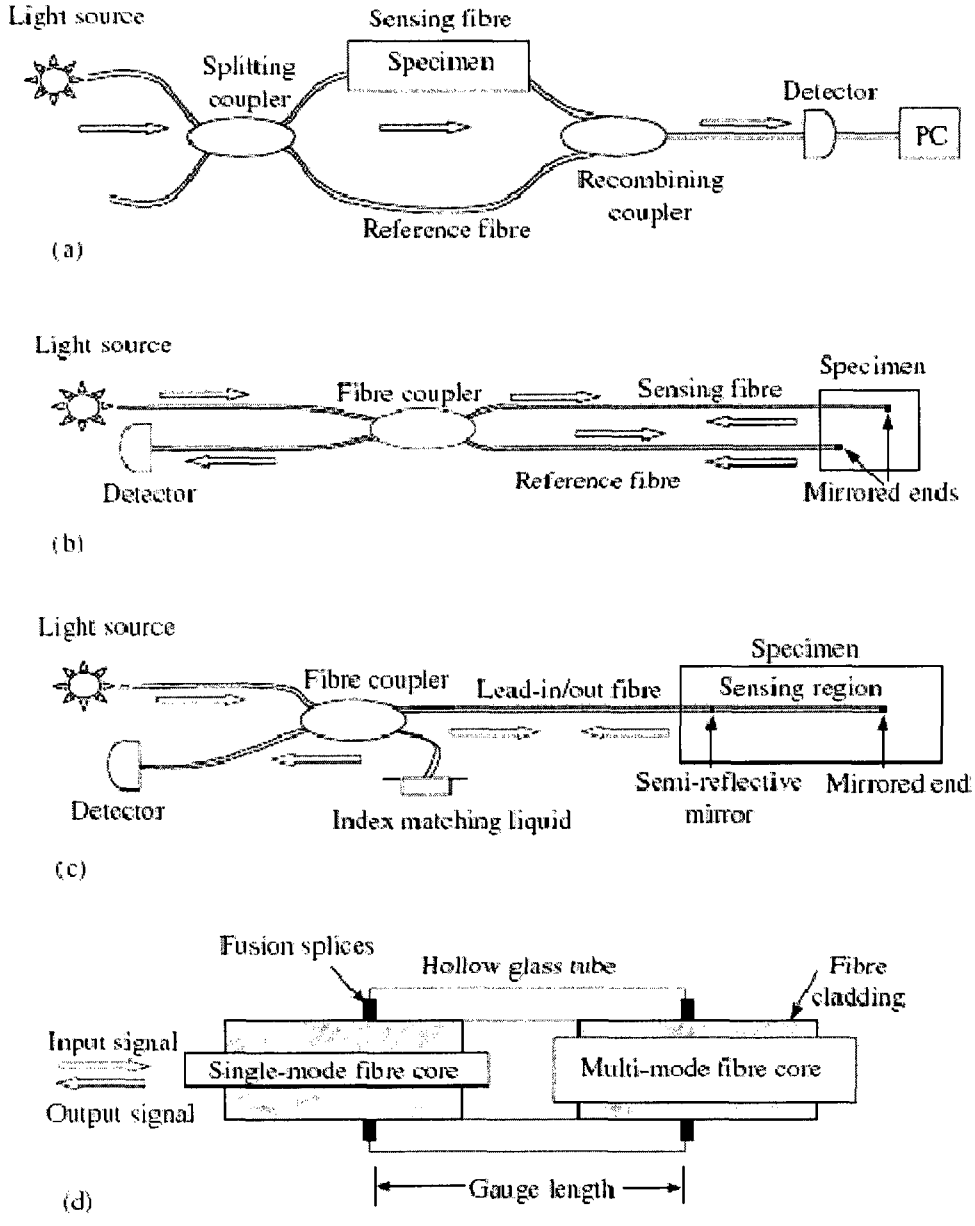

Figure 1.9. Schematics of interferometric sensors: (a) Mach- Zehnder, (b) Michelson, (c) intrinsic Fabry-Perot, and (d) extrinsic Fabry-Perot [14].

Mach-Zehnder interferometer has sensing and reference arms. The light is coupled to arms, phase in sensing arm was changed due to the temperature, vibration, strain, and pressure and when the light from reference and sensing arms coupled together to the

output phase shift will cause in power output change. Michelson interferometer is based on the phase shift principle as well. Figure 1.10 illustrates Michelson interferometer with embedded sensing arm.

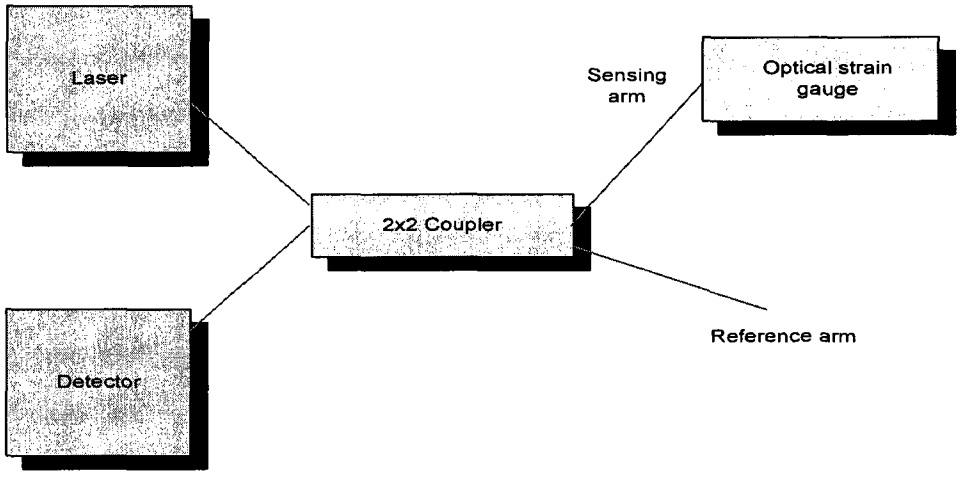

Figure 1.10. Michelson all optical fiber unbalanced interferometer.

This sensor will be used in present work for strain detection. Only one coupler is needed in this design due to the mirror ends in sensing and reference arms. Intrinsic Fabry-Perot has change in power output due to the change in length between semi-reflective and reflective mirrors. Extrinsic Fabry-Perot interferometer has air gap between singlemode input and multimode reflector. The distance between two fibers will change due to temperature or strain and resulted phase shift will generate change in power output.

Previous research on Michelson interferometer was reviewed for implementation. This research includes the papers that illustrate the abilities of the interferometers to detect pressure and temperature [15], strain [16]; the single mode all fiber Michelson

interferometer with phase compensation by the control of laser frequency was reported by Kashyap and B. K. Nayar [17].

R.D. Turner *et al* [18] defined specific requirements for optical sensors and criterias for smart structures applications. Polarimetric, interferometric, and modal sensors were defined, high-birefringence polarimetric and localized Michelson sensors were applied for strain readings; finally, strain sensitivities were obtained from experiments where high sensitivity was experimentally obtained from localized Michelson interferometer [18]. Optical spectrum analysis was performed using Michelson interferometer where piezoelectric translator was used to stretch the fiber; the limitations of the measuring the strain was 10^{-4} according to the linear Hooke's region of the fiber reported in article K.-J. Krath *et al* [19]. L. Yuan *et al* [20] represented theoretical calculations and tensile tests results for detection of strain/damage in composite using Michelson interferometer. The dependence of the sensitivity coefficient of the fiber-optic sensor from the fiber gauge length of the interferometer was obtained.

T. Valis *et al* [21] studied localized Michelson interferometer: theoretical calculations of the strain were shown, surface-adhered and embedded in composite sensors were used for detection of the strain and acoustic emissions, strain values were comparable with electrical strain gauge. A Mach-Zehnder interferometer was used by N. Narendran *et al* [22] to record the fracture: sensing arm was embedded in Plexiglas in-plane and transversely to determine the stress-intensity factor. Michelson interferometer was developed for detection small ultrasonic displacements in the presence of much larger mechanical vibrations in monitoring the state of wear in machine tools by R. McBride *et al* [23]. Tests on static workpiece and rotating tool holder during face milling

of mild steel were performed to detect AE, and results were compared with piezoelectric transducer outputs. Damage monitoring was performed with localized MI by I. B. Kwon *et al* [24]; different laminate lay-ups and different length of the strain gauge were used for detection of strain and AE waves. H. Tsuda *et al* [25] recorded impact and tensile tests with MI placed on the unidirectional laminate. Fast Fourier transform and digital filter processing of the optical signal were performed to detect strain and AE waves; damage monitoring using MI mounted on the composite structure showed comparable results with electrical strain gauge and piezoelectric transducer. Another article of H. Tsuda *et al* [26] illustrated response of the Michelson interferometer to AE simulated by pencil lead break, where MI was placed on carbon fiber reinforced plastic, and its response for AE was compared with piezoelectric transducer. S. L. Loret *et al* [27] demonstrated demodulation technique for unbalanced MI with measurement range 10 mm where dynamic response of the structure through modal analysis was evaluated.

- Fiber Bragg grating, FBG, sensors can be used for strain and temperature measurements. Change in the axial direction or thermal expansion causes the alteration in grating spacing and reflective index, and wavelength of the reflective wave changes [28]. Figure 1.11 presents optical network for FBG sensor.

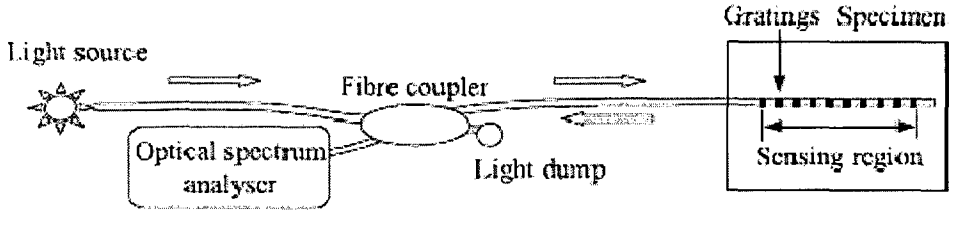

Figure 1.11. Schematics of Bragg grating sensor [14].

Bragg grating sensor changes the reflected wavelength due to the change in space between the gratings and refractive index. Optical sensor based on Bragg grating can be used to detect temperature, strain, and acoustic emissions. Bragg grating can be used as filters. Y. Zhao and Y. Liao summarized the methods to achieve the strain and temperature readings using FBGs [29], and overview for FBG sensors such as their fabrication, theoretical calculations of strain and temperature, and applications were illustrated [30].

- Faraday rotators, fiber laser sensors, and integrated optical MEMS (Micro-Electronic-Mechanical-System) sensors are other examples of the optical sensors.

To measure strain in the mechanical structures optical sensor can be placed on the structure, inside it, or embedded inside the composite packaging in order to protect optical fiber from hostile environment. Optical sensors recently started to replace the electrical and mechanical sensors which are used in industry for damage detection and for non-destructive evaluation.

1.4 The placement of the optical sensor

The placement of the optical sensor on mechanical structure is important for detecting errorless signal without damaging the optical sensor and without diminishing the mechanical properties of the structure. Optical sensor can be bonded to the mechanical structure with adhesive film, epoxy resin, or cyano-acrylate bonding agent. N. Fürstenau et al [31] recorded in-flight strain measurements where double-polarization Michelson interferometers with balanced interferometer arms of 5 cm sensing length

where bare sensing arm was adhered on the composite plate eight-layer laminate [±30°] with width 5 cm. Then this plate was applied on aircraft wing structure, and optical strain gauge was tested on the ground and during the flights.

Optical sensors were designed for applications where they were embedded inside composite structure, smart skins. Comprehensive testing for embedded optical fibers, which were placed along and perpendicular to loading direction and in configurations both symmetrical and asymmetrical respective to the midplane inside graphite/bismaleimide laminate with $[0_3,90_2,0]_S$ lay-up were performed by D. W. Jensen *et al* [32, 33]. Their test results showed that tensile strength and stiffness were not significantly degraded (1% to approximately 10%) due to embedded optical fibers, but compression test results in ref. [33] represented compressive strength and stiffness reductions up to 70% and 20%, respectively. From these results it could be seen that compressive strength and stiffness were sensitive to orientation of the optical fiber with respect to the loading direction. The samples with optical fibers placed perpendicular to loading direction and reinforcement exhibited the maximum reduction in compressive strength. M. Surgeon and M. Wevers [34] reported static and dynamic mechanical tests with composite specimen where optical fibers were embedded inside laminate with $[0,45,-45,90]_S$ lay-up. From the results of mechanical tests authors determined an optimal optical fiber configuration where optical fiber was embedded in 90/90 interface, because this configuration showed a minimum influence on mechanical properties.

Because optical fiber can change mechanical properties of the composite structure and in order to protect it from hostile environment for applications on the mechanical

structures packaged optical sensors were fabricated and tested in order to determine the credibility of these sensors.

From previous research it is evident that packaged optical sensor will find numerous applications. Optimal design of the package for optical sensor is the ultimate goal for research. Impregnated inside carbon/epoxy composite carriers optical sensors can be used for fatigue testing of aircraft components such as frames, stringers, and rivet rows in the skin of wings. Interferometric strain sensors can be used for the detection of dynamic and static strain.

1.5 Advantages of composite package for optical sensor

The advantages of packaged sensors are that optical sensors do not damage the mechanical structure, and they are protected from hostile environment with composite package, these sensors are cheap and inherit all advantages of the other optical sensors such as small size, light weight, passive, low power, resistant to electromagnetic interference, high sensitivity, wide bandwidth, and environmental insensitivity, low cost, absence of Joule heating effects as in electrical strain gauges; inexpensive nondestructive technique can be used to evaluate the performance of the mechanical structures using these composite carriers with optical sensors inside.

1.6 Scope and objectives of the thesis

Present work proposes the new fabricated packaged optical sensor for detection of the mechanical strain in aluminum. Optimal design of the composite package with embedded optical sensor was determined for applications on the mechanical structures. The scope of this thesis includes design, fabrication, tensile tests, microscopy results, and simulation results using ANSYS. First, fabrication of the composite packaging was performed according to the guidelines in ref. [35] observed for quality and resin pocket. Second, ANSYS simulations were performed based on microscopy results. The resin pocket size was studied in ANSYS. Third, to conclude which lay-up for the package design and which adhesive as well as which thickness of the adhesive layer will be the most appropriate for practical applications the static tensile tests were performed using aluminum samples with attached packaged optical sensors. Third, the finite-element analysis using ANSYS software was performed based on microscopy results from samples utilized for tensile tests to analyze the optimal carbon/epoxy packaging with embedded optical fiber in terms of different adhesive thickness, diverse laminate lay-up of composite carrier and mechanical properties of the composite material used for fabrication of the composite carrier, and strain concentration. Strain values from simulations were compared with the strain readings from tensile tests.

The objective of this thesis is to develop design of the most advantageous composite package for optical sensor which can be used for strain readings in mechanical structures. Therefore, this thesis consists of three aspects of research:

(1) To study strain transition from composite package to the optical sensor for different configurations;

(2) To study response of the optical sensor embedded in composite package;

(3) To propose an optimal design of the composite package for the fiber optic sensor.

1.7 Organization of the Thesis

Chapter 1 provides brief introduction about the sensors available in the market for mechanical structures damage evaluation, the scope and objectives of this thesis. Chapter 2 discusses theoretical calculations for determination of the strain using Michelson interferometer and background on the design with composite materials for four package designs. Moreover, investigation of dependency of the strain in optical fiber on the different geometries of the resin pocket and the adhesive layer were simulated by using ANSYS. Chapter 3 describes fabrication of the composite carrier with embedded optical fiber, experimental set up for tensile tests, test results, and microscopic results. Chapter 4 illustrates the simulation results for different lay-up of composite carriers, and different composite material that were performed in ANSYS. Chapter 5 discusses comparison between experimental results and ANSYS simulations. Chapter 6 consists of summary of the work, recommendations for optimal design and future work.

CHAPTER 2

THEORETICAL BACKGROUND

This chapter introduces packaged optical sensor, Michelson Interferometer (MI), and Fiber Reinforced Composite Material (FRCM) that was used for optimal design of package.

Fiber reinforced plastics which were used for fabrication of the package have good performance in terms of superior specific strength, rigidity, and light weight. They are widely used in aerospace, chemical, building, and automobile industries. Composite structure consists of matrix part, epoxy, and reinforced part, fiber (carbon, glass). To investigate the damages of this material is complex and consists of three modes such as matrix cracks, delamination, and fiber breakage. Non-destructive evaluation technique is the non-expensive evaluation of the composite structure. Electrical and optical sensors are used for non-destructive evaluation of composite structures such as piezoelectrical transducers, PZT, electrical strain gauges, ESG, optical polarization sensors, fiber Bragg grating, FBG, phase-modulated sensors such as Michelson interferometer, Mach-Zehnder, Fabry-Perot, and Sagnac.

Compare to other type of sensors, fiber-optic sensors have some advantages, such as light weight, immunity to electro-magnetic interference, and ability to measure different physical parameters using one probe, corrosion resistance, offering electrical isolation, remote sensing, and they can withstand high temperatures.

Michelson unbalanced interferometer was used to fabricate a novel design of a package in order to monitor the mechanical structures. The packaged sensor was connected to the aluminum sample, and the output signal was recorded. The optical phase shift modulation of the light in the signal arm, in sensor gauge, resulted due to induced strain in the sensor gauge. The intensity of the light from sensing arm was mixed with the light from the reference arm in the output of optical fiber coupler. From strain sensitivity of the optical sensor mechanical strain was obtained and compared with the readings of electrical strain gauge in tensile test where axial stress was applied on aluminum sample.

Theoretical background on all-fiber Michelson Interferometer and composite material, thermoset, is presented below. Theoretical measurements of strain and temperature for Michelson Interferometer and mechanical properties of four different designs of laminates in composite carriers are illustrated.

2.1 Michelson Interferometer

As it was discussed in the introduction the interferometric sensors can be intrinsic or extrinsic, and the phase difference is determined by comparing phases of the sensing and reference fibers.

Michelson interferometer is one of the examples of the phase-modulated sensors. This sensor is very sensitive, all-fiber, easy to construct and embed inside composite material. It employs a laser light source, 2x2 coupler, optical spectrum analyzer, and two single-mode fiber arms, sensing and reference. The light is divided and injected into each fiber arm. Then wave propagates along the sensing and reference arms and reflects back to the

coupler due to the mirrored tips. Finally, reflected light recombines in coupler, and splits back to laser source and to optical spectrum analyzer. Figure 2.1 represents schematic of a Michelson interferometer.

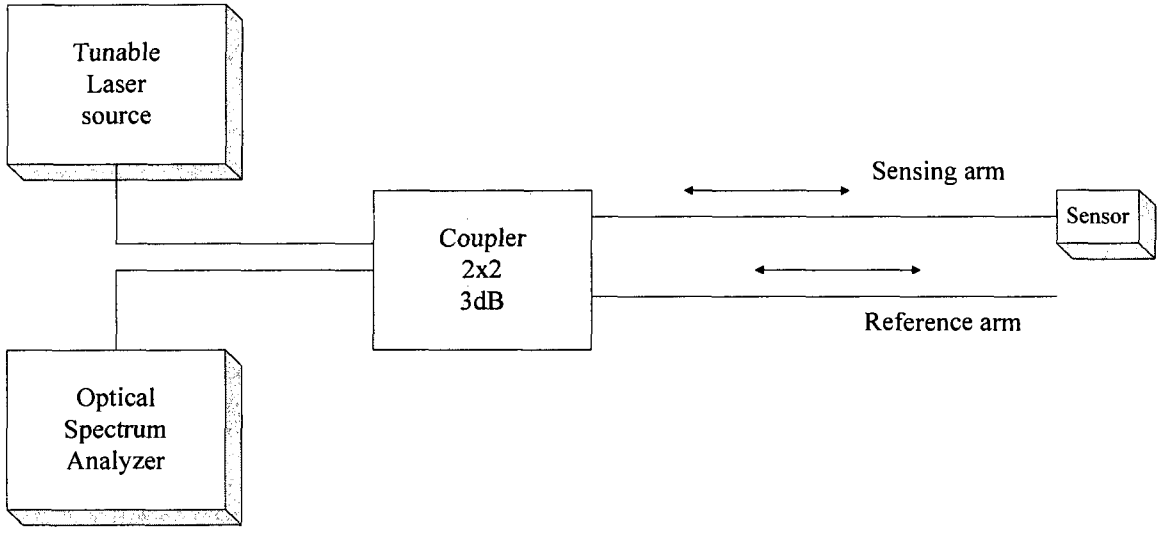

Figure 2. 1. Schematic of a Michelson interferometer.

The Michelson interferometer configuration uses one 3 dB coupler and two fibers with mirrored ends for back reflection. The input laser light is split 50 – 50 between mirrored fibers and then the light is reflected from reference and sensing fibers to the detectors where phase shift is detected. The sensor is defined by the difference in the length of sensing and reference arms.

A phase shift occurs when environment perturbs one fiber relative to the other. The change in phase results from changes in the length and the refractive index of the sensing fiber [36]. For interferometric sensors the output beam should be in phase to achieve

constructive interference. The ability of fiber to hold polarization state minimizes the possibility of degenerated modes that degrade sensitivity.

The change in the length of the sensing fiber will decrease the common intensity output due to the phase shift between sensing and reference arms. This effect will create destructive interference. If the phase shift is the integral number of wavelengths (ϕ = 0, 2π, 4π, etc.) then two legs of the interferometer are in phase and provide constructive interference and maximum intensity. If the phase shift is integral number of the half wavelengths ($\varphi = \pi$, 3π, etc.) then two beams interfere destructively and have minimum intensity. Path length difference in 1/4 λ in the fiber of Michelson interferometer will result in a 1/2 λ path length change due to the second pass of the reflected beam in Michelson interferometer design. Therefore, for Michelson interferometer minimum intensity is at phase shift of integral number of ¼ wavelengths ($\varphi = \pi/2$, $3\pi/2$, $5\pi/2$, etc.), and it has the greatest rate of change of intensity with phase shift and highest sensitivity for ($\phi = 0, \pi, 2\pi$, etc.).

This destructive interference leads to zero combined intensity in the output of Michelson interferometer. Constructive interference will occur accordingly in phase shift for π, 2π, and etc.

As the result, valuable information for one cycle will be in phase shift from 0 to $\pi/4$ where phase shift increase gives increase in power output from minimum to maximum. Figure 2.2 shows the power output from Michelson interferometer.

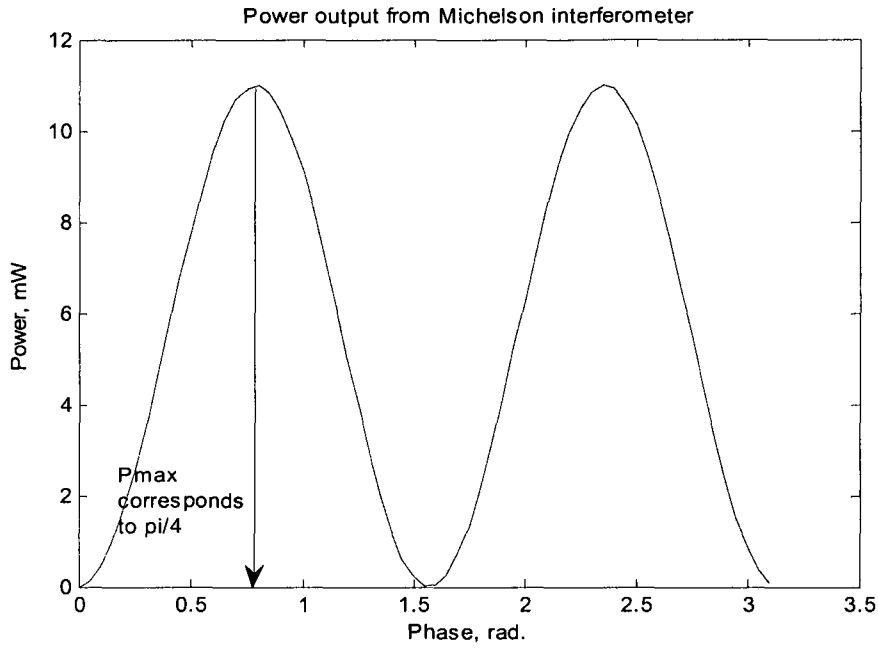

Figure 2.2. Power output from Michelson interferometer.

Intensity of the signal increases from 0 radians to $\pi/4$ radians. The optical phase shift modulation of the light in the signal arm induced by the strain in the interferometer is converted into an intensity modulation at the output by mixing the light from the signal and reference arms in the output fiber coupler.

The disadvantage of this interferometer is the feedback into the laser from mirrored fibers that is a source of noise, especially in high performance systems [37] and lack of the directivity in Michelson interferometer.

2.1.1 Fabrication of the Michelson Interferometer

Michelson interferometer includes sensing and reference arms from single mode optical fibers with reflected ends, 3 dB or 50 /50, 2x2 coupler, laser source, and optical spectrum analyzer.

Fibers for sensing and reference arms were cleaved and mirrored using physical vapor deposition technique. Aluminum was used (99.9%) and was deposited on the tips of the optical fibers to achieve reflectance of the light.

Coupler was used to divide signal between sensing and reference arms and couples these signals back. The basic principle of fiber coupler is that under appropriate conditions light transfer can occur between adjacent fiber cores via a mechanism called evanescent wave coupling. In this design two fiber cores are in close proximity, the evanescent field of the signal traveling in the throughput fiber reaches into and excites the mode of the coupled fiber. When the modes of the two fibers exhibit the same phase velocity, resonant interaction take place and total energy transfer occurs after some interaction length referred to as the coupling length. If the interaction is allowed to continue beyond this point, the fiber roles are reversed and the signal is coupled back into the throughput fiber until the entire signal resides in the throughput fiber after two coupling lengths. This is called "over coupling" [37]. If the length of the coupling region is sufficient, the process repeats itself in a cyclical manner along the length of the coupler according ref. [38].

Neglecting polarization effects the output intensities, I_1 and I_2 are given [39] as

$$I_1 = I_0[1 - V\cos(\phi_a - \phi_b)]$$
$$I_2 = I_0[1 + V\cos(\phi_a - \phi_b)] \quad (2.1)$$

where V is the visibility and equal to $\frac{P_{max} - P_{min}}{P_{max} + P_{min}}$. The visibility of the interference is independent of the splitting ratio of the coupler, and depends only on the reflectivity of the fiber ends, the initial shift between sensing and reference arms, and on the coherence properties of the source. [39].

The phase difference, $\phi_a - \phi_b$, can be represented by contribution from the noise sources, ϕ_d, and signal, $\phi_s \sin\omega_s t$, including the effect of a harmonic signal of amplitude ϕ_s and circular frequency ω_s [38]. The phase difference is expressed as

$$\phi_a - \phi_b = \phi_d + \phi_s \sin\omega_s t \quad (2.2)$$

and photocurrent, I_D, can be expressed as [38]

$$I_D = I_{0D}[1 + V\cos(\phi_d + \phi_s \sin\omega_s t)] \quad (2.3)$$

Phase control is required in the interferometer. Active phase control is achieved by application of a physical stimulus to the reference arm of the interferometer. Piezoelectric element is used to strain the fiber and produce phase modulation.

2.1.2 Michelson Interferometer sensing nature.

Michelson Interferometer can detect strain and temperature due to the phase shift. Theoretical calculations of the strain and temperature sensitivities are represented next.

Calculation of the phase shift due to strain

The phase delay, ϕ, of the light traveling through the fiber of length, L, is equal in ref. [40] as

$$\phi = \beta L \tag{2.4}$$

where $\beta = \frac{2\pi n_{eff}}{\lambda}$ is propagation constant, effective refractive index, n_{eff}, depends from velocity of the light inside the optical fiber and equals 1.4682 [41].

The phase change can be expressed as [16, 40]:

$$\Delta\phi = \beta\Delta L + L\Delta\beta \tag{2.5}$$

where phase change depends from change in the optical fiber length due the applied strain, this is physical effect, and change in propagation constant due two effects such as strain-optic effect where strain changes the refractive index of the fiber and waveguide dispersion effect due to a change in fiber diameter produced by the strain [15, 16, 40]. Figure 2.3 shows the applied stress along the fiber.

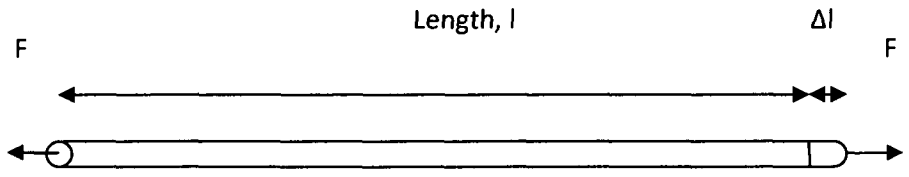

$$\varepsilon_{axial} \equiv \frac{\Delta l}{l}$$

Figure 2.3. Applied stress along the fiber.

The first term can be represented [15, 16, 40] as

$$\beta\Delta L = \beta L\varepsilon \tag{2.6}$$

where ε is the strain along the optical fiber.

The second term is given as sum of two effects. [15, 16, 40]

$$L\Delta\beta = L\frac{d\beta}{dn}\Delta n + L\frac{d\beta}{dD}\Delta D \tag{2.7}$$

where n is refractive index of the propagation medium, core of the optical fiber and D is diameter of the core. The first derivation depends from the photoelastic effect where the density of the crystal is changed due the strain, and distortion of the bonds is resulted. Induced strain is proportional to the change in $1/n^2$, and proportionality constant is p (photoelastic coefficient). The photoelastic effect is given from ref. [15] and [42], [16]

$$\Delta\left(\frac{1}{n^2}\right)_i = pS = \sum_{j=1}^{6} p_{ij} S_j \tag{2.8}$$

where $S_j = \begin{bmatrix} \varepsilon \\ -\mu\varepsilon \\ -\mu\varepsilon \\ 0 \\ 0 \\ 0 \end{bmatrix}$ is the strain vector for longitudinal strain in the x direction and μ is Poisson's ratio from ref. [16, 43], p is strain-optic tensor for homogeneous isotropic material, and it is given from ref. [15, 43] as

$$p_{ij} = \begin{bmatrix} p_{11} p_{12} p_{12} \\ p_{12} p_{11} p_{12} \\ p_{12} p_{12} p_{11} \end{bmatrix} \tag{2.9}$$

The photoelastic effect for material with no shear strain can be considered only for i, j = 2,3 elements of the strain-optic tensor. The optical indicatrix is given as

$$\Delta\left(\frac{1}{n^2}\right)_{2,3} = \varepsilon p_{12} - \mu\varepsilon p_{11} - \mu\varepsilon p_{12} = \varepsilon p_{12}(1-\mu) - \mu\varepsilon p_{11} \tag{2.10}$$

This equation shows that the refractive index in y and z directions changes due to the strain.

As a result, change in refractive index in x-direction of the light propagation is equal to:

$$\Delta n = -\frac{1}{2} n^3 \Delta\left(\frac{1}{n^2}\right)_{y,z} = -\frac{1}{2} n^3 \left(\varepsilon p_{12}(1-\mu) - \mu\varepsilon p_{11}\right) \tag{2.11}$$

The first part of the equation (7) can be expressed as

$$L\frac{d\beta}{dn}\Delta n = -L\frac{n^2\beta}{2}\left[\varepsilon p_{12}(1-\mu) - \mu\varepsilon p_{11}\right] \tag{2.12}$$

where $\frac{d\beta}{dn} = \frac{2\pi}{\lambda} = \beta_0$ propagation constant change due to the change in refractive index [41,16].

The change in diameter due the strain is given in ref. [16] as

$$\Delta D = S_3 D = \mu\varepsilon D \tag{2.13}$$

where D is diameter of the core, S_3 is the strain in z direction, and ε is the strain which results in diameter change.

Next, waveguide dispersion arises as the result of the dependence of the propagation constant on the V-number, which depends on the wavelength [44].

The normalized parameters which are used to characterize the waveguide mode dispersion are normalized propagation constant, b, and V-number/normalized frequency, V, where b and V are: [44]

$$b = \frac{\beta^2/k_0^2 - n_{clad}^2}{n_{core}^2 - n_{clad}^2} \tag{2.14}$$

$$V = \frac{2\pi}{\lambda} a\left(n_{core}^2 - n_{clad}^2\right)^{1/2} \tag{2.15}$$

where a is radius of the core in optical fiber, λ is wavelength in vacuum, and D=2a.

From ref. [15], [16] the derivative of the refractive index is given as

$$\frac{d\beta}{dD} = \frac{d\beta}{db}\frac{db}{dV}\frac{dV}{dD} = \frac{V}{D}\frac{2V^2}{\beta D^2}\frac{db}{dV} \tag{2.16}$$

where

$$\frac{dV}{dD} = \frac{1}{2} k_0 \left(n_{core}^2 - n_{clad}^2\right)^{1/2} \tag{2.17}$$

$$\frac{d\beta}{db} = \frac{\left(n_{core}^2 - n_{clad}^2\right)k_0^2}{2\beta} = \frac{V^2 4}{2\beta\beta^2} \tag{2.18}$$

and $\frac{db}{dV}$ is the slope of the b-V dispersion curve at the point which describes the waveguide mode from ref. [44].

Finally, the phase shift can be expressed as in ref. [15] including waveguide mode dispersion effect due to a change in the fiber diameter as

$$\Delta\phi = (\beta\varepsilon L - L\frac{\beta n^2}{2}\varepsilon[(1-\mu)p_{12} - \mu p_{11}] + L\varepsilon\frac{2\mu\mu^3}{\beta D^2}\frac{db}{dV}) \tag{2.19}$$

The practical formula for phase shift excludes the last part due negligible dispersion effect according ref. [40], [15], [16], and it is given as

$$\Delta\phi = \beta L\varepsilon\left(1-\frac{n^2}{2}\left[(1-\mu)p_{12}-\mu p_{11}\right]\right) = \beta L\varepsilon G \tag{2.20}$$

where ε is strain along the fiber due to axial stress and G is strain-phase coupling coefficient.

The phase responsivity $R = \Delta\varphi/\varepsilon L$ to strain is given in ref. [40] as

$$R = \beta\left\{1-\frac{n^2}{2}\left[(1-\mu)p_{12}-\mu p_{11}\right]\right\} = \beta G \tag{2.21}$$

From the above formula phase change and responsivity of the optical fiber can be obtained. Because the signal passes the phase sensitive region twice the sensitivity is doubled and it is given as

$$R_{MI} = \frac{\Delta\phi}{\varepsilon L} = 2*\beta*G \tag{2.22}$$

Numerical values of the parameters used for calculations were taken from the Corning ® website for SMF-28 [45], [15], and mechanical properties of 96% silica glass [46]. The

exact parameters for this material, Corning® SMF-28™, were not available. Table 2.1 provides the values of the parameters [15, 45, 46].

Table 2.1. Parameters for single mode fiber [15, 45, 46].

n_{core}, ref. [49]	Diameter, D, μm, ref.[49]	E, 10^{10} N/m²	p_{11}	p_{12}	$\frac{\Delta n}{\Delta T}$, $10^{-6}/°C$	μ	CTE, $\frac{\mu m}{m*°C}$
1.4682	8.2	7.0	0.121	0.27	10	0.19	0.75

Table 2.2 shows data for calculating the phase shift, $\Delta\phi$, phase responsivity, R, and strain sensitivity, ε, for a given laser source output and single mode fiber.

Table 2.2. Data for phase shift due to the strain and strain sensitivity.

P_{max}, dBm	λ_s, nm	β, $10^6 m^{-1}$	$\Delta\phi, 10^6\ \varepsilon L$	R, 10^6	$\varepsilon, \mu\varepsilon$	G
5.5	1550	5.9519	9.39234	9.39281	0.213	0.78906

For the fiber optic embedded in composite the phase shift sensitivity will be the same as for free fiber.

Effect of Temperature on Phase Shift.

Due to the thermal expansion of the fiber as well as variation of refractive index versus temperature, the optical phase shift will be affected by temperature. The changes can be calculated as: [16].

$$\Delta\phi = \frac{\pi}{\lambda}\left(\frac{n}{L}\frac{dL}{dT} + \frac{dn}{dT}\right) \tag{2.23}$$

This formula includes the reflected back light propagation effect which includes double distance for Michelson interferometer.

Calculation of phase shift due to the applied pressure.

Pressure can be measured by optical sensor. Stress, σ, due to the applied pressure, P, is three-component vector [15]:

$$\sigma = \begin{bmatrix} -P \\ -P \\ -P \end{bmatrix} \tag{2.24}$$

Figure 2.4 illustrates applied pressure on the optical fiber.

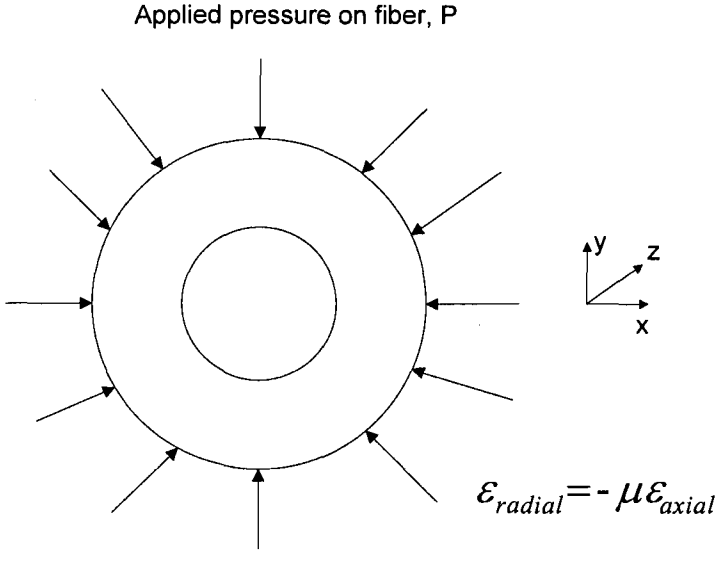

Figure 2.4. Applied pressure on optical fiber.

Strain, ε, is three-component vector:

$$\varepsilon = \begin{bmatrix} \varepsilon_x \\ \varepsilon_y \\ \varepsilon_z \end{bmatrix} = \begin{bmatrix} -P(1-2\mu)/E \\ -P(1-2\mu)/E \\ -P(1-2\mu)/E \end{bmatrix} \tag{2.25}$$

where μ is Poisson's ratio and E is Young's modulus of optical fiber.

The phase shift due to the applied pressure is [15]:

$$\Delta\phi = -\beta(1-2\mu)L\frac{P}{E} + \frac{\pi}{\lambda}n^3 L\frac{P}{E}(1-2\mu)(2p_{12}+p_{11})/2 = \\ = -\frac{P}{E}(1-2\mu)\beta L\left(1-\frac{n^2}{2}[2p_{12}+p_{11}]\right) \tag{2.26}$$

Waveguide mode dispersion effects were omitted due to negligible value. Phase shift per meter length and per unit of pressure, Pa, is equal to $2*1.5159*10^{-5} = 3.03181*10^{-5}$ rad. The calculations are based on data from Table 2.1 and assuming laser source at 1550 nm.

Phase shift for embedded optical fiber in composite structure.

Optical fiber embedded inside composite structure experiences the stresses applied to the composite structure which is transformed by matrix. Edward E. Tapanes in his thesis [47] illustrated in-plane load assumptions between matrix and optical fiber such as

$$\varepsilon_{11}^{f} = \varepsilon_{11}^{\mathrm{m}} \tag{2.27}$$

$$\sigma_{22}^{f} = \sigma_{22}^{\mathrm{m}} \tag{2.28}$$

$$\sigma_{12}^{\mathrm{f}} = \sigma_{12}^{\mathrm{m}} \tag{2.29}$$

where superscript 'f' denotes optical fiber and 'm' refers to matrix.

The first assumption is that bonding between the optical fiber and matrix is perfect, second assumption states that stress perpendicular to the fiber is continuous across matrix and optical fiber, and the third assumption is that shear stress is the same in matrix and fiber. Using these assumptions and definitions of strain and stress E.E. Tapanes [47] derived strain tensor, S_j, for an embedded fiber in terms of the strain in the matrix is given as

$$S_j = \begin{bmatrix} \varepsilon_{11}^{\mathrm{m}} \\ -\mu^{f} * \varepsilon_{11}^{m} \\ -\mu^{f} * \varepsilon_{11}^{m} \\ 0 \\ 0 \\ \dfrac{\mathrm{G}^{\mathrm{m}}}{\mathrm{G}^{\mathrm{f}}} * \varepsilon_{12}^{m} \end{bmatrix} \tag{2.30}$$

where G^{m} and G^{f} are shear modulus of matrix and optical fiber.

Because the strain in matrix and optical fiber is the same and last row in Equation (2.30) will be canceled during multiplication with strain-optic tensor the strain-phase sensitivity is the same as for free fiber.

Error calculations.

The response of embedded phase-based optical fiber sensors is given as: [48]

$$\delta = \frac{\Delta\phi}{\phi_0} = F_a S_1^f + F_{t2} S_2^f + F_{t3} S_3^f + F_T T^f \tag{2.31}$$

where δ is normalized phase change of the sensor, ϕ_0 is absolute phase retardation of the light propagation in the fiber sensor when it is free of thermo-mechanical loading, F_a is sensitivity of the sensor to axial strain, F_{t2} is sensitivity of the sensor to transverse strains in the 2-nd direction, F_{t3} is sensitivity of the sensor to transverse strains in the 3-rd direction, and F_T is sensitivity of the sensor to temperature. The error due to transverse strains or thermal loading is given from ref. [48]

$$E = 100 * \frac{\delta - \delta'}{\delta'} = 100\left[(F_a - F) + K_{t2} \frac{S_2^f}{S_1^f} + K_{t3} \frac{S_3^f}{S_1^f} + \gamma \frac{T_f}{S_1^f} \right] \tag{2.32}$$

where δ' is ideal sensor response for axial strain and equal to

$\delta' = FS_1^f = \varepsilon\left[1 - \frac{n^2}{2}\left((1-\mu)p_{12} - \mu p_{11}\right)\right]$ and δ is normalized by F_a sensitivity sensor response where $K_{t2} = \frac{F_{t2}}{F_a}$, $K_{t3} = \frac{F_{t3}}{F_a}$, and $\gamma = \frac{F_T}{F_a}$ are two transverse strain and thermal apparent strain sensitivity factors, respectively. The sensor error is the function of difference between the actual and calibrated axial sensitivities, the transverse strain

sensitivities and thermal sensitivity factors, and the loading ratios S_2^f / S_1^f, S_3^f / S_1^f, and T^f / S_1^f. This error equation for optical fiber sensor qualifies the amount of error that is attributable to phase change associated with the loading except the axial strain.

2.2 Analysis of Composite Laminates

The composite material consists of heterogeneous anisotropic medium. The proper structural theory should be used to model the stiffness, stress fields and to determine the initiation and growth mechanisms of different failures [49]. In a heterogeneous system, the material properties are a function of position. In an isotropic medium the physical properties at point A will remain invariant for any arbitrary rotation of axes. In an anisotropic medium the physical properties at point A will be directionally dependent or in other words given material property will have different values in different directions.

The composite material is an anisotropic because it has different modulus along the fiber direction and transverse to it. Assuming that fibers in composite are parallel the composite material can be treated as a homogeneous orthotropic material with x-axis along the fibers.

Damage mechanisms in laminate are intra-ply damage is damage within the ply, fiber-matrix debonding, fiber fracture, fiber pull-out, matrix cracks, and interplay damage: delamination.

In the Fiber Optic Smart Structures J. S. Hansen [50] shows that the assumption was made based on that the lamina is in a state of plane stress. Plane stress is a state of stress where only the components of the stresses in the plane are non-zero. Therefore, out-of-

plane stresses σ_3, τ_{13}, τ_{23} may be ignored due to small values to the in-plane stresses σ_1, σ_2, τ_{12}.

Thermal coefficient of expansion of epoxy is about $1081.6*10^{-6}$/°C (32.0 $*10^{-6} in./in./^{\circ}F$), while that of a graphite fiber is about $50.7*10^{-6}$/°C (1.5 $*10^{-6} in./in./^{\circ}F$, 1°C= 33.8°F) according J. Hansen [50]. Thermosets are cured at about 176.67°C (350°F).

Failures in mechanical structures are due to the static overload, impact, or fracture. The modes of the fracture are fiber failure matrix cracking, or delamination.

The tensile and compressive failure stresses have different values due to different failure mechanisms. In 1-direction tensile failure stresses are 1.5 times compressive failure stresses. The overview of the composite structure demonstrates the complicity of the analysis that should be used for evaluation of material characteristics. The embedded optical fiber sensors will complicate the mechanics of the structure. The interaction between the optical fiber and composite material or host can be explored by numerical, analytical, and experimental stress analysis techniques.

Theoretical calculations for composite packages.

Analysis with lay-up of the unidirectional tape with carbon fiber in 0° direction along the applied force with four layers, [0/0/0/0] package design, lay-up of the unidirectional tape with carbon fiber in 90° direction with reference to the applied force, [90/90/90/90] package design, lay-up with carbon fiber in -45°, 45°, 45°, and -45° direction with reference to the applied force, [-45/45/45/-45] package design, and lay-up of the unidirectional tape with carbon fiber in -60°, 60°, 60°, -60° direction with reference to the applied force, [-60/60/60/-60] package design, was performed using Laminate Analysis

Program (LAP 3.0F) where strain 2000 με was applied along x-axis on 1 m² laminate. The initial data is given in Table 2.3. The thickness of one ply was 0.125 mm, and the laminate thickness was 0.5 mm, fiber volume fraction, v_f=0.6. Table 2.3(a) and (b) illustrates obtained data.

Table 2.3. Mechanical properties for composite carriers a) for composite carriers fabricated from CYCOM® 5276-1, b) for composite carriers fabricated from NCT-301.

a

Laminate design	[0/0/0/0]	[90/90/90/90]	$[\mp 45]_s$	$[\mp 60]_s$
Young's modulus in x-direction, E_x, GPa	157.7	8.54	16.726	9.955
Young's modulus in y-direction, E_y, GPa	8.54	157.7	16.726	48.75
Shear modulus, G_{xy}, GPa	4.63	4.63	40.418	31.47
Poisson ration in xy-direction, ν_{xy}	0.32	0.02	0.81	0.31
Poisson ratio in yx-direction, ν_{yx}	0.017	0.32	0.806	1.54

b

Laminate design	[0/0/0/0]	[90/90/90/90]	$[\mp 45]_s$	$[\mp 60]_s$
Young's modulus in x-direction, E_x, GPa	131.0	8.97	14.98	9.553
Young's modulus in y-direction, E_y, GPa	8.97	131.0	14.98	43.121
Shear modulus, G_{xy}, GPa	4.172	4.172	33.843	26.425
Poisson ratio in xy-direction, ν_{xy}	0.304	0.021	0.795	0.317
Poisson ratio in yx-direction, ν_{yx}	0.021	0.304	0.795	1.4304

These data were used for simulations purposes.

The strain for 2000με was applied to the described above composite packages. The simulations using Laminate Analysis Program are illustrated in Table 2.4.

Table 2.4. Results of the simulations for composite packages a) from CYCOM® 5276-1, b) from NCT-301.

a

Laminate design	[0/0/0/0]	[90/90/90/90]	$[\mp 45]_s$	$[\mp 60]_s$
ε_x, με	2000	2000	2000	2000
ε_y, με	-640	-34.66	-1612.518	-627.942
σ_x, MPa	315.4	17.08	33.452	19.91
			-14.53	-3.832
			(for -45° layers)	(for -60° layers)
τ_{xy}, MPa	-	-		
			14.53	3.832
			(for 45° layers)	(for 60° layers)

b

Laminate design	[0/0/0/0]	[90/90/90/90]	$[\mp 45]_s$	$[\mp 60]_s$
ε_x, με	2000	2000	2000	2000
ε_y, με	-608	-41.63	-1591	-633.823
σ_x, MPa	262.0	17.94	29.96	19.107
			-12.57	-2.485
			(for -45° layers)	(for -60° layers)
τ_{xy}, MPa	-	-		
			12.57	2.485
			(for 45° layers)	(for 60° layers)

The results of the simulations for LAP 3.0 F showed comparably small compressing transversal strain in y direction for three packages except $[\mp 45]_s$ where negative strain in direction perpendicular to the applied load condition is more than three quarters of the applied strain in x direction. The negative strain can compress the optical fiber inside of this particular package and will alter a measuring strain along optical sensor embedded in composite package. The composite package from CYCOM® 5276-1 material was fabricated, and geometry of the resin pocket was depicted for preliminary ANSYS simulations done before tensile tests with composite packages.

CHAPTER 3

EXPERIMENTAL WORK

Experimental work includes the fabrication of the composite carriers with four different lay-ups, microscopy results on fabricated samples, tensile tests where composite packages were bonded on the aluminum samples on which axial force was applied. Finally, microscopic observations after tensile tests were made in order to observe fracture surfaces.

Composite carriers were fabricated from graphite/epoxy. Graphite is the reinforcement and epoxy is the polymer matrix.

3.1 Manufacturing process

Variations in manufacturing process parameters can alter the material surface properties. The reason is that adhesive properties depend from roughness, surface free energy, chemical composition and etc. Q. Bénard *et al.* [51] demonstrated experimentally that tool preparation can effect and modify surface parameters.

Fabrication of composite with epoxy matrix requires autoclave curing. Curing process lasts for four hours and it involves a combination of high temperature, pressure, and vacuum. The prepreg layers are cured within a sealed structure which includes porous release film on the prepreg layers, and then bleed cloth (absorption ply), breather,

and bladder. Bladder was attached to the aluminum plate with thermal double side tape. Figure 3.1 illustrates the layup for fabrication.

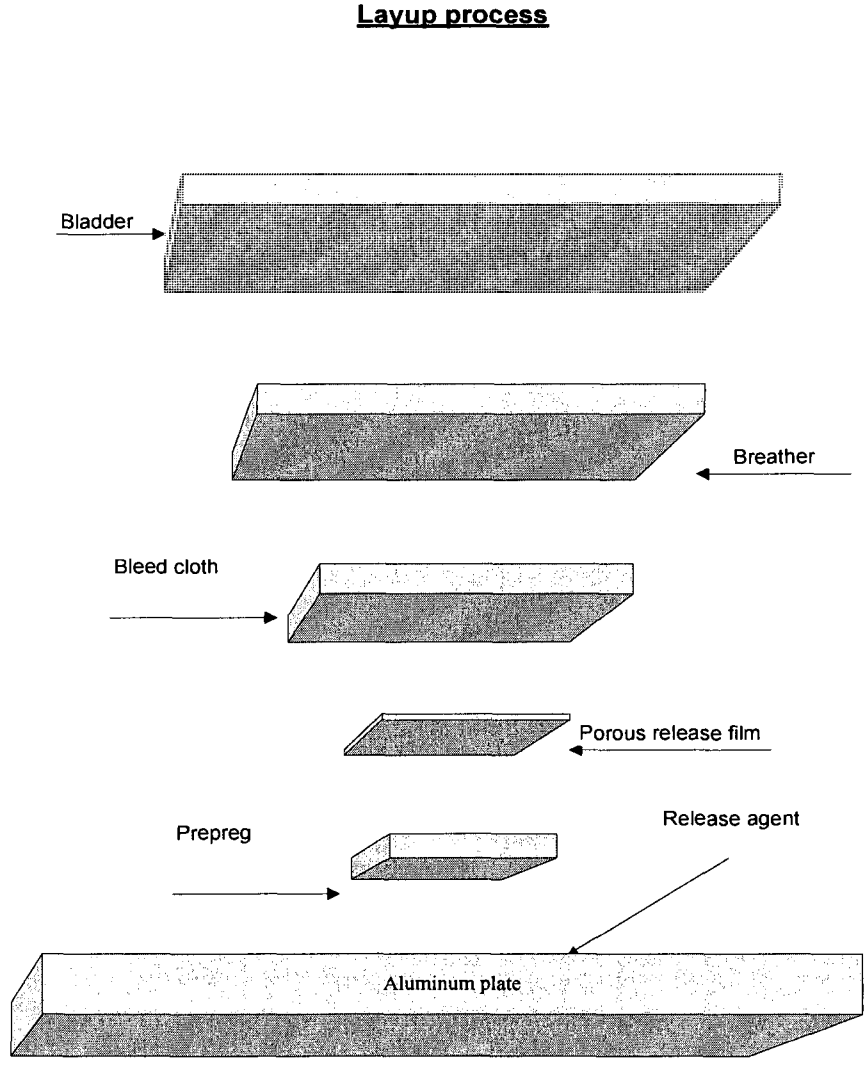

Figure 3.1. Layup process for fabrication of composite carrier.

After bladder was attached to the aluminum plate with double thermal tape and this blanket was connected to the vacuum prepreg was placed inside autoclave for curing. Autoclave has 2' x 4'4'' size, 125 psi maximum pressure, 204 °C maximum temperature. It was purchased from Mécano Soudure Drummond Ltée.

Autoclave program 99 was used for fabrication where increase in temperature was until 177° C, and applied pressure was 60 psi. For next fabrication of packages (with 100 μm adhesive layer due to better performance) 70 psi pressure was applied in order to decrease resin pocket between optical and carbon fibers and resin layer between the plies of prepreg. According to F. L. Matthews [35] not properly controlled manufacturing process can cause the defects inside the laminate: voids (small cavities in resin), delamination (unbonded areas between layers), or not often longitudinal cracks (lack of bonding between reinforcement and matrix). The cause for voids is that prepreg was not warmed to room temperature before laying-up, and moisture was inside the prepreg stack. Delaminations are due to entrapped air or the inclusion of pieces of backing sheet. Longitudinal splitting and delamination can occur in multi-directional laminates caused by thermal stresses induced during cool-down from the curing temperature [35]. New material NCT 301, carbon/epoxy, was used for final tests with three proposed designs which illustrated better performance during the tests with CYCOM® 5276-1 composite material. The composite carriers from CYCOM® 5276-1were fabricated using fabrication cycle #1 and composite carriers from NCT301 were fabricated using fabrication cycle #2. Figure 3.2 illustrates curing cycles used for fabrication composite carriers.

a) fabrication #1

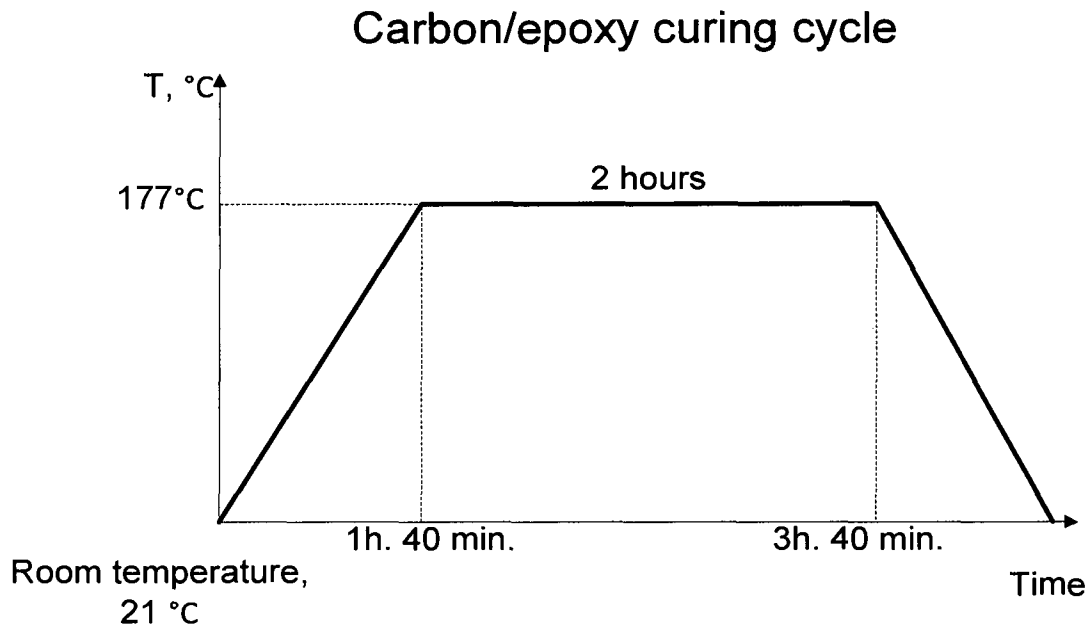

b) fabrication #2

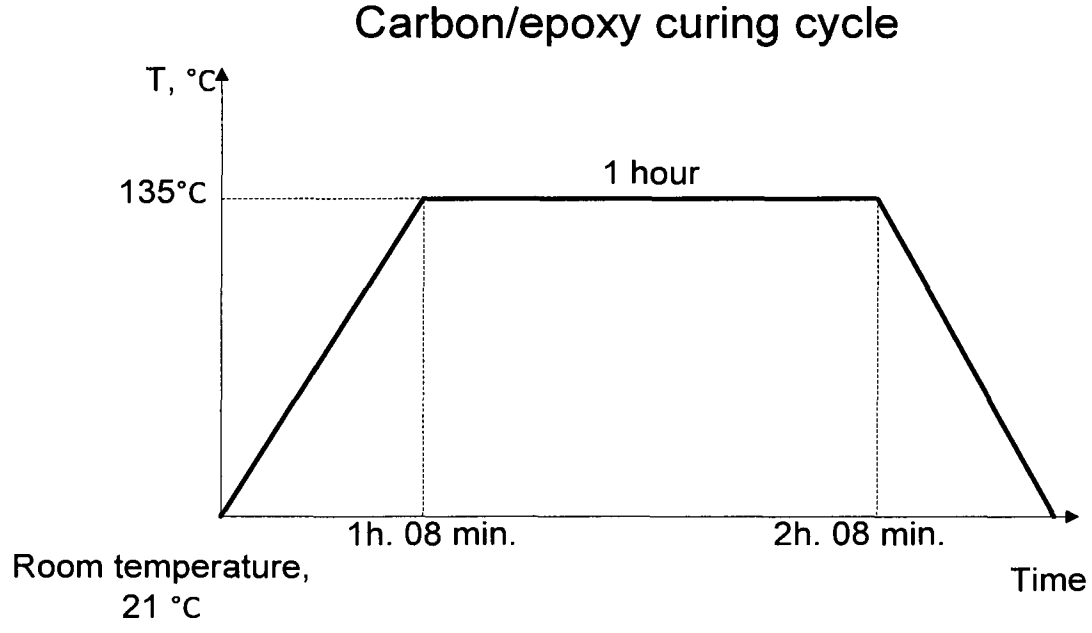

Figure 3.2. Curing cycle for carbon/epoxy: a) fabrication #1 with 60 psi and 70 psi pressure applied and b) fabrication #2 with 50 psi pressure applied.

Fabricated composite packages with embedded optical fiber inside using CYCOM® 5276-1 composite material with four lay-ups such as [0/0/F(0)/0/0], [-60/60/F(0)/60/-60], [-45/45/F(0)/45/-45], [90/90/F(0)/90/90] were cut using diamond-tipped saw and lay-ups such as [-60/60/F(0)/60/-60], [-45/45/F(0)/45/-45], and [90/90/F(0)/90/90] were fabricated from NCT301 composite. Figure 3.3 illustrates fabricated composite package.

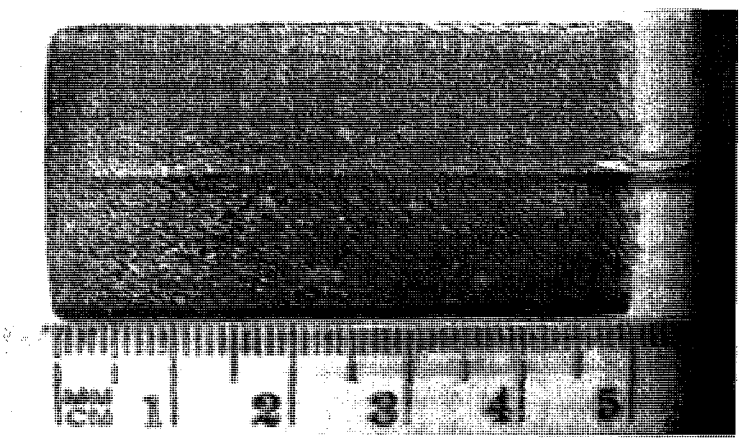

Figure 3.3. Fabricated composite carrier for optical sensor.

Then fabricated samples were prepared for microscopy observations in order to learn the geometry of the resin pocket which usually appears due to the difference in diameter size of carbon and optical fiber, 5 μm and 125 μm respectively.

3.2 Microscopy on the fabricated samples

The cut composite packages were embedded inside epoxy and then ground and polished. Grinder/polisher was used for sanding and polishing. Embedded inside epoxy

composite packages were sanded using 400, 600, and polished with 800 grit paper discs with water for lubrication. Finally, packages were polished using Nylon Arctic with 1 micron diamond suspension and water based diamond extender as lubricant; and fine polishing was performed with Imperial using 0.05 micron SiC suspension for 5 min. Polished surface had a mirror finish upon completion of this polishing process. Surface preparation and morphology assessment was done with the equipment and software listed in Table 3.1.

Table 3.1. Equipment and software for microscopy observations.

Name of the instrument	Grinder/Polisher	Optical microscope	Digital camera	Software
Model number	METASERV2000	Ergolux	Moticam 2000	Motic Images Plus 2.0
Manufacturer	BUEHLER	Leitz		
Objective		NPL Fluotar		
Magnification		50x10.85 DF	with camera magnified by 10 more	
Resolution of camera			2.0M Pixel USB 2.0	

First fabricated sample for resin pocket investigation had [0/F(0)/0] lay-up using composite material graphite/epoxy (CYCOM® 5276-1). The magnification 500 was used for macroscopic image which is illustrated in Figure 3.4.

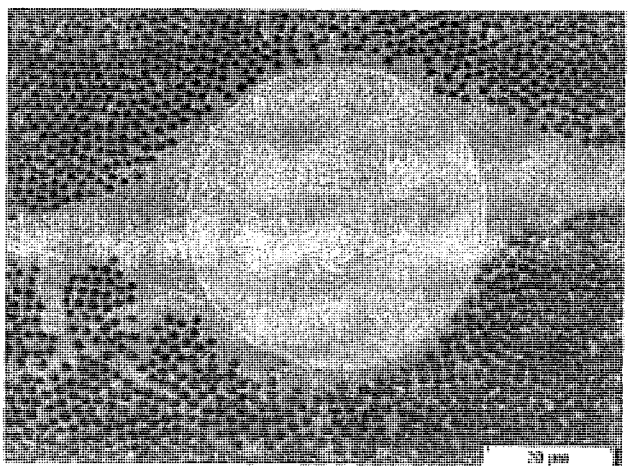

Figure 3.4 Microscopic results, [0/F(0)/0] layup design of composite carrier.

Next fabrication was done for new lay-up [0/0/F(0)/0/0] and microscopic observations in Figure 3.5 illustrated decrease in the size of the resin pocket.

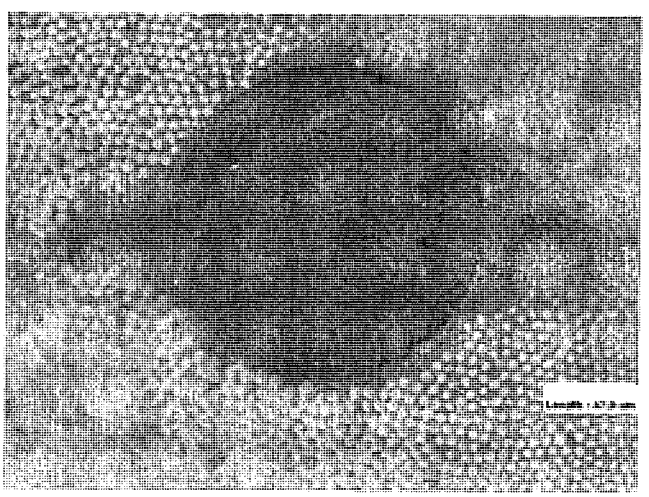

Figure 3.5 Microscopic results, [0/0/F(0)/0/0] layup design of composite carrier.

The geometry of the resin pocket was obtained from the microscopy results. Thereafter, based on the estimated geometry of this sample ANSYS simulations were performed for twice larger, twice smaller, and real geometry of the resin pocket. SOLID92 was used for simulations. The appearance of the resin pockets is due to the different diameter in optical and carbon fiber. However, it could be due to the inadequate amount of the pressure applied during the curing or due to the quality of the material. The design with four layers of composite material was used for tensile tests.

3.3 Tensile Tests

Composite package design for optical sensor was tested. Initially, four lay-ups were fabricated and bonded to the aluminum samples. Aluminum samples were 10 inch x 1 inch. Two types of adhesive were tested. First adhesive was cyanoacrylate which is used for electrical strain gauge adhesion as well. The tensile tests were performed with this adhesive, but this adhesive showed inability to provide the adequate bonding strength for composite package due to the partial disbonding. The composite packages were partially disconnected from aluminum. Second choice was epoxy. Epoxy (EPON 862/EPI-CURE 3234 15.4% of weight (HEXION™))with adhesive layer 250 micrometer and 100 micrometer in thickness was used for bonding of the composite carriers to the aluminum samples. The proper treatment of the surface of the aluminum and composite package was important issue in bonding. Extra grinding to obtain slightly rough surface of the composite carrier was performed. Glass beads with 250 micrometer and 100 micrometer

diameters were used to control the thickness of the adhesive layer for composite packages. Curing of the epoxy adhesive was 7 days at room temperature without postcuring. Four lay-up designs were used for tensile tests for two different thicknesses of the adhesive for CYCOM®5276-1 and three lay-ups disregarding [0/0/F(0)/0/0] design using 100 micrometer thickness of the adhesive layer were used for tensile tests with NCT301 composite carriers. MTS 100 kN machine was used for static tensile tests.

3.3.1 Experimental design.

Basic mechanical formulas used for calculations in applying the necessary force to the aluminum sample, and dependence of the phase shift from applied force which was used for evaluation of the data in tensile tests is recorded next.

1) Mechanical test

According to Hook's law, axial stress, S, is given for glass fiber as

$$S = E\varepsilon \tag{3.1}$$

where E is the elastic modulus, $\varepsilon = \frac{\Delta l}{l}$ is longitudinal deformation.

The load along fiber when it reaches mechanical maximum, F_f, is given as

$$F_f = S_f \times A \tag{3.2}$$

where S_f is the specified tensile strength of optical fiber, and A is the cross sectional area of the fiber.

2) Photoelastic predictions

Phase shift in Michelson interferometer is proportional to the applied strain and it is expressed as

$$\Delta\phi = \phi_s - \phi_r = \beta G\varepsilon = \beta G\frac{F}{AE} \tag{3.3}$$

where β is propagation constant, G is strain-phase coupling coefficient, and ε is axial strain, equals $\frac{\Delta\phi}{\beta G}$, F is applied load, A is cross sectional area, E is Young's modulus of optical fiber, ϕ_s is phase in sensing arm and ϕ_r is the phase in reference arm, $\Delta\phi$ is phase shift.

3.3.2 Experimental results.

Mechanical characterization of composite material graphite/epoxy (CYCOM® 5276-1) was taken from experimental results of Chao Zhang's Ph. D. thesis [52] and properties of adhesive was taken from HEXION datasheet [53]. Mechanical properties for NCT 301were recorded from Newport technical data sheet and shear modulus was included from experimental data in ref. [54]. Table 3.2 represents mechanical properties of the composite carrier and bonding epoxy resin which was used to place composite carrier on the aluminum sample.

Table 3.2. Mechanical properties of graphite/epoxy and bonding epoxy resin.

Material	E_1, GPa	E_2, GPa	G_{12}, GPa	μ_{12}	μ_{21}
Graphite/epoxy	157.7	8.54	4.63	0.32	0.3
NCT 301, carbon/epoxy	131.0	8.97	4.172 [2]	0.304	0.3
EPON™ Resin 862/EPI-CURE 3234 15.4% of weight	3.24	3.24	1.25[1]	0.3[1]	0.3

[1] from reference [53]

[2] from reference [54]

Epoxy was used to adjust fabricated samples on the aluminum. EPON™ Resin 862 (HEXION™) was used with curing agent EPI-CURE 3234 (TETA) 15.4% of weight. EPON Resin 862 (Diglycidyl Ether of Bisphenol F) is low viscosity, liquid epoxy resin manufactured from epichlorohydrin and Bisphenol-F. This resin once linked with appropriate curing agent exhibits superior mechanical, adhesive, electrical and chemical resistance properties. TETA (triethylene tetramine) is general purpose curing agent frequently used with liquid epoxy resins. Amine-type curing agent produces exothermic reaction which releases enough heat to cure at room temperature or low curing temperatures. The amount of hardener added to the epoxy is important. Glass beads were used to control the thickness of the adhesive layer. Moreover, silica can improve the bond

strength and to reduce the temperature coefficient of expansion of the epoxy. Thin bond layer minimizes creep, hysteresis, and linearity problems. (Measure resistance between strain grid and specimen, it should exceed 10000 MΩ) [55].

Application of the electrical strain gage is an important part of the experiment. The aluminum sample and composite carrier surfaces were sanded to obtain a smooth but not polished surface, traces of oil or grease were removed using acetone or alcohol, etching surface with appropriate acid, and neutralizing with a basic solution to give the proper chemical affinity for the adhesive. Aluminum samples were 10 inch by 1 inch according to the standards ASTM: D3039/D 3039M-00 Figure 3.6 illustrates the placement of the composite package and electrical strain gauges on the aluminum.

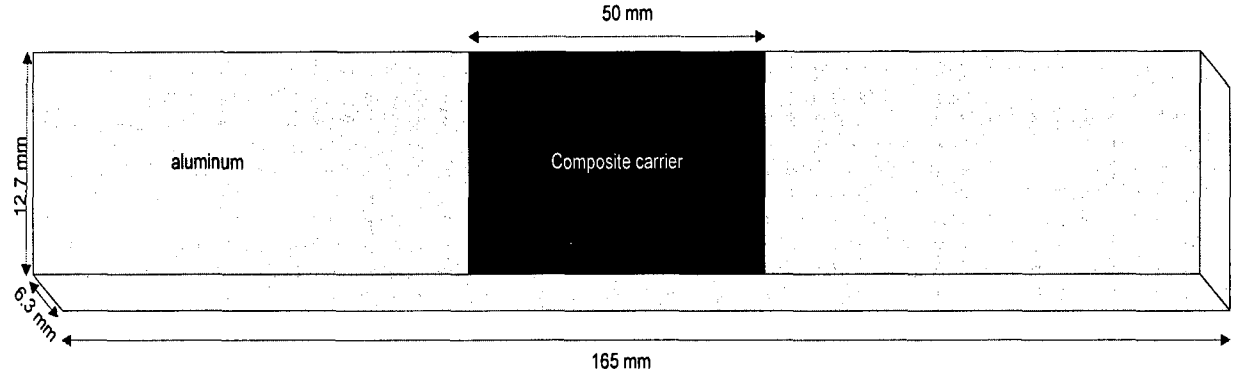

a

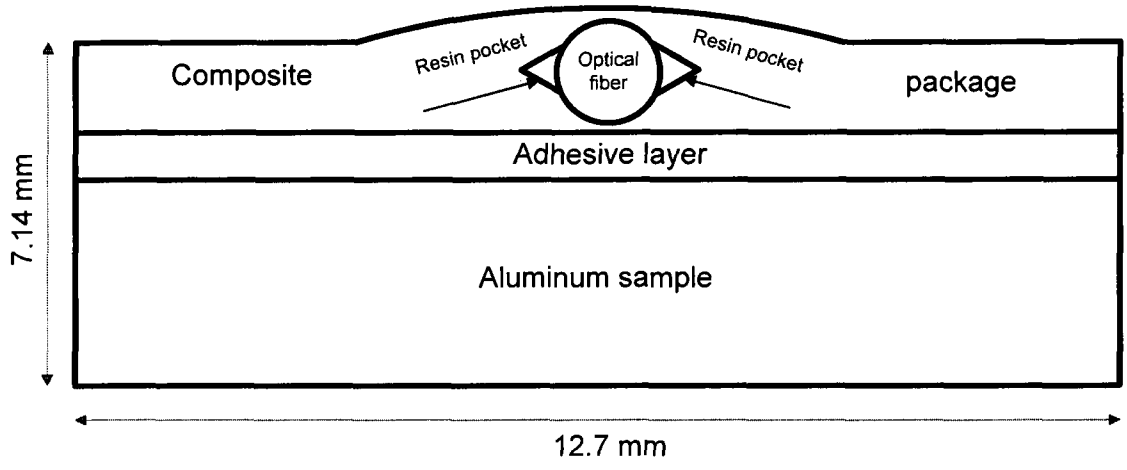

b

Figure 3.6. Schematics of the aluminum with packaged optical sensor and electrical strain gauges: a) full view; b) cross-section.

For tensile tests Optical Spectrum Analyzer (OSA) and tunable laser as light source were used. OSA, AQ 6319, has resolution 0.01 nm – 0.5 nm and sensitivity $\leq \pm 10$ pm. Tunable laser, Anritsu, MG 9541A, was used to apply light to the optical network in first series of tensile tests at 1550 nm wavelength, and laser from ILX Lightwave company was used for second series of tensile tests at 1559 nm wavelength applied to the optical network. Optical network consisted of the single mode fiber with tips covered with aluminum using metallization in clean room to achieve mirrored end; two 2 x 1 optical couplers (wavelength insensitive couplers) in order to split the signal in 50/50 to the sensing and reference arms and then send reflected waves to the OSA. Adapters were used to connect the optical fiber to the optical couplers in the first series of tensile tests and electrical splicing – for second series of tensile tests. LabView was used to acquire the power output from the optical network. Electrical strain gauges were adjusted to the aluminum

sample and to the composite package in order to compare the strain in both mechanical materials due to applied force. General purpose strain gauges from Vishay were purchased. Acquisition system for electrical strain gauges to read the strain was from Intertechnology Measurements. Figure 3.7 illustrates the equipment set up for tensile tests.

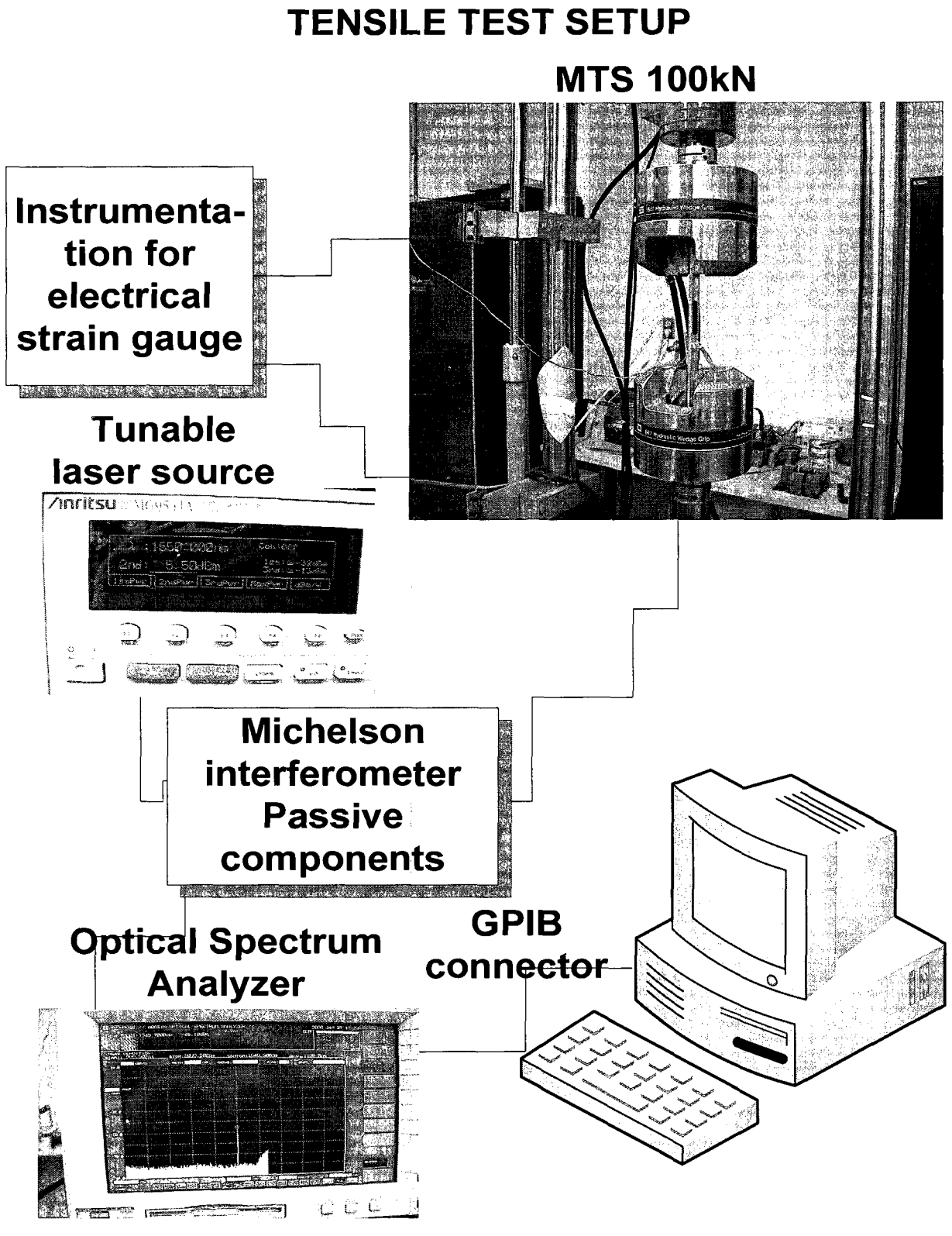

Figure 3.7 Tensile test setup.

3.3.2.1. Tensile test with 250 micrometer thickness of adhesive layer, CYCOM®5276-1, fabrication #1.

In this test force was applied on the aluminum samples with attached composite packages with the rate 100N/sec. to maximum 21 kN in order to obtain 2000 με in aluminum substrate. Four composite designs were investigated for application as composite carrier for optical sensor. These designs are [0/0/F(0)/0/0], [90/90/F(0)/90/90], [-45/45/F(0)/45/-45], [-60/60/F(0)/60/-60]. Table 3.3 presents output characteristics of the packaged optical sensors before tensile test.

Table 3.3. Output characteristics of the packaged optical sensors before tensile test.

Composite material	Package design	Power, μW	Visibility, V	Initial phase shift, rad.
CYCOM®5276-1, 250 μm	[0/0/F(0)/0/0]	91.63	0.7	-0.58656
	[-60/60/F(0)/60/-60]	7.05	0.7	-3.6483
	[-45/45/F(0)/45/-45]	38.58	0.7	-5.67514
	[90/90/F(0)/90/90]	3.77	0.7	-2.22953
CYCOM®5276-1, 100 μm	[-60/60/F(0)/60/-60]	50.05	0.31	-4.06654
	[90/90/F(0)/90/90]	16.4	0.68	-4.00608
NCT301, 100 μm	[-45/45/F(0)/45/-45]	4.55	0.34	2.52897
	[90/90/F(0)/90/90]	78.06	0.9	-3.027
	[-60/60/F(0)/60/-60]	2.852	0.42	2.14668

The initial phase shift appears due to the difference in length between the sensing and reference arms, and due to fabrication, shrinkage of package due to the decrease in temperature. Table 3.4 represents the dimensions of the composite carriers, length, l, thickness, t, and width, w, and length of the reference and sensing arms, l_r and l_s respectively, in Michelson interferometer.

Table 3.4. Geometry of the composite carriers and Michelson interferometer:

3.4(a) CYCOM®5276-1 composite material, thickness of adhesive layer 250 μm;

Design of the laminate	l, mm	w, mm	t, mm	l_r, mm	l_s, mm
[0/0/F(0)/0/0]	54	31	0.8	765	827
[90/90/F(0)/90/90]	55.6	32.4	0.68	765	830
[-45/45/F(0)/45-45]	53.9	33.0	0.9	765	813.5
[-60/60/F(0)/60/-60]	55.6	34.5	0.9	765	827

3.4(b) CYCOM®5276-1 composite material, thickness of adhesive layer 100 μm;

Design of the laminate	l, mm	w, mm	t, mm	l_r, mm	l_s, mm
[-60/60/F(0)/60/-60]	51.08	31.34	0.7	846	1486
[90/90/F(0)/90/90]	59.79	23.9	0.7	846	1220

3.4(c) NCT 301 composite material, thickness of adhesive layer 100 μm.

Design of the laminate	l, mm	w, mm	t, mm	l_r, mm	l_s, mm
[-60/60/F(0)/60/-60]	50.7	26.8	0.55	1307	1257
[90/90/F(0)/90/90]	51.5	26.29	0.5	1307	1317.5
[-45/45/F(0)/45/-45]	50.8	27.0	0.52	1307	1292

(1) Tensile test with [0/0/F(0)/0/0] package with 250 micrometer adhesive layer.

Strain on aluminum sample had much higher value than it was on the composite package due to applied force. This result is due to the different stiffnesses in these materials. Composite package is strong and in the first application of force curvature appears on the top of the package and cracks inside the adhesive layer. The results showed that [0/0/F(0)/0/0] design of package is not apropriate design. It is stiffer compared to the aluminum.

(2) Tensile test with [90/90/F(0)/90/90] package with 250 micrometer adhesive layer.

Axial force was applied on the aluminum sample three times. The difference between the strain values on composite package and in aluminum samples can be seen from Figure 3.8, where the average values of strain and standard deviation versus applied force in electrical strain gauges on the aluminum sample and on the composite carrier and calculated strain from Michelson Interferometer were illustrated.

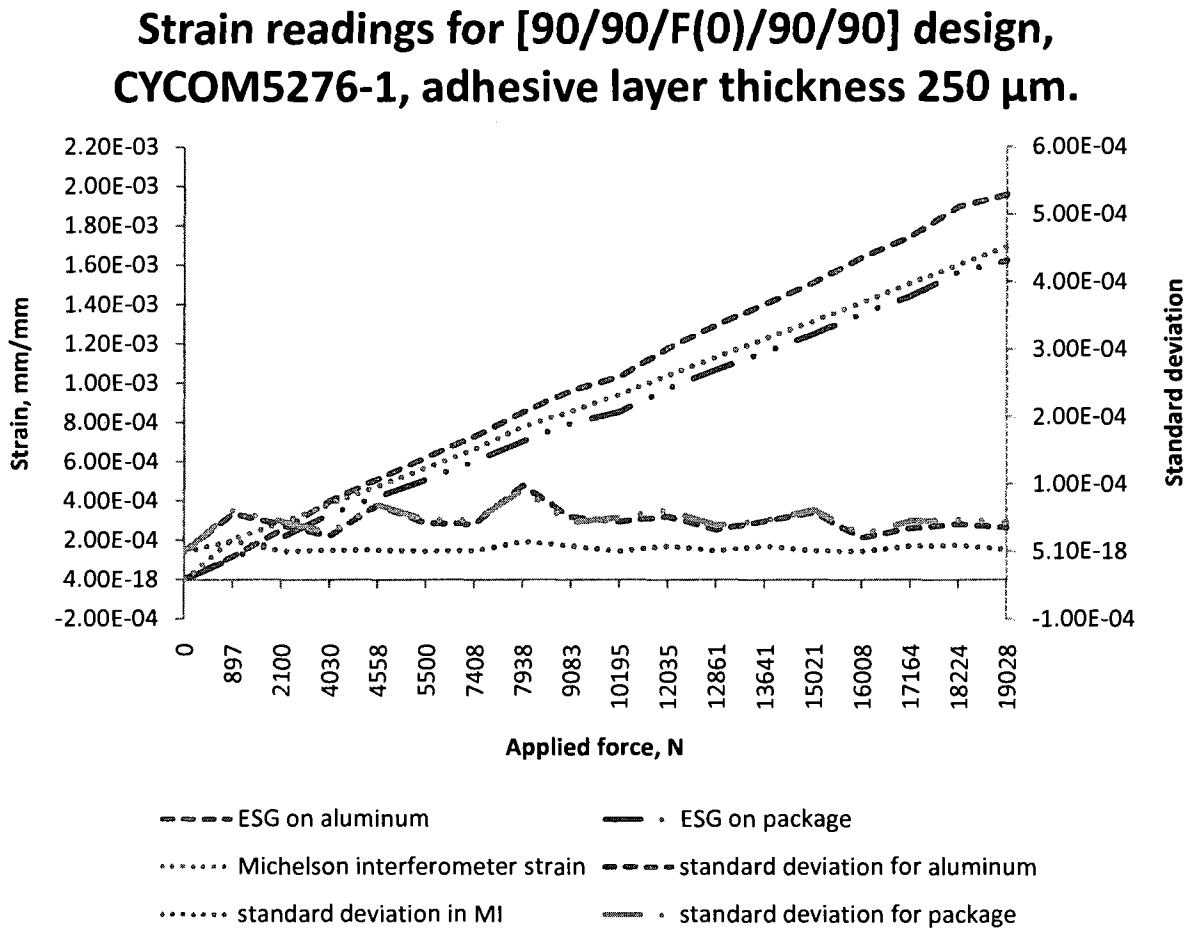

Figure 3.8. Tensile test, [90/90/F(0)/90/90], 250 µm adhesive layer, average values of strain readings from electrical strain gauges and Michelson interferometer and their standard deviation versus applied force.

The difference between data from electrical strain gauges on the aluminum sample and composite package is not very high according to the graph readings. For strain calculations in Michelson interferometer assumption was made that each 11 seconds 6 cycles were lost due to the speed of applied force on the aluminum. Strain readings from Michelson interferometer were compared to the strain data from electrical strain gauges.

Uniform increase was observed in all three repetitions with slight difference in values, standard deviation represents this variance of the values.

(3) Tensile test with [-45/45/F(0)/45/-45] package with 250 micrometer adhesive layer

Force was applied on the aluminum sample from 0 N to 21 kN three times and the strain readings from electrical strain gauges which were placed on aluminum sample and on the composite package were compared with strain from optical sensor embedded in composite carrier. Aluminum sample had cross section area 160.02 mm^2. From the tensile test strain readings this package illustrated inadequate performance, it did not elongate with the sample due to the high stiffness of this design layup in composite carrier. The composite carrier did not increase in length and the difference between aluminum and composite package was almost 100%. The reason for this behavior is the high stiffness of the composite package. The top of the package was tend to curve due to the strain on the bottom part. The simulations illustrated this tendency of the package to the curvature for applied strain on the bottom of the package.

(4) Tensile test with [-60/60/F(0)/60/-60] package with 250 micrometer adhesive layer.

Figure 3.9 shows the strain versus applied force between strain gauge data from composite package and from aluminum sample and from embedded optical sensor.

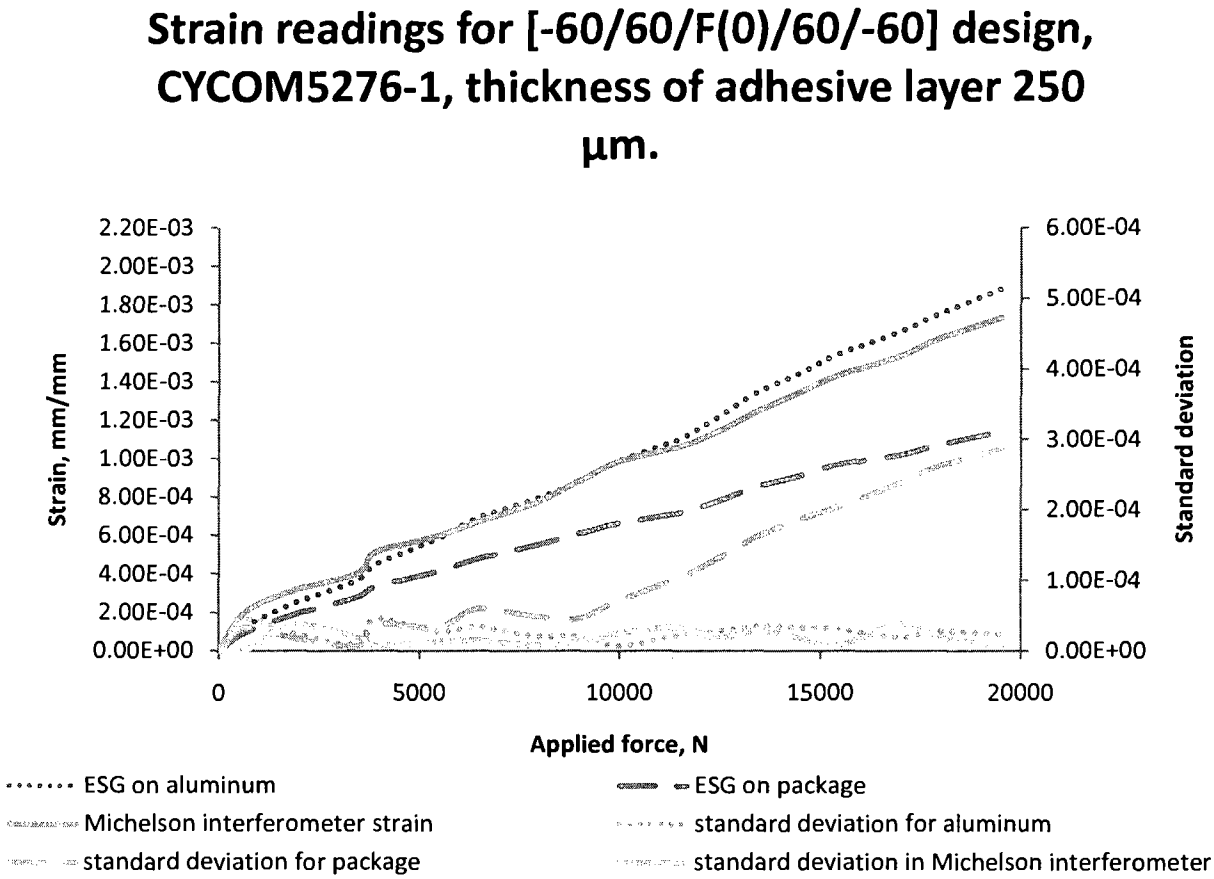

Figure 3.9. Tensile test, 250 µm adhesive layer thickness, [-60/60/F(0)/60/-60], strain readings from electrical strain gauges and Michelson interferometer versus applied force.

From this data it can be seen that package and aluminum sample have comparable output in strain at the start. However, the difference between the strain values on the package and strain readings on the aluminum increased with increase in applied force on the aluminum. This is due to the decreased transmission of the strain through adhesive layer. Assumption was made that 6 cycles were lost during elongation of the optical fiber due to the fast increase in strain. Maximum 114 cycles were lost according to the assumption. Strain readings in Michelson interferometer were comparable to the strain data from

electrical strain gauge on the aluminum sample. Table 3.5 illustrates the data, differences in strain between optical sensor and package, D_{o-p}, differences in strain between aluminum and package, D_{a-p}, and differences in strain between aluminum and optical sensor, D_{a-o}, from tensile test with composite package designs [90/90/F(0)/90/90] and [-60/60/F(0)/60/-60]. The thickness of the adhesive layer was taken as 250 μm.

Table 3.5. Tensile tests, [90/90/F(0)/90/90] and [-60/60/F(0)/60/-60] lay-up designs, thickness of the adhesive layer 250 μm, strain readings from aluminum, composite carrier and MI, and difference estimations.

CYCOM®5276-1	ESG on aluminum, με	Strain in optical fiber, με	ESG on package, με	D_{o-p}, %	D_{a-p}, %	D_{a-o}, %
[90/90/F(0)/90/90]	1955	1690	1619	4.2	17.2	13.6
[-60/60/F(0)/60/-60]	1882	1732	1141	34.1	39.4	8.0

Difference between optical sensor and package is around 4 %, and difference between electrical strain gauge on the aluminum sample and the one on the composite carrier is around 17%. The strain readings in optical sensor are less than strain data on aluminum sample and higher than microstrain data on the composite package. Difference in strain readings between strain gauge on aluminum and optical sensor is less than 10%. This design of the composite package gave the smallest difference in strain readings between strain in aluminum sample and optical sensor. However, difference between the strain on

the package and strain from optical sensor could be enlarged due to the assumption made for calculation of the strain from Michelson interferometer.

3.3.2.2. Tensile test with 100 micrometer thickness of adhesive layer, fabrication #1, CYCOM®5276-1.

Two composite designs were investigated for application as composite carrier for optical sensor. These designs are [90/90/F(0)/90/90] and [-60/60/F(0)/60/-60].

The initial phase shift appears due to the difference in length between the sensing and reference arms, and due to fabrication, shrinkage of package due to the decrease in temperature. The instrumentation for the tensile tests was the same as before and listed in Table 3.5, where laser source2 was utilized.

(1) Tensile test with [-60/60/F(0)/60/-60] package with 100 micrometer adhesive layer thickness.

Force was applied on the aluminum sample from 0 N to 21 000 N three times with rate 60 N per second, and the strain readings from electrical strain gauges which were placed on aluminum sample and on the composite package were compared with strain from optical sensor embedded in composite carrier. Aluminum sample had cross section area 160.02 mm^2. Figure 3.10 shows the strain versus applied force between strain gauge data from composite package, aluminum sample, and from Michelson interferometer.

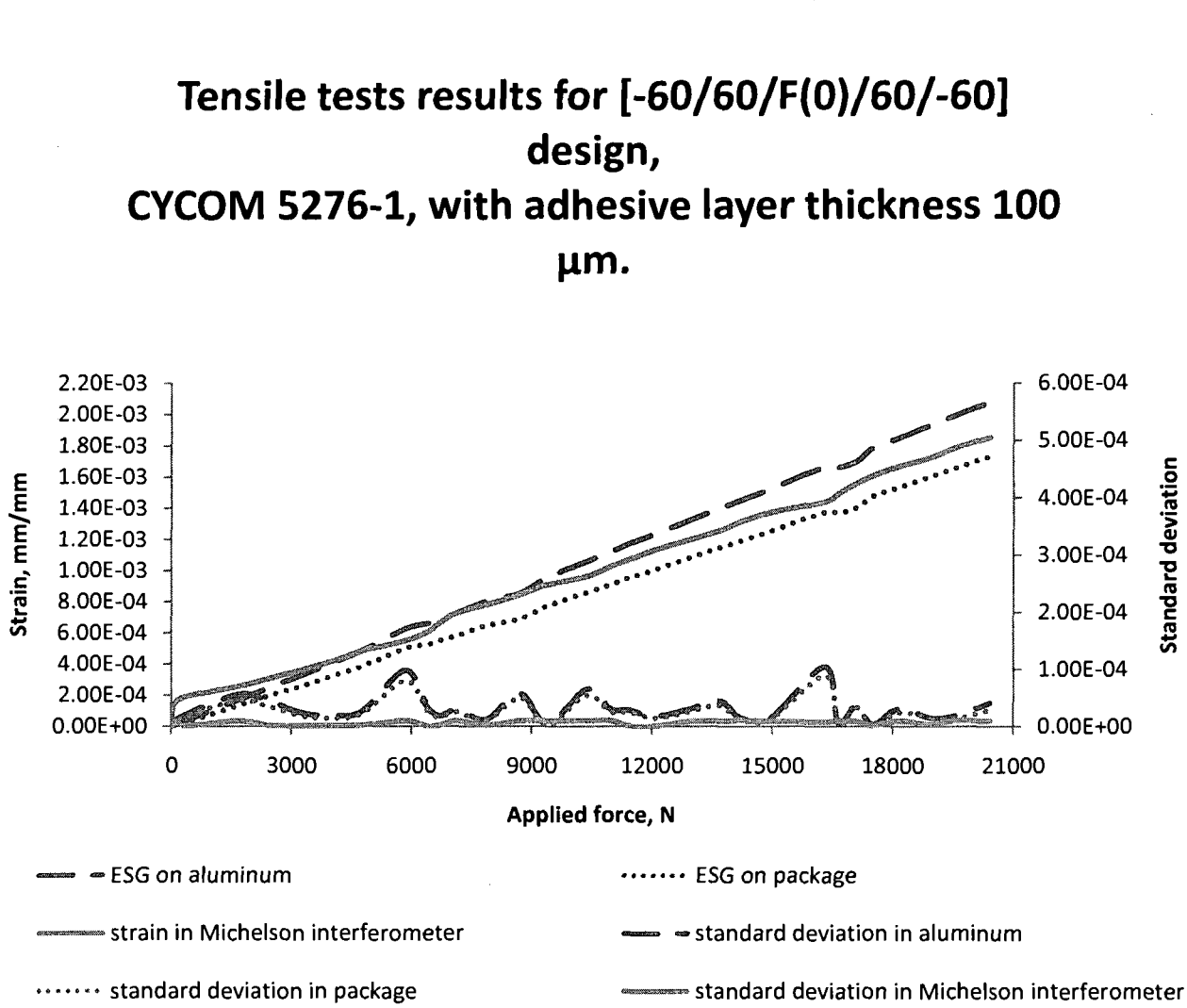

Figure 3.10. Tensile test, 100 μm adhesive layer thickness, [-60/60/F(0)/60/-60] design.

From this data it can be seen that package and aluminum sample had comparable output in strain measurements with optical sensor readings. Assumption was made that 3.5 cycles were lost during elongation of the optical fiber due to the fast increase in strain. Maximum 112 cycles were lost according to the assumption. Strain in Michelson interferometer is comparable to the strain in electrical strain gauge on the aluminum sample.

(2) Tensile test with [90/90/F(0)/90/90] package with 100 micrometer adhesive layer thickness.

Force was applied on the aluminum sample from 0 N to 21 kN three times at a rate of 60 N per second, and the strain readings from electrical strain gauges which were placed on aluminum sample and on the composite package were compared with strain from optical sensor embedded in composite carrier. Aluminum sample had cross section area 160.02 mm^2. Figure 3.11 shows the strain versus applied force between strain gauges data from composite package and from aluminum sample and Michelson interferometer.

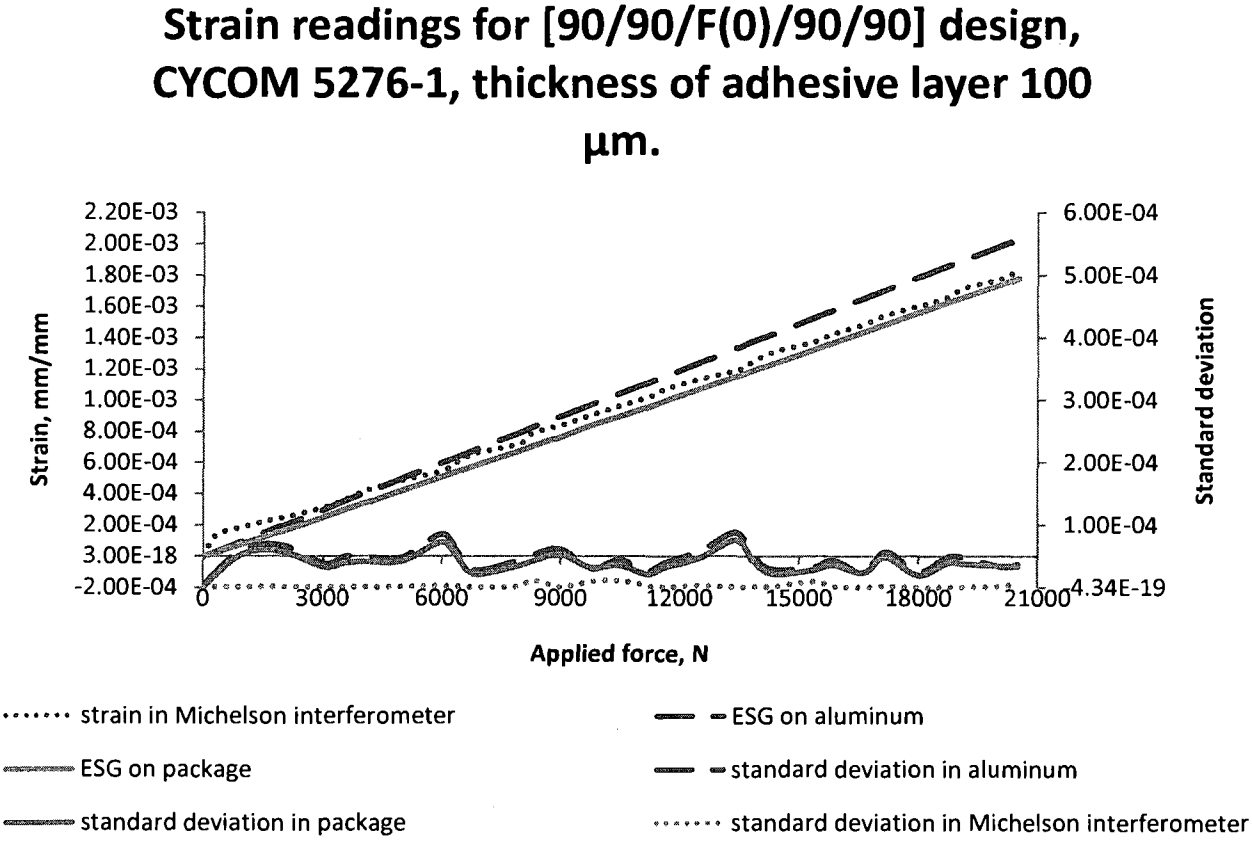

Figure 3.11. Tensile test, 100 µm adhesive layer thickness, [90/90/F(0)/90/90], strain versus applied force, CYCOM 5276-1.

From this data it can be seen that package and aluminum sample have comparable output in strain measurements. Assumption was made that 3.5 cycles were lost during elongation of the optical fiber due to the fast increase in strain. Maximum 112 cycles were lost according to the assumption. assumption. Strain is comparable to the strain in electrical strain gauge on the aluminum sample. Table 3.6 illustrates the data, difference in strain between optical sensor and package, D_{o-p}, difference in strain between aluminum and package, D_{a-p}, and difference in strain between aluminum and optical sensor, D_{a-o}, from tensile test with composite package designs [90/90/F(0)/90/90] and [-60/60/F(0)/60/-60] and thickness of the adhesive layer 100 μm.

Table 3.6. Tensile tests, [-60/60/F(0)/60/-60] and [90/90/F(0)/90/90] lay-up designs, 100 μm adhesive layer thickness, strain reading from optical and electrical sensors, and difference estimations.

CYCOM®5276-1	ESG on aluminum, με	Strain in optical fiber, με	ESG on package, με	D_{o-p}, %	D_{a-p}, %	D_{a-o}, %
[-60/60/F(0)/60/-60]	2078	1851	1729	6.6	16.8	10.9
[90/90/F(0)/90/90]	2030	1846	1777	3.7	12.5	9.1

Difference between strain gauge on aluminum and optical sensor was around 10.9% for [-60/60/F(0)/60/-60] lay-up, and difference between strain gauge on aluminum and optical sensor was around 9.1%.

3.3.2.3. Tensile test with 100 micrometer thickness of adhesive layer, fabrication #2, NCT 301.

Tensile tests were similar to the tests done with CYCOM®5276-1. Maximum 21000N were applied on the aluminum samples with 20N/sec. speed. The thickness of the adhesive layer was 100 μm. Dimensions of the samples included in Table 3.4. The results from tensile tests for [90/90/F(0)/90/90], [-45/45/F(0)/45/-45], and [-60/60/F(0)/60/-60] designs of the composite carriers are represented in Figure 3.12.

Strain readings for [-60/60/F(0)/60/-60] design, NCT301, thickness of adhesive layer 100 µm.

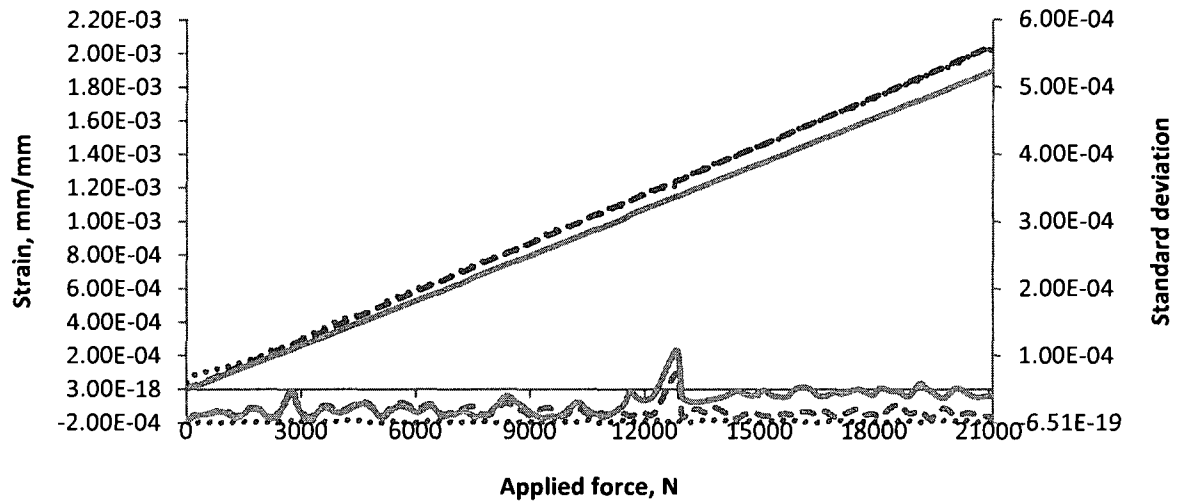

a

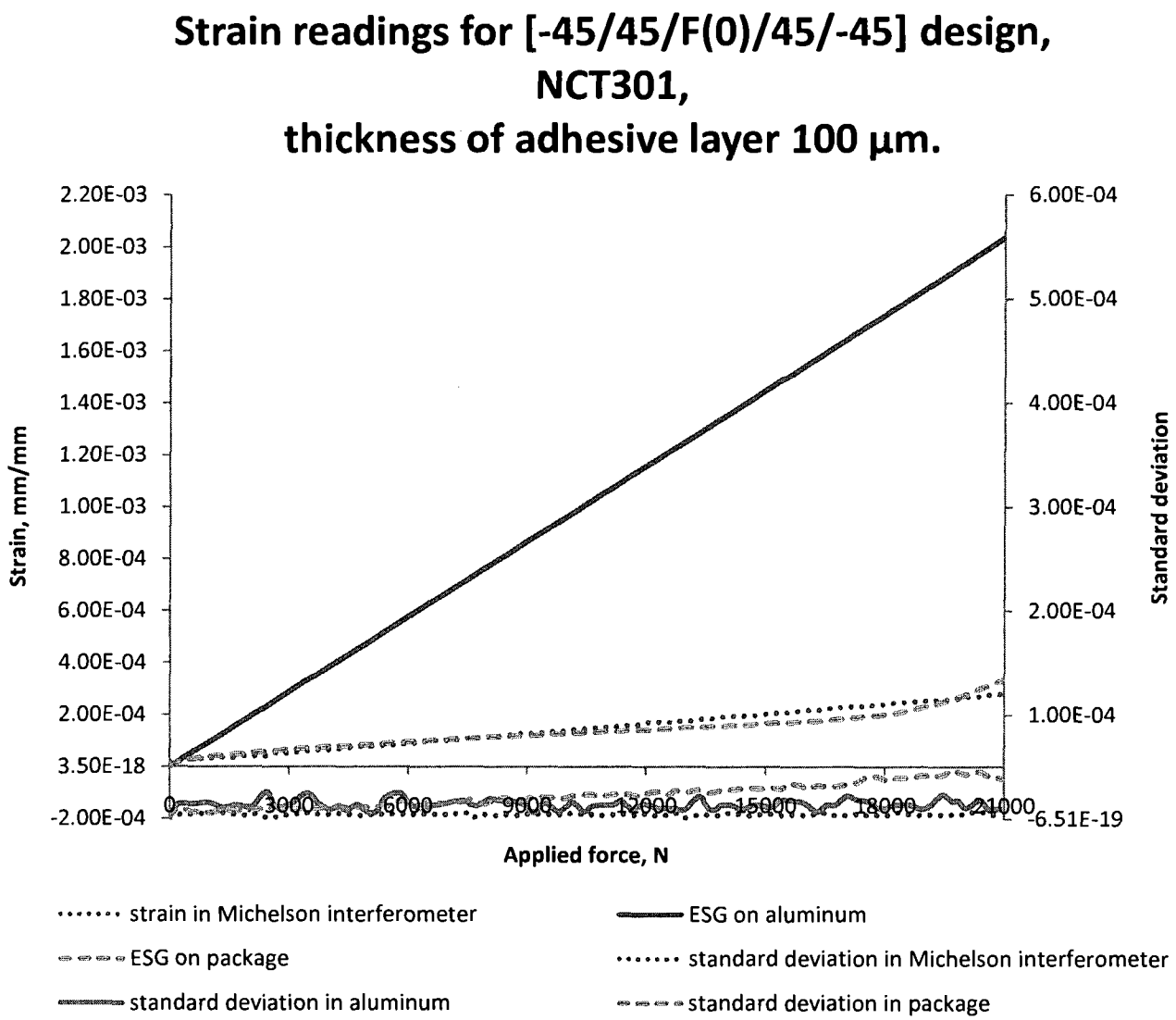
Strain readings for [-45/45/F(0)/45/-45] design,
NCT301,
thickness of adhesive layer 100 μm.
2.20E-03
2.00E-03
1.80E-03
1.60E-03
1.40E-03
1.20E-03
1.00E-03
8.00E-04
6.00E-04
4.00E-04
2.00E-04
3.50E-18
-2.00E-04
Strain, mm/mm
6.00E-04
5.00E-04
4.00E-04
3.00E-04
2.00E-04
1.00E-04
-6.51E-19
Standard deviation
0
3000
6000
9000
12000
15000
18000
21000
Applied force, N
strain in Michelson interferometer
ESG on aluminum
ESG on package
standard deviation in Michelson interferometer
standard deviation in aluminum
standard deviation in package

b

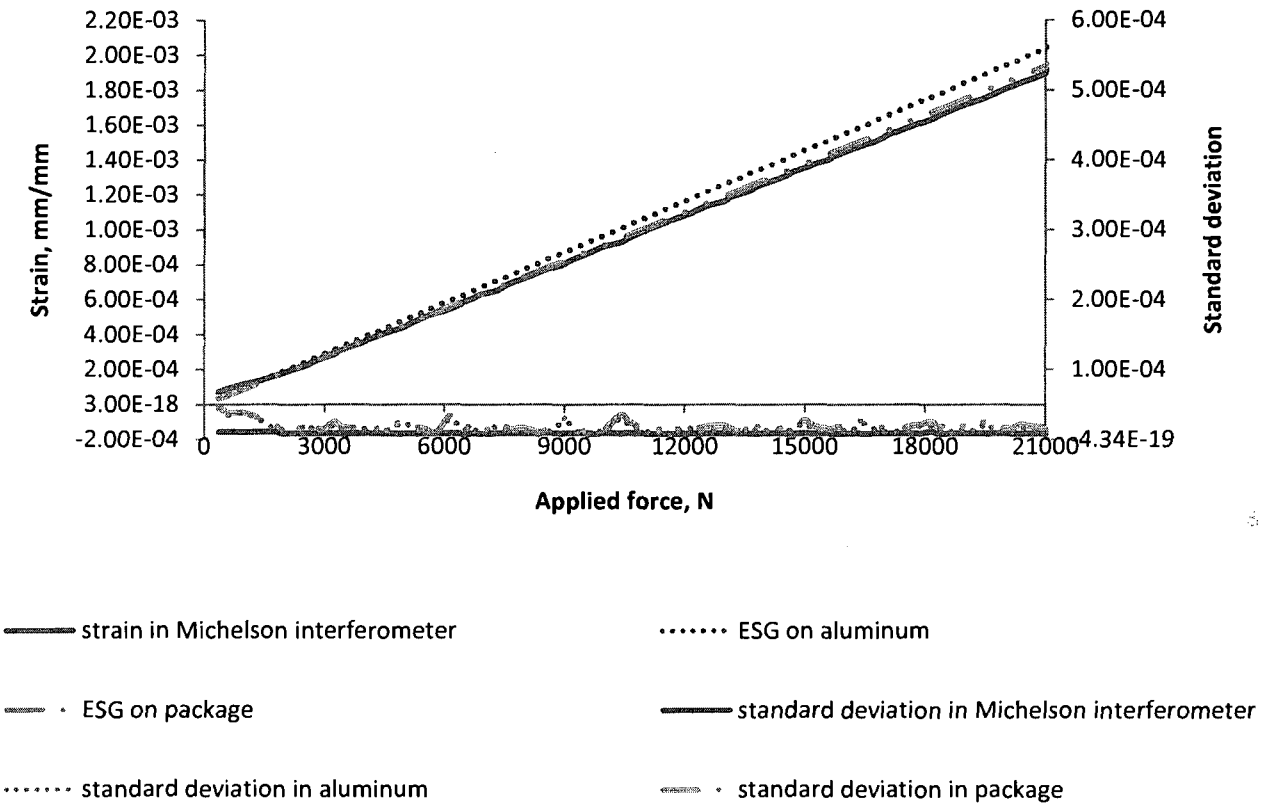

c

Figure 3.12. Tensile tests, 100 μm adhesive layer thickness,NCT301 composite material strain readings versus applied force for three fabricated composite carrier designs such as a) [-60/60/F(0)/60/-60]; b) [-45/45/F(0)/45/-45]; and c) [90/90/F(0)/90/90].

From this data it can be seen that packages and aluminum samples had comparable outputs in strain measurements with optical sensor readings for [90/90/F(0)/90/90] and [-60/60/F(0)/60/-60] designs. Assumption was made that 1.4 cycles were lost during elongation of the optical fiber due to the fast increase in strain in 11.8 sec. Maximum 124 cycles were lost according to the assumption. Strain readings in Michelson interferometer were comparable to the strain data in electrical strain gauges on the aluminum sample. Table 3.7 illustrates the data, difference in strain between optical sensor and package, D_{o-p}, difference in strain between aluminum and package, D_{a-p}, and difference in strain between aluminum and optical sensor, D_{a-o}, from tensile test with composite package designs [90/90/F(0)/90/90] and [-60/60/F(0)/60/-60] and thickness of the adhesive layer 100 μm.

Table 3.7. Tensile tests, NCT301 composite material, strain readings from sensors, and difference estimations.

Design of the composite package	ESG on aluminum, με	Strain in optical fiber, με	ESG on package, με	D_{o-p}, %	D_{a-p}, %	D_{a-o}, %
[-60/60/F(0)/60/-60]	2039	2020	1892	6.3	7.2	0.9
[-45/45/F(0)/45/-45]	2031	280	330.9	18.2	83.7	86.2
[90/90/F(0)/90/90]	2044	1907	1943	1.9	4.9	6.7

The variation of the results illustrated in Table 3.7 confirmed that [90/90/F(0)/90/90] composite design has less difference than all others designs. However, design

[-60/60/F(0)/60/-60] was improved for NCT301 composite material due to the reduced stiffness of the composite material used for fabrication of the composite package.

3.3.3 Difference in results for tensile tests.

In summary, composite packages with high Young's modulus were stiffer than aluminum substrate; therefore, they were as reinforcement for aluminum in the place where they were bonded. Practically, they did not elongate, they curved, and bonding between aluminum sample and composite package was decreased because of the curvature. Therefore, difference estimation was done for two most successful designs such as [-60/60/F(0)/60/-60] and [90/90/F(0)/90/90] for CYCOM®5276-1 and NCT301. Figure 3.13 illustrates the error results between electrical strain gauge on the aluminum and electrical strain gauge on composite carrier, and between electrical strain gauge on aluminum and optical sensor for these designs.

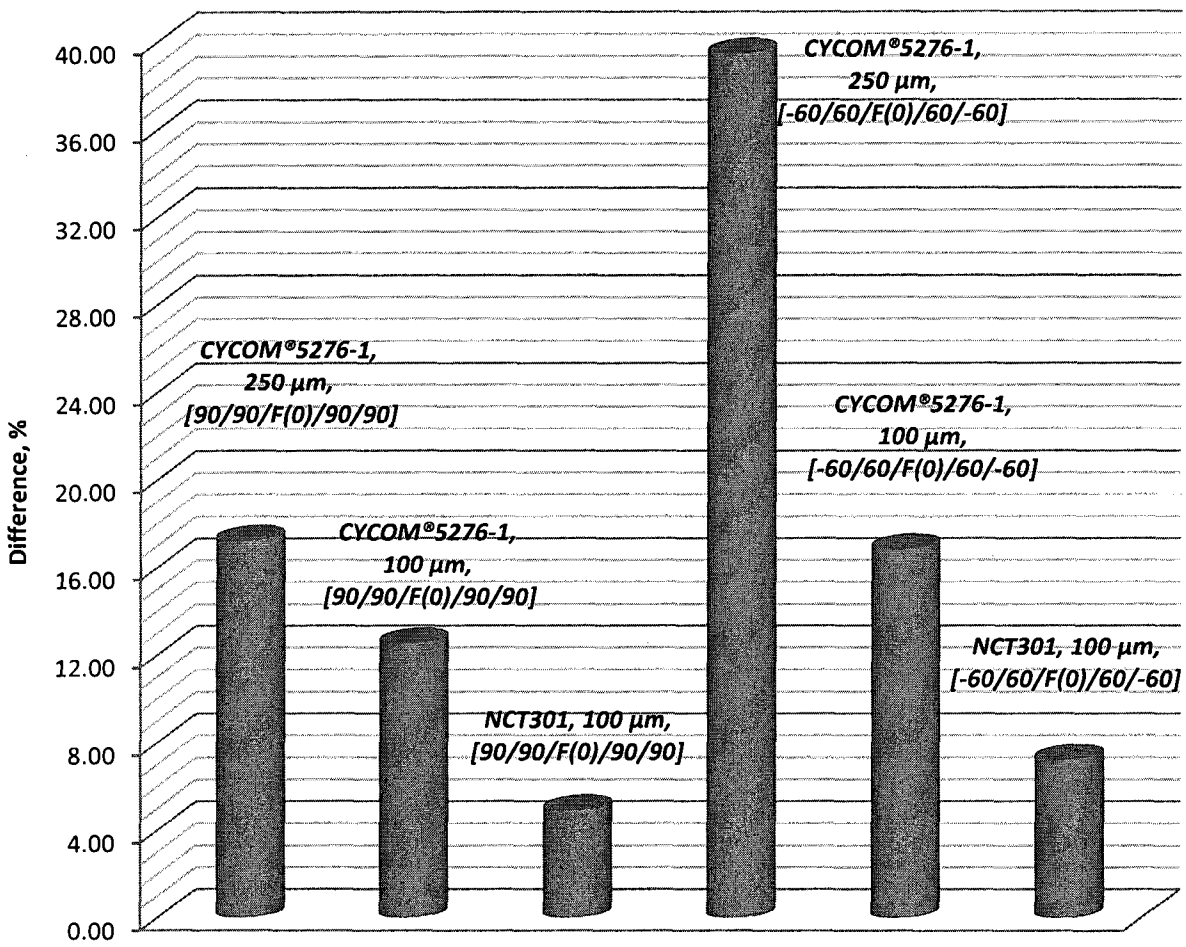
Difference between strain readings on aluminum and on composite package.
Difference, %
40.00
36.00
32.00
28.00
24.00
20.00
16.00
12.00
8.00
4.00
0.00
CYCOM®5276-1, 250 µm, [90/90/F(0)/90/90]
CYCOM®5276-1, 100 µm, [90/90/F(0)/90/90]
NCT301, 100 µm, [90/90/F(0)/90/90]
CYCOM®5276-1, 250 µm, [-60/60/F(0)/60/-60]
CYCOM®5276-1, 100 µm, [-60/60/F(0)/60/-60]
NCT301, 100 µm, [-60/60/F(0)/60/-60]

a

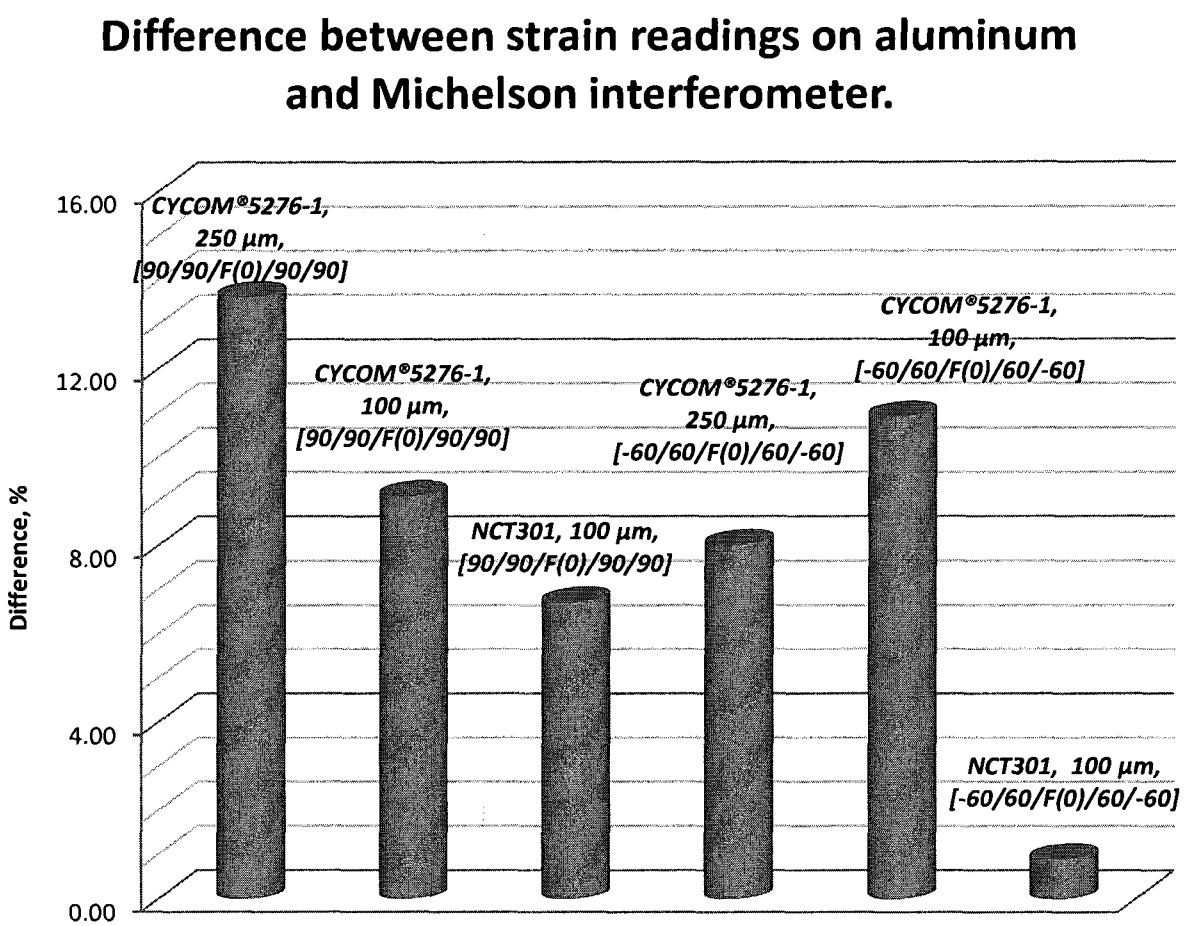

b

Figure 3.13. Difference between strain readings in CYCOM®5276-1 and NCT301 composite carriers: a) on aluminum and on composite package; b) on aluminum and Michelson interferometer.

The thin adhesive layer and less stiff package will be cause for minor variance in strain results between ESGs and between aluminum and optical sensor. Composite material with less stiffness represented less difference between aluminum and composite package and between aluminum and Michelson interferometer.

3.4 Microscopic results for tensile tests

Microscopic measurements were performed in order to obtain geometry of the resin pocket and distribution of the layers. The results were used for creation of the models in ANSYS. These models were used to perform the simulations and static analysis results were compared with the tensile tests outputs.

3.4.1 Microscopic results for composite carriers from CYCOM®5276-1 composite material.

After tensile tests the aluminum samples with bonded composite carriers were cut in the middle of the package, microscopic observations were performed for CYCOM®5276-1 composite carriers. The position of the optical fiber inside the composite package was investigated. Next step was cutting samples to small pieces in order to grind and polish them. Grinding and polishing were done according standard procedure for composites. Optical microscope was used to capture the images of the optical fiber inside the composite packages with 50x magnifications including camera and lenses. Figure 3.14 presents microscopy results for 250 micrometer adhesive layer for CYCOM®5276-1.

[0/0/F(0)/0/0]

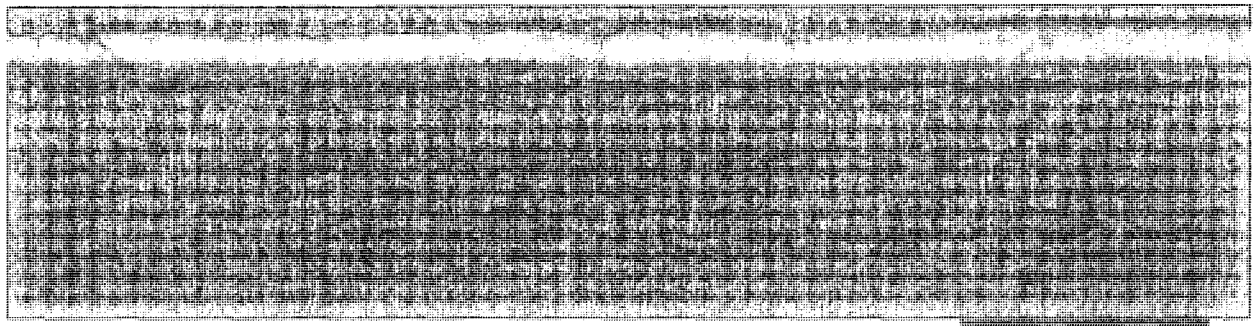

a

[-60/60/F(0)/60/-60]

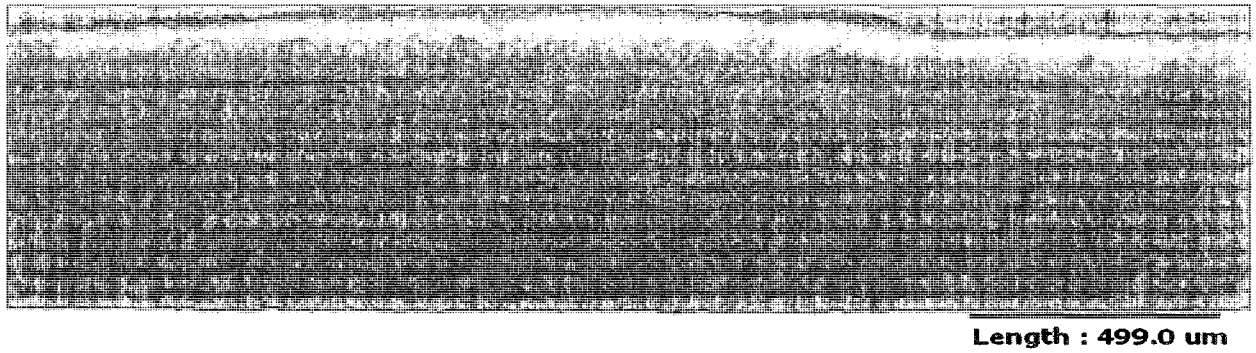

b

[-45/45/F(0)/45/-45]

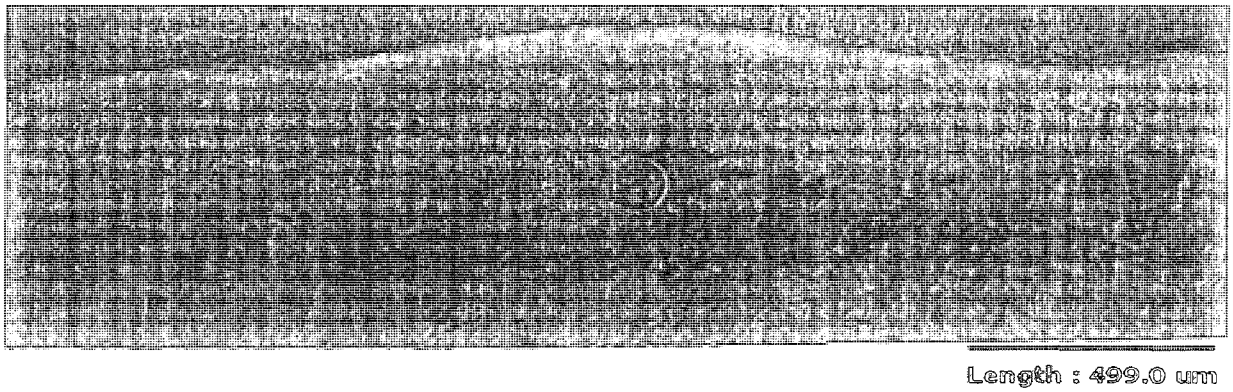

c

[90/90/F(0)/90/90]

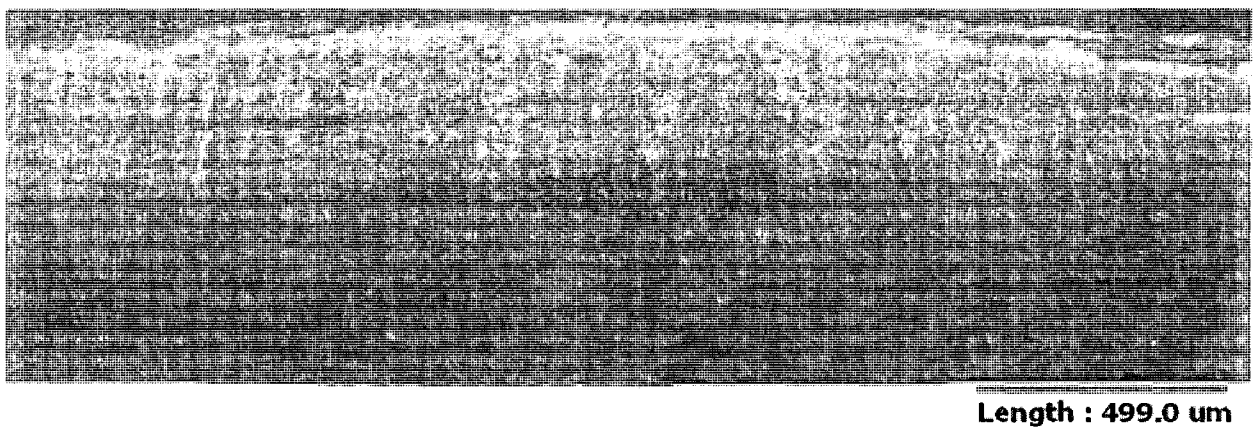

d

Figure 3.14. Microscopic results for samples with 250 micrometer adhesive layer a) [0/0/F(0)/0/0]; b) [-60/60/F(0)/60/-60], c) [-45/45/F(0)/45/-45]; and d) [90/90/F(0)/90/90] designs.

The microscopic results revealed that the negligible resin pocket will be in lay-up [0/0/F(0)/0/0] and the large resin pocket will be for designs [90/90/F(0)/90/90] and [-60/60/F(0)/60/-60]. Thin layers of the resin presented in all composite packages. These layers can be the cause for higher difference between strain values on aluminum and on composite package. Figure 3.15 illustrates microscopic results for 100 micrometer adhesive layer for composite carriers from CYCOM®5276.

[90/90/F(0)/90/90]

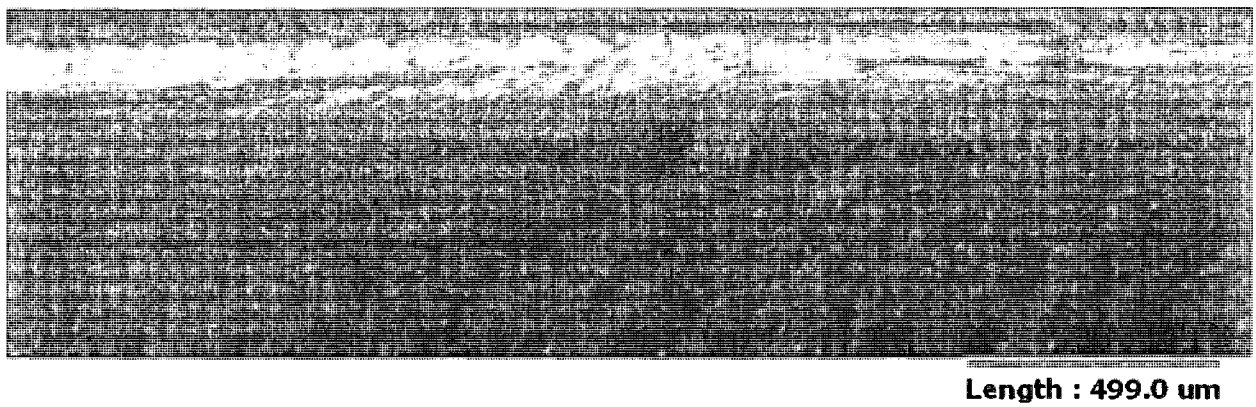

a

[-60/60/F(0)/60/-60]

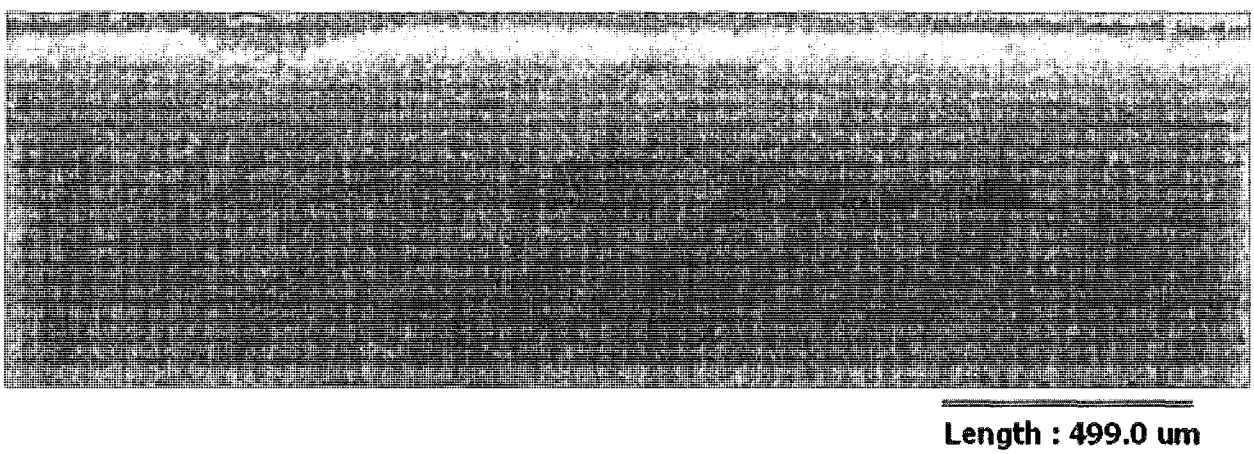

b

Figure 3.15. Microscopic results for samples with 100 micrometer adhesive layer a) [90/90/F(0)/90/90] and b) [-60/60/F(0)/60/-60] designs.

In both cases resin layers were presented. These layers can be the cause of the difference in strain readings between composite carrier and aluminum. Hence, the transmission of the strain through composite package was altered.

3.4.2 Microscopic results for composite carriers from NCT301 composite material.

Microscopic results were performed on the fabricated samples for [90/90/F(0)/90/90], [-45/45/F(0)/45/-45], and [-60/60/F(0)/60/-60] lay-ups of laminate. Figure 3.16 illustrates the microscopic images of these three composite packages.

[90/90/F(0)/90/90]

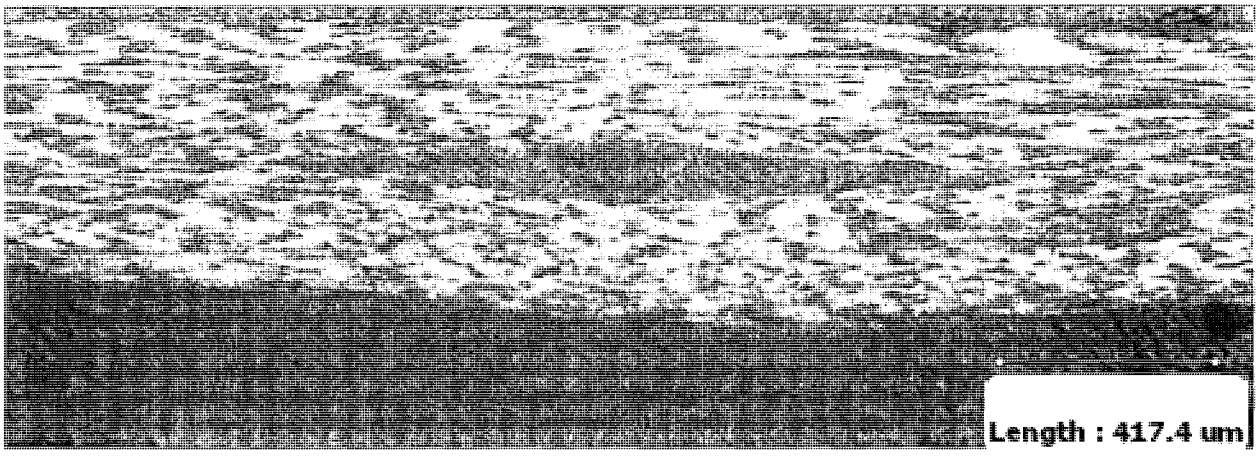

a

[-60/60/F(0)/60/-60]

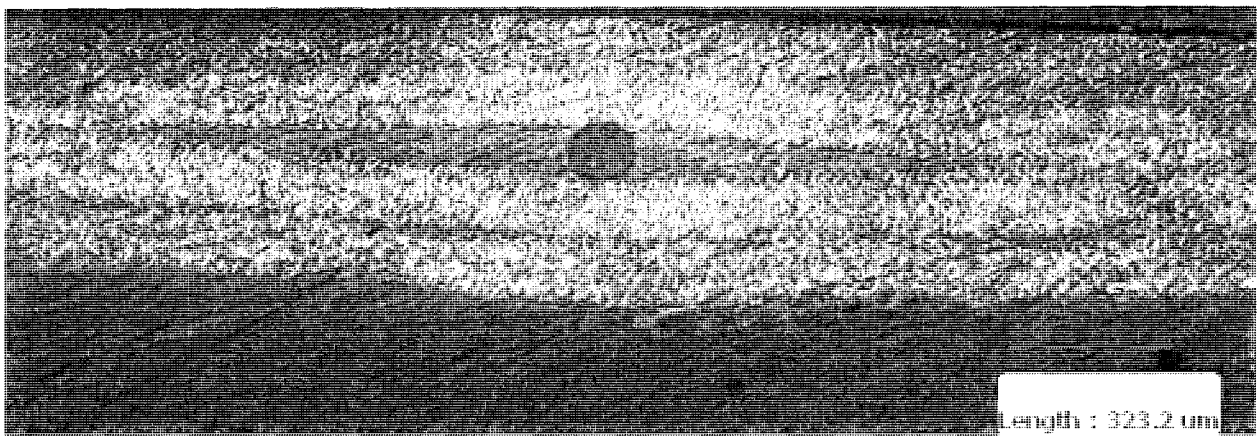

b

[-45/45/F(0)/45/-45]

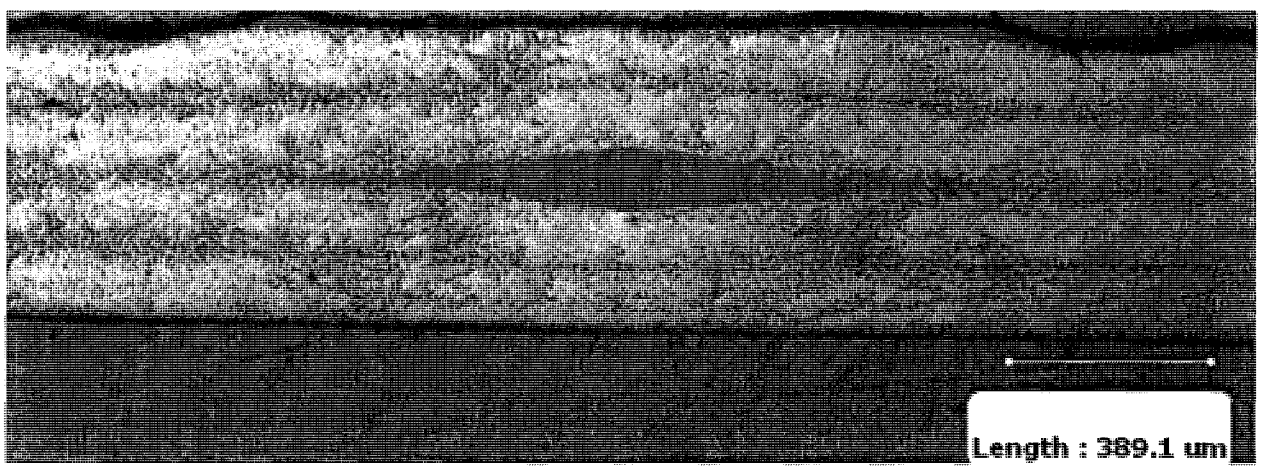

c

Figure 3.16. Microscopic results for samples with 100 micrometer adhesive layer a) [90/90/F(0)/90/90], b) [-60/60/F(0)/60/-60], and c) [-45/45/F(0)/45/-45] layup designs.

Microscopic results had shown that layers of resin were inside CYCOM®5276-1 composite carriers. These layers can be partially responsible for higher errors from strain readings apart from the stiffness of the material. Composite carriers from NCT301 material illustrated no resin layers. The resin pocket was observed in all samples. The geometry of the resin pockets were utilized for creation of the models in ANSYS.

CHAPTER 4

ANSYS SIMULATIONS

Simulations using ANSYS were performed based on the geometry of the composite packages used for tensile tests. The microscopic results were discussed previously in Chapter 3.

4.1 Preliminary ANSYS Simulations

SOLID92 was used for simulations. Solid92 has a quadratic displacement behavior and is well suited to model irregular meshes which were applied for packaging. The element is defined by ten nodes having three degrees of freedom at each node: translations in the nodal x, y, and z directions. The element also has plasticity, creep, swelling, stress stiffening, large deflection, and large strain capabilities.

Design includes four volumes which represent fiber, non symmetrical resin pocket, and two layers of the composite material. Different meshing size was applied for volumes.

The used version of the ANSYS has maximum 16000 nodes for meshing, and this is the reason for use only 10 cm length of the model for simulations. The size of the model is 100x 150 with maximum thickness in the middle 3.38. The size magnified by 10^4.

4.1.1 Simulations for three geometries of the resin pocket in composite carrier.

Based on the estimated geometry of the sample [0/F(0)/0] from microscopic results after fabrication #1 ANSYS simulations were performed for twice lager, twice smaller, and observed geometry of the resin pocket. Displacement 30 (3mm) was applied on the layer1, composite layer, area at x=100 and zero displacement at x-direction was applied on all areas, resin pockets, composite package, optical fiber, on the left side of the model. Figure 4.1 illustrates schematics of the model.

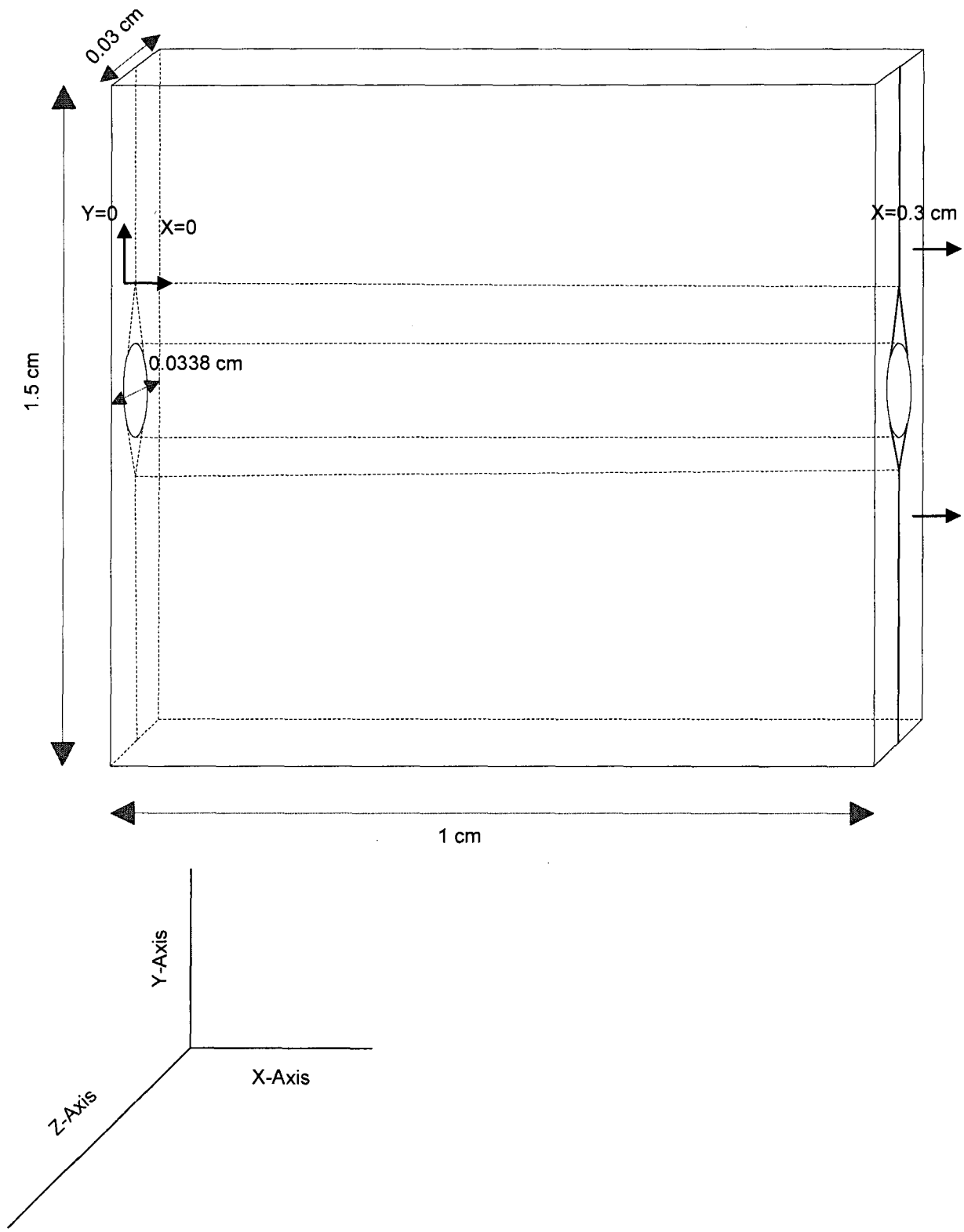

Figure 4.1. Schematics of the model used for simulations.

Paths in x- and y-directions were investigated and outcomes recorded in the tables for three models. Nodal solutions for strain and displacement were performed.

Strain output for optical fiber was compared for three geometries of the resin pocket. Figure 4.2 shows two geometries of the resin pocket.

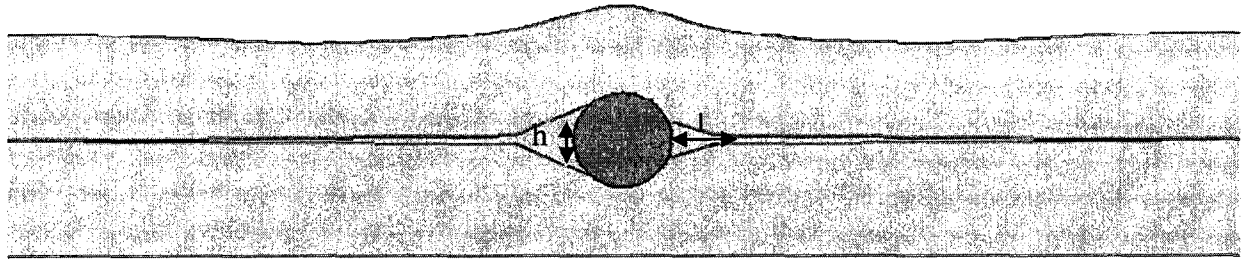

a

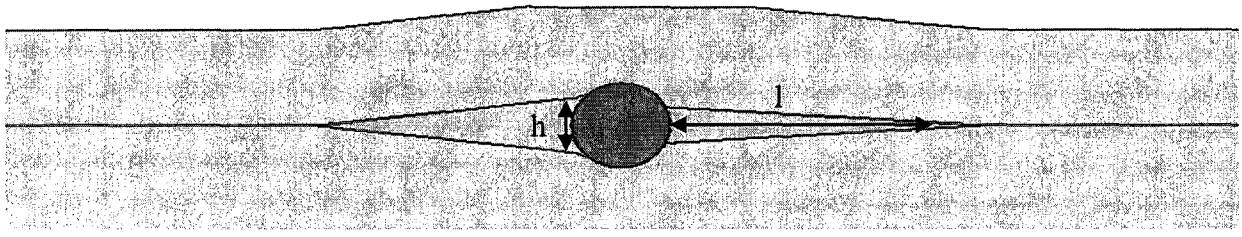

b

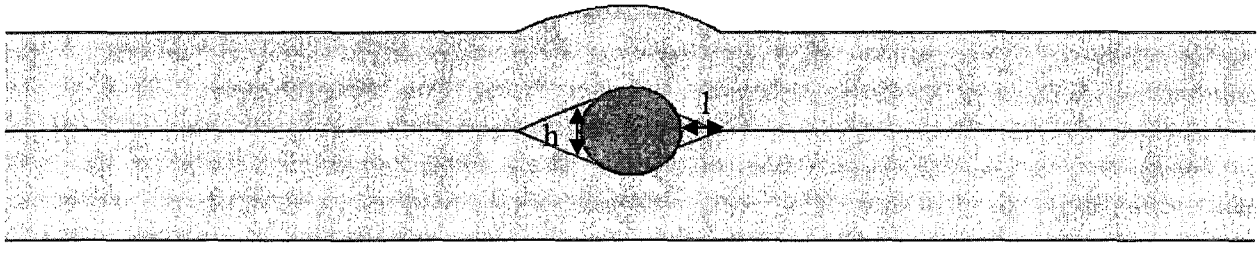

c

Figure 4.2 Resin pocket geometry a) real geometry, b) twice-larger, c) twice-smaller.

Design includes five volumes which represent fiber, resin pockets, and two layers of the composite material. Table 4.1 illustrates the geometries of the resin pockets used in these simulations such as height, h, and length, l.

Table 4.1. Geometries of the resin pocket.

Model	h/l of left resin pocket, m^2	h/l of right resin pocket, m^2
Real geometry	$2.6*10^{-8}$	$1.8*10^{-8}$
Twice-smaller	$1.3*10^{-8}$	$1.4*10^{-8}$
Twice-larger	$5.2*10^{-8}$	$3.6*10^{-8}$

The largest error corresponded to applied strain 3000με had model with the increased resin pocket model, and the smallest error – model with decreased resin pocket geometry. Figure 4.3 illustrates average strain values in optical fiber embedded inside composite package for three geometries of the resin layers.

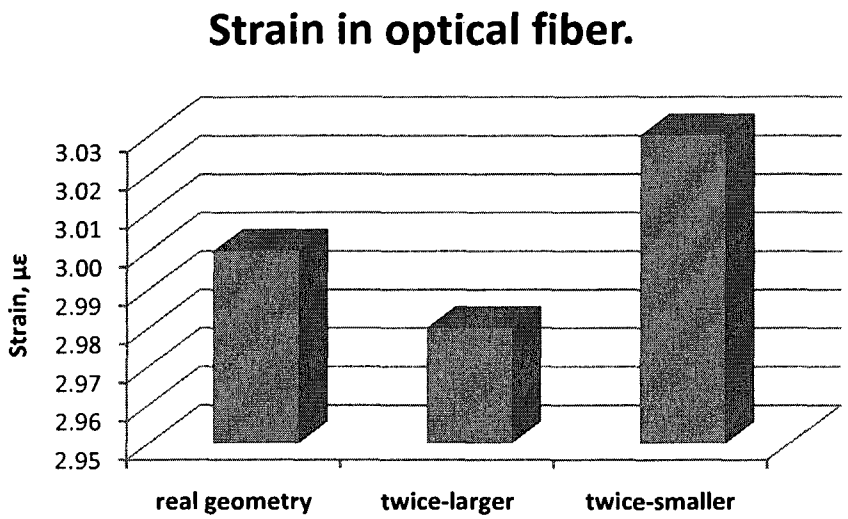

Figure 4.3. Strain in optical fiber transformed from composite package in ANSYS simulations for three geometries of the resin pocket.

From above results, enlarged size of resin pocket decreases the performance of the optical sensor embedded inside composite structure.

4.1.2 Simulations for three geometries of the resin pocket in composite carrier with added adhesive layer.

These simulations included three geometries of the resin pockets such as real resin pocket, twice smaller resin pocket, and twice larger resin pocket and adhesive layer (0.2 mm and 0.3 mm thickness). The strain in optical fiber embedded inside the composite structure was established. Strain is transmitted from adhesive layer to optical fiber through composite material of the package.

Suitably strong adhesive can be used to avoid distortion. According to J. W. Dally and W. F. Riley in their book [56] epoxy adhesives have higher bond strength and higher level of strain at failure than other types of adhesives; cyanoacrylate cement has fast cure at room temperature and its performance depends from time, moisture absorption, or elevated temperature (not for long usage); polyesters exhibit a high shear strength and modulus and can be applied at low temperature (5°C) but it has low peel strength a low resistance to solvents; ceramic cements can be used in radiation environment and in high temperature where organic adhesives cannot be applied. Material description of Permabond Cyanoacrylate adhesives 268 from ref. [57] was used for simulations. Thickness of the resin layer was chosen 0.2mm and 0.3 mm because thin bond layer of adhesive minimizes creep, hysteresis, and linearity problems from ref. [56]. For these two cases strain and ratio between applied strain and strain in optical fiber were recorded.

Three geometries of the resin pocket were used for simulations. Element type Solid92 was used as in previous simulations. Thin layer of resin was added to all geometries from previous ANSYS simulations. Nonsymmetrical model with 10^4 magnification was built in ANSYS, and simulations were performed. Displacement 30 (3mm) was applied on the layer1, adhesive layer, area at x=100 and zero displacement was applied on left side of the model at x,y-directions on all areas on the left side of the model and z-displacement on the back of the structure. The model with adhesive layer was used for different geometry of the resin pocket and two thicknesses of the adhesive layer. Figure 4.4 illustrates the cross-section and schematics of this model.

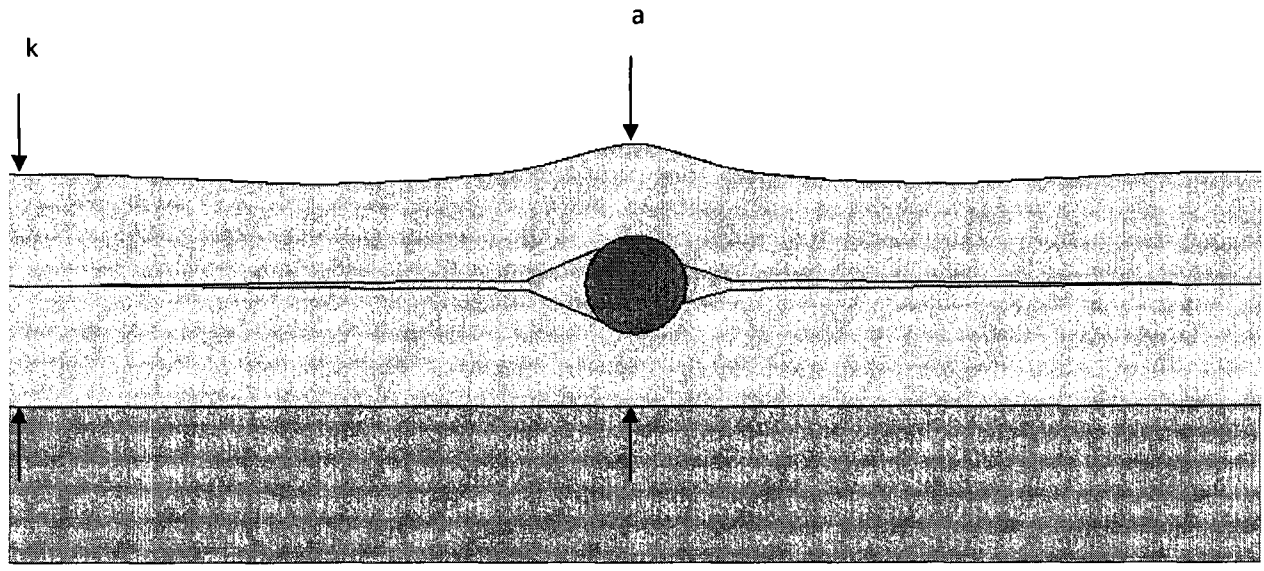

Adhesive layer

a

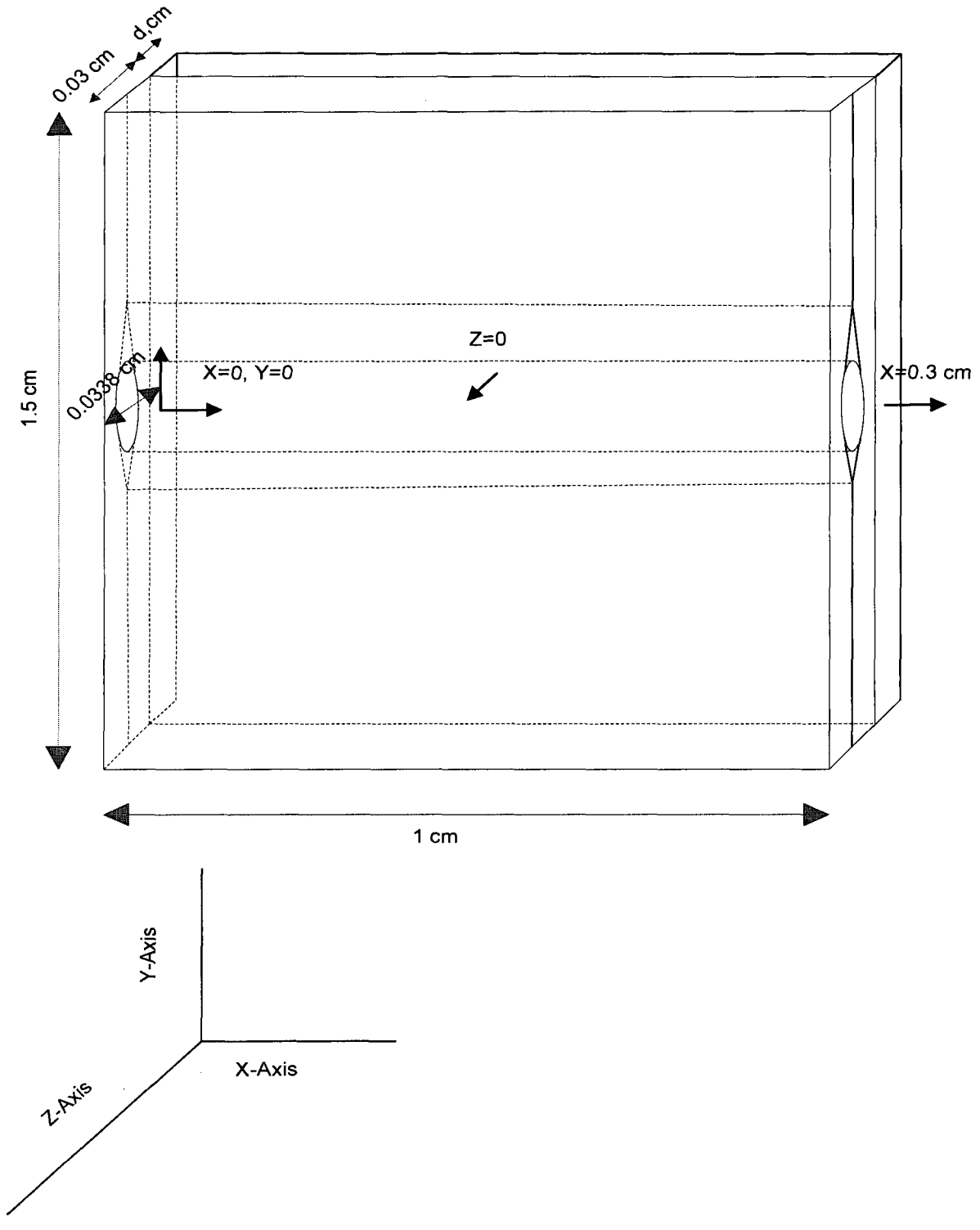

b

Figure 4.4. Model for ANSYS simulations a) cross-section and b) schematics.

Table 4.2 presents the thickness of the resin layer, d, and thickness of the composite packages for real geometry on the edge, k, /in the middle, a, which were used for creation of the models in ANSYS.

Table 4.2. Geometry of the adhesive layer and thicknesses of the composite package.

CYCOM®5276-1	d, m	k/a, m
[0/F(0)/0]	$0.2*10^{-3}$	$0.03*10^{-3}/0.0338*10^{-3}$
[0/F(0)/0]	$0.3*10^{-3}$	$0.03*10^{-3}/0.0338*10^{-3}$

Results of the simulations with adhesive layers.

The ratio of the strain in optical fiber versus strain in adhesive layer in geometries with different thicknesses of the adhesive layer is illustrated in Figure 4.5.

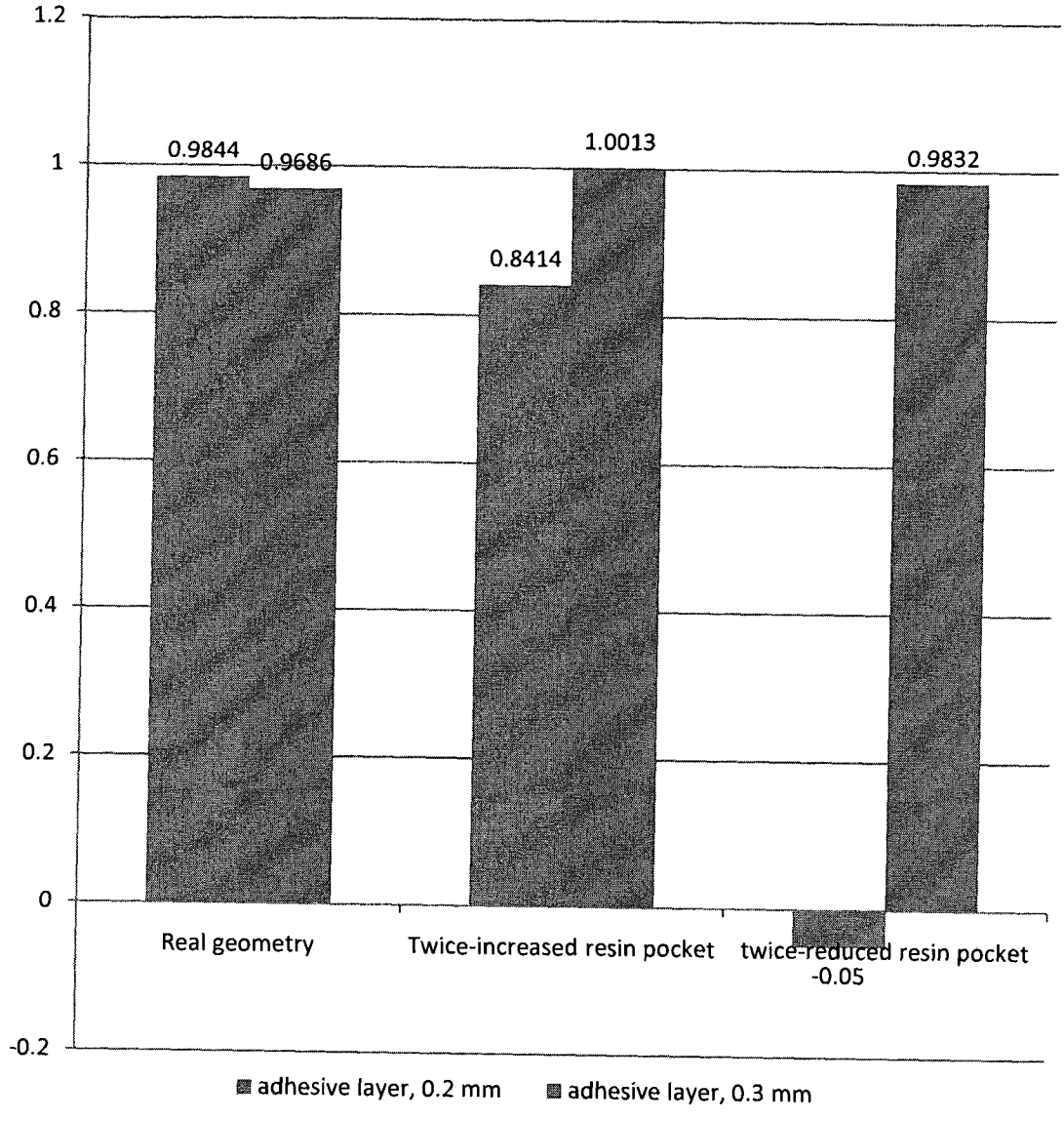

Figure 4.5. Strain ratio for different geometries and two adhesive layers.

The results showed that strain in optical fiber and adhesive layer in real geometry are almost the same for 0.2 mm and 0.3 mm adhesive layers. For adhesive layer with thickness 0.3 mm strain ratios of optical fiber and adhesive layer are almost 1 or almost the same in the middle of the structure. The negative strain ratio resulted due insufficient number of nodes for meshing of the model provided by software (16000). The increase in

number of data from meshing will provide with superior data. Figure 4.6 illustrates the values of the strain in optical fiber and adhesive layer for all geometries.

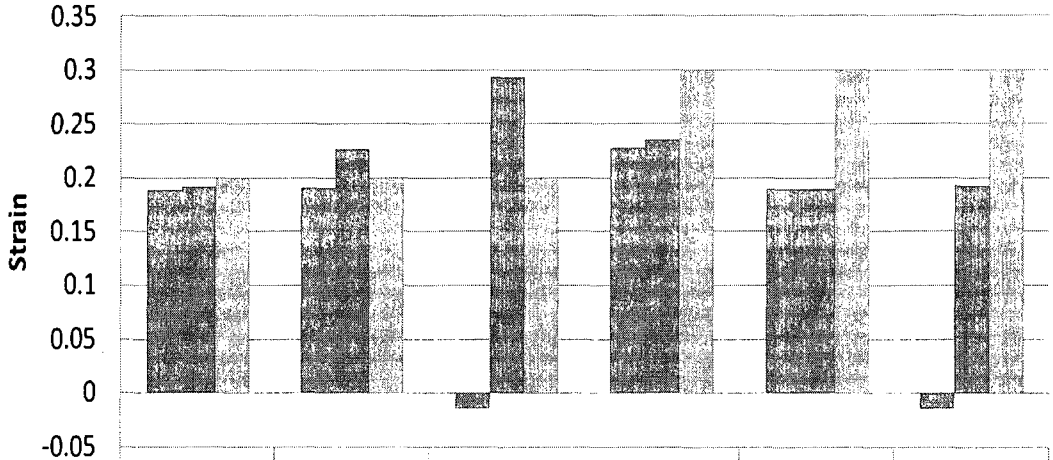

	Full size resin pocket	Double size resin pocket	Half size resin pocket	Full size resin pocket	Double size resin pocket	Half size resin pocket
Fiber	0.189	0.191	-0.0147	0.228	0.19025	-0.0147
Adhesive layer	0.192	0.227	0.294	0.2354	0.19	0.19325
adhesive layer, mm	0.2	0.2	0.2	0.3	0.3	0.3

Figure 4.6. Strain in x-direction for all geometries and adhesive layers.

Real geometry shows satifying results for adhesive layer 0.3 mm where differences between applied strain, 0.3mm/mm, and strain in fiber was 23% and in adhesive layer was 20%. The error between adhesive layer and optical fiber strains was 4%.

In summary, simulations using ANSYS software were done for three different geometries of the resin pocket and for adhesive layer 0.2 mm and 0.3 mm thicknesses. Solid92 element was used with magnification of the sample in 10^4 times. Zero displacement was applied in z-direction for back layer and in x,y- directions to the left of

the model on the adhesive layer. Displacement of 30 units was applied in positive x-direction on adhesive layer for 100 units length of the composite package in order to strech the fiber inside. Two paths inside optical fiber and inside adhesive layer were created and results of strain was obtained. The normalized strains were near 1 for geometries with adhesive layer 0.3 mm and strain within 4% difference between optical fiber and adhesive layer was for real geometry. In addition, real geometry which was implemented from microscopic results showed the maximum strain in optical fiber from the recorded data for both adhesive layer thicknesses. The real geometry with 0.3 mm adhesive layer introduced the best value of strain in optical fiber. The half smaller resin pocket did not illustrated good performance like for package without adhesive layer due to the apperance of the curvature in composite material. This mechanical behavior of the composite package wasconfirmed during tensile tests.

4.2 Simulations for composite packages used in tensile tests

Element Solid 92 was used for simulations in ANSYS. It consists of tetrahedral elements. Solid92 has a quadratic displacement behavior and is well suited to model irregular meshes which were applied for packaging. The tetrahedral element is defined by ten nodes having three degrees of freedom at each node: translations in the nodal x, y, and z directions. Adhesive layer, EPON 862/EPI-CURE 3234 was epoxy adhesive, CYCOM 5276-1 and NCT-301 were materials applied for packages, SMF from Corning was optical sensor, aluminum was test sample on which strain was applied and it was transmitted to composite carrier. Geometries for the models simulated in ANSYS were

done according to the microscopic observations. Resin pocket assumed symmetrical. As the result, half model was investigated. Figure 4.7 represents schematics of the model used for simulations in ANSYS for CYCOM®5276-1 and NCT301.

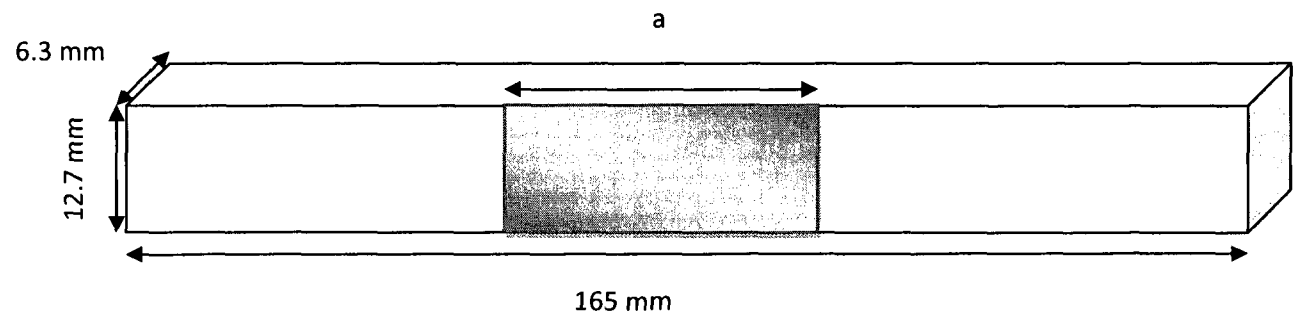

a

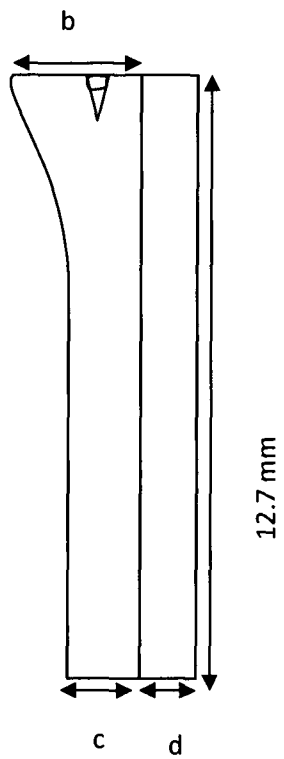

b

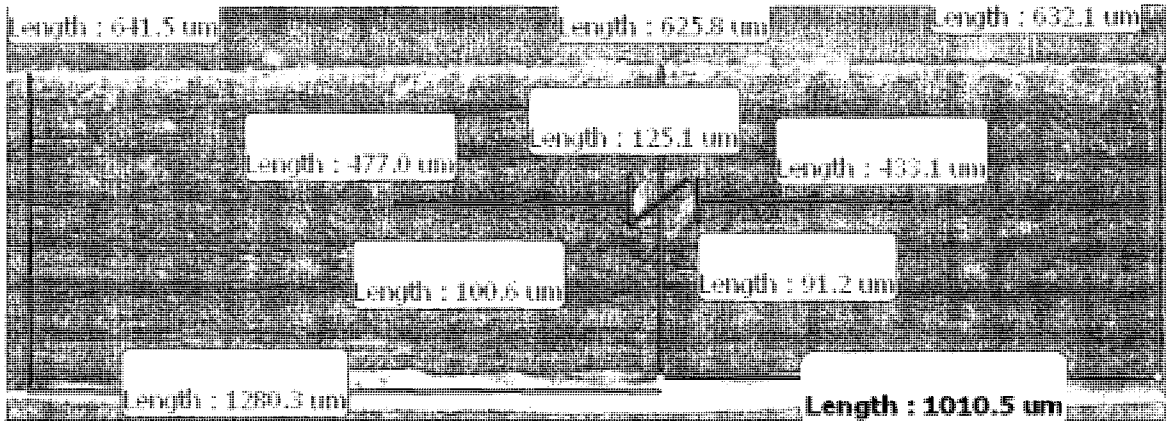

c

Figure 4.7. Schematics of the model used in ANSYS: a) aluminum with attached composite package; b) enlarged cross-section for shaded area includes adhesive layer, composite package, resin pocket, and optical fiber; c) geometry from microscopic results.

The geometry was different for composite package in CYCOM®5276-1 and NCT301 for [-60/60/F(0)/60/-60], [-45/45/F(0)/45/-45], and [90/90/F(0)/90/90] lay-ups. Table 4.3 represents the variations for a, b, c, and d parameters.

Table 4.3. Geometry variables for composite packages.

Composite material		a, mm	b, mm	c, mm	d, mm
CYCOM®5276-1, 250 μm thickness of adhesive layer	[90/90/F(0)/90/90]	55.6	0.69	0.59	0.25
	[-60/60/F(0)/60/-60]	55.6	0.71	0.67	0.25
CYCOM®5276-1, 100 μm thickness of adhesive layer	[90/90/F(0)/90/90]	59.79	0.63	0.62	0.1
	[-60/60/F(0)/60/-60]	51.1	0.66	0.61	0.1
NCT301, 100 μm thickness of adhesive layer	[90/90/F(0)/90/90]	51.5	0.56	0.5	0.1
	[-60/60/F(0)/60/-60]	50.7	0.59	0.55	0.1
	[-45/45/F(0)/45/-45]	50.8	0.59	0.52	0.1

The geometry of the resin pocket differed from one model to another. Figure 4.8 illustrates the resin pocket geometry.

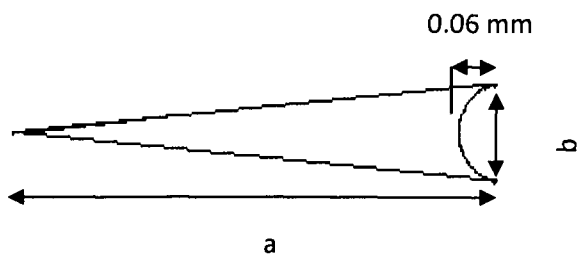

Figure 4.8. Geometry of the resin pocket.

The length of the resin pocket and width were different for composite carriers. Table 4.4 illustrates a and b values for resin pocket geometries.

Table 4.4. Geometries of the resin pockets.

Composite material		a, mm	b, mm
CYCOM®5276-1, 250 μm	[90/90/F(0)/90/90]	0.6	0.126
	[-60/60/F(0)/60/-60]	0.76	0.126
CYCOM®5276-1, 100 μm	[90/90/F(0)/90/90]	0.5	0.12
	[-60/60/F(0)/60/-60]	0.5	0.12
NCT301, 100 μm	[90/90/F(0)/90/90]	0.58	0.12
	[-60/60/F(0)/60/-60]	0.7	0.12
	[-45/45/F(0)/45/-45]	0.53	0.12

Meshing was applied on the created model. Maximum 256000 nodes for meshing was the restriction in ANSYS. Element size at picked areas was different for each volume in the model due to the geometry and restriction for maximum nodes allowed. Figure 4.9 illustrates the mesh of the model and magnified meshing on the edge of the composite carrier where mesh for optical fiber, resin pocket, composite package, and adhesive layer can be seen well.

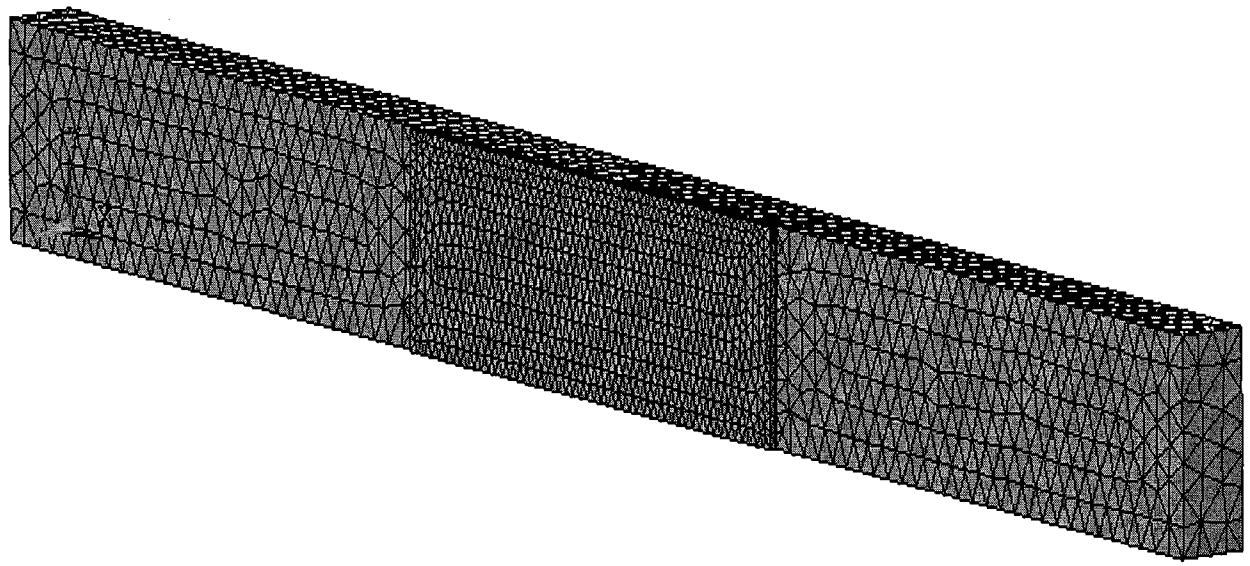

a

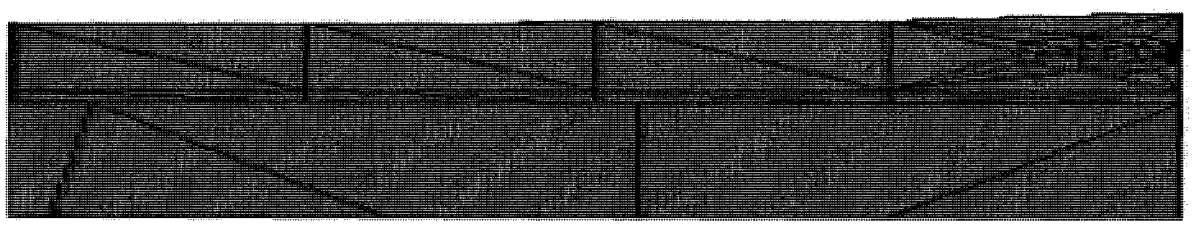

b

Figure 4.9. Meshing for a) all model; b) edge of the model.

The meshing was similar for all designs. Static analysis was used in simulations. Aluminum sample length was 165 mm, to generate strain 2000 με displacement for 0.33 mm was applied on right area of the aluminum. Boundary conditions: x and y displacements were zero for left area of the aluminum, z displacement was 0 for back area- opposite to one where composite carrier was applied, 0.33 displacement in x direction was applied on the right area of the aluminum, and zero displacement in y

direction was applied on the right area of aluminum. Figure 4.10 illustrates these boundary conditions.

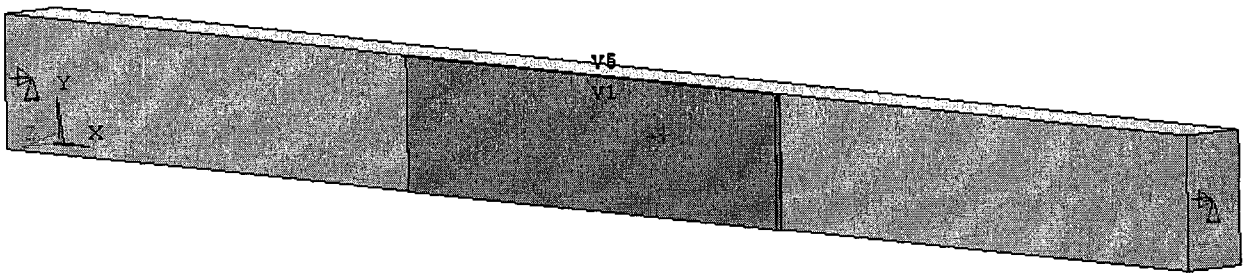

Figure 4.10. Boundary conditions for model in ANSYS.

The results of ANSYS simulations for average strain in x direction for composite packages fabricated from CYCOM 5276-1 and NCT 301 are illustrated in Figure 4.11.

Average strain in x direction for [90/90/F(0)/90/90] and [-60/60/F(0)/60/-60] designs, CYCOM 5276-1, thickness of adhesive layer 250 μm.

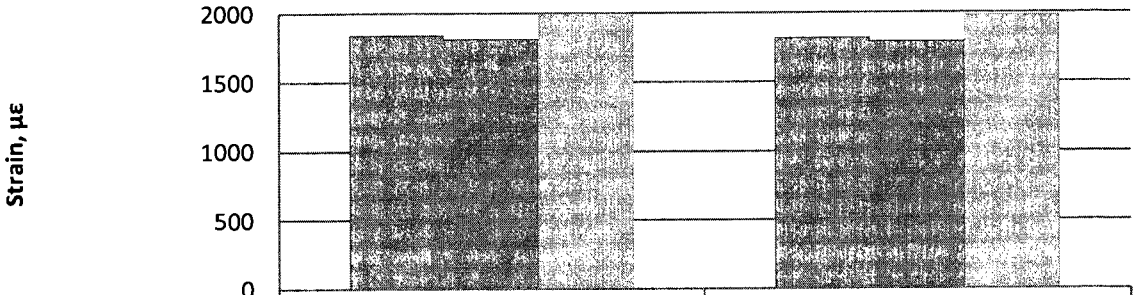

	[90/90/F(0)/90/90]	[-60/60/F(0)/60/-60]
optical fiber, με	1846	1820
composite carrier, με	1817	1794
aluminum, με	1988	1979

a

Average strain in x direction for [90/90/F(0)/90/90] and [-60/60/F(0)/60/-60] designs, CYCOM 5276-1, thickness of adhesive layer 100 μm.

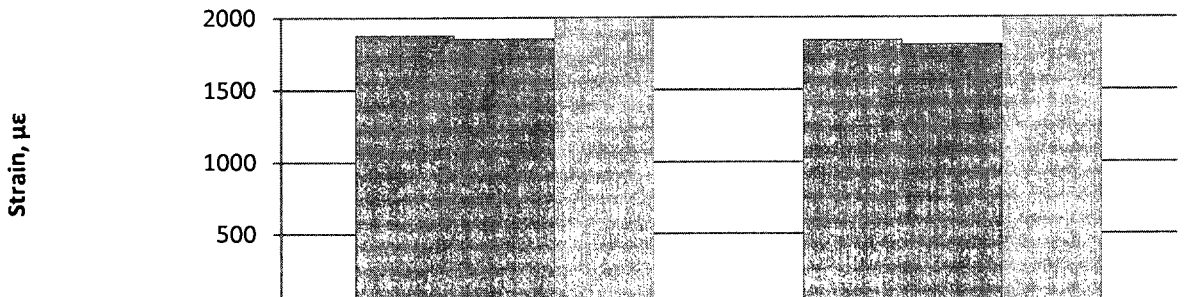

	[90/90/F(0)/90/90]	[-60/60/F(0)/60/-60]
optical fiber, με	1882	1846
composite carrier, με	1856	1813
aluminum, με	1988	1989

b

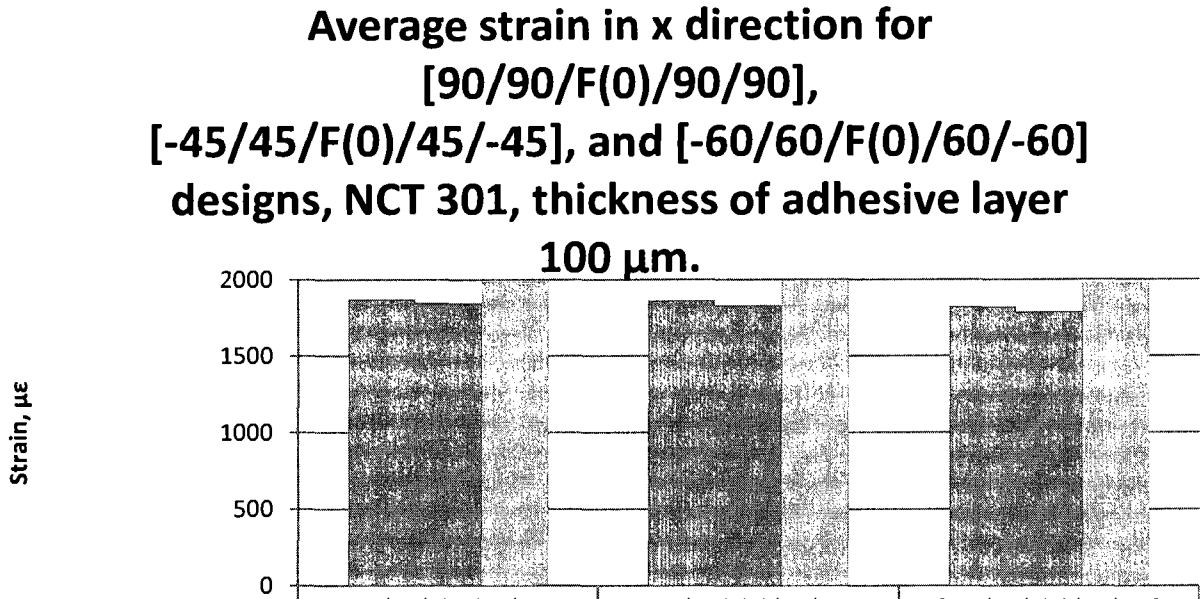

c

Figure 4.11. Average strain in x direction in aluminum, in optical fiber, and on the composite carrier for a) CYCOM 5276-1, thickness of adhesive layer 250 μm, [90/90/F(0)/90/90] and [-60/60/F(0)/60/-60] designs of composite carrier; b) CYCOM 5276-1, thickness of adhesive layer 100 μm, [90/90/F(0)/90/90] and [-60/60/F(0)/60/-60] designs; c) NCT 301, thickness of adhesive layer 100 μm, [90/90/F(0)/90/90], [-60/60/F(0)/60/-60], and [-45/45/F(0)/45/-45] designs.

Figure 4.12 represents the strain in x direction and standard deviation for different lay-ups of the composite carrier.

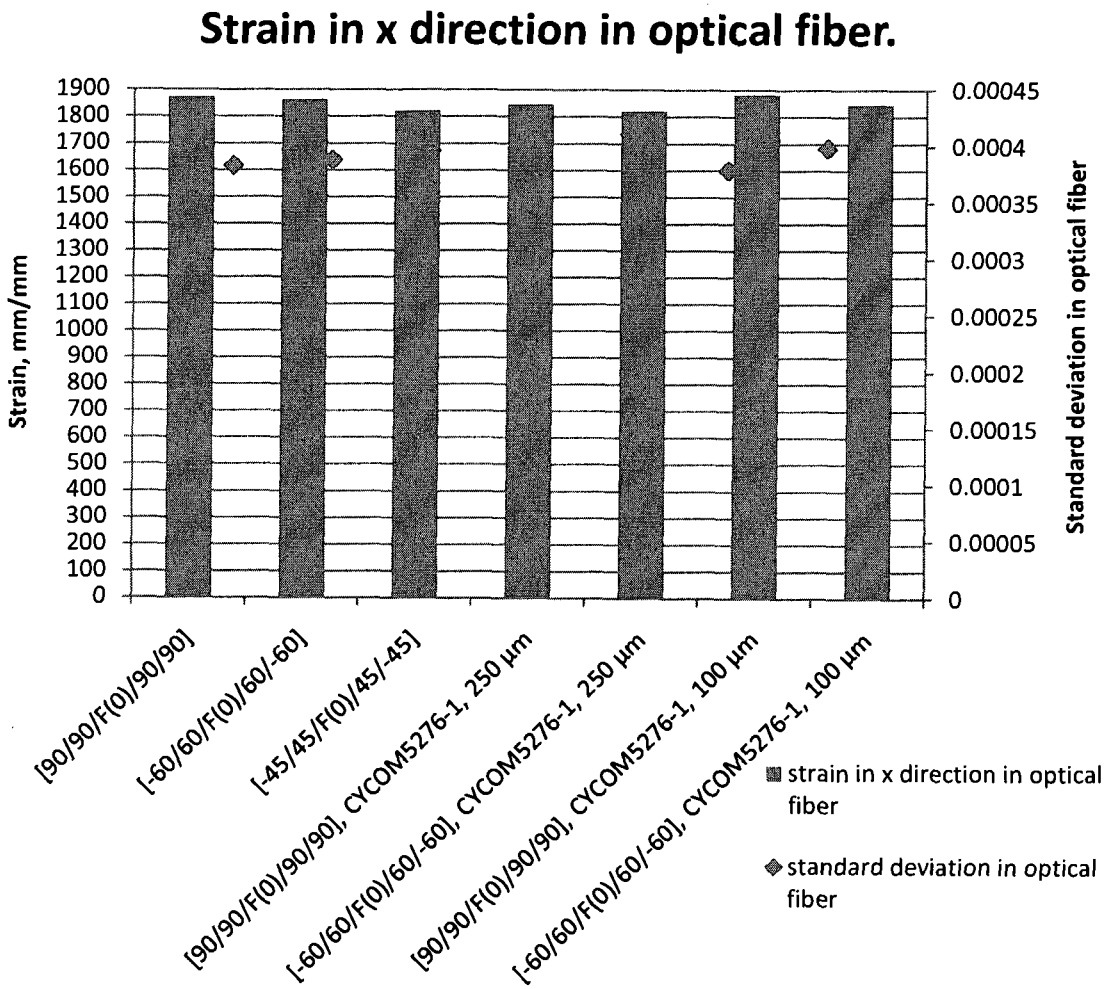
Strain in x direction in optical fiber.
Strain, mm/mm
Standard deviation in optical fiber
1900
1800
1700
1600
1500
1400
1300
1200
1100
1000
900
800
700
600
500
400
300
200
100
0
0.00045
0.0004
0.00035
0.0003
0.00025
0.0002
0.00015
0.0001
0.00005
0
[90/90/F(0)/90/90]
[-60/60/F(0)/60/-60]
[-45/45/F(0)/45/-45]
[90/90/F(0)/90/90], CYCOM5276-1, 250 µm
[-60/60/F(0)/60/-60], CYCOM5276-1, 250 µm
[90/90/F(0)/90/90], CYCOM5276-1, 100 µm
[-60/60/F(0)/60/-60], CYCOM5276-1, 100 µm
strain in x direction in optical fiber
standard deviation in optical fiber

a

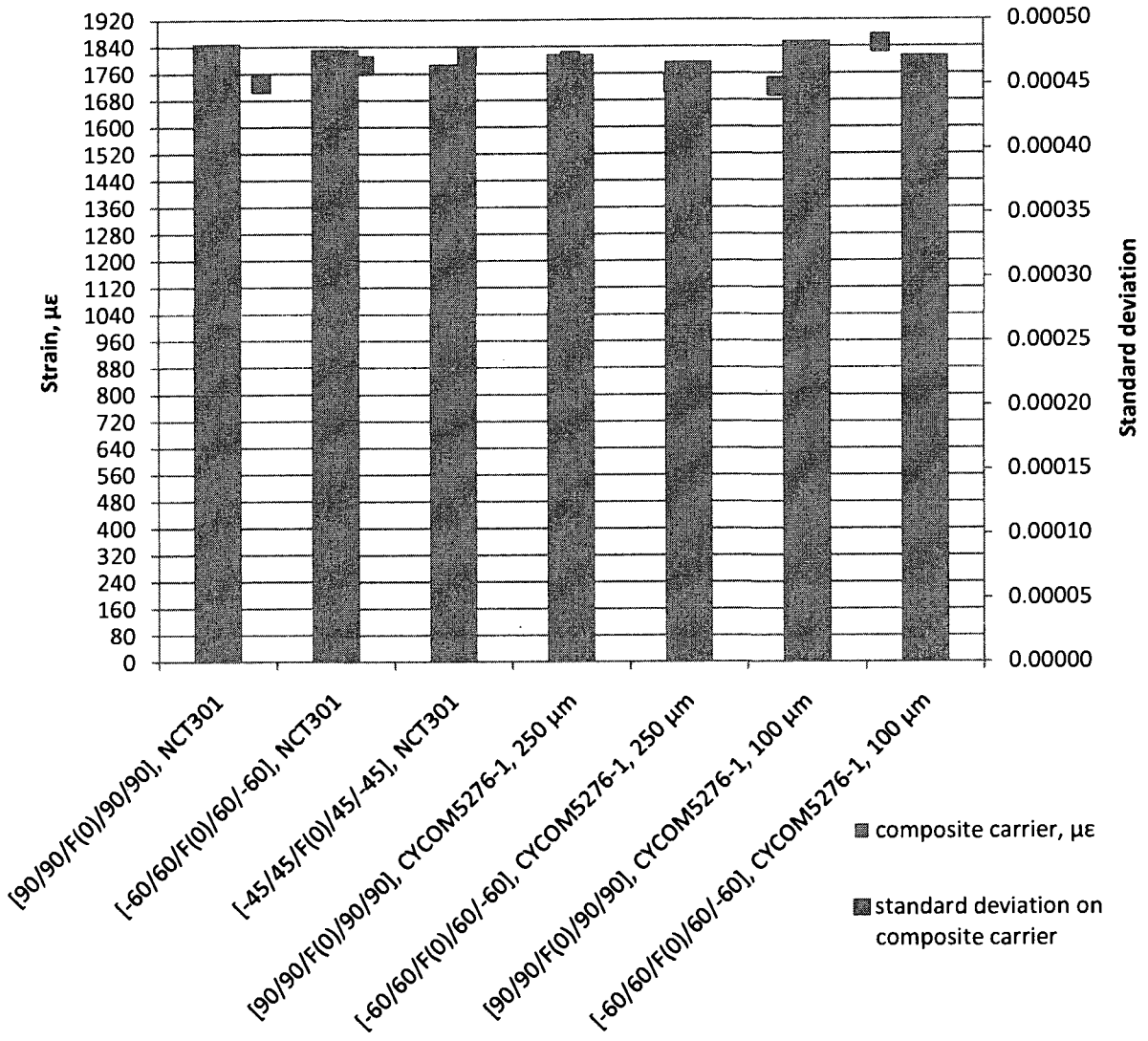
Average strain in x direction on composite carrier.
Strain, με
Standard deviation
1920
1840
1760
1680
1600
1520
1440
1360
1280
1200
1120
1040
960
880
800
720
640
560
480
400
320
240
160
80
0
0.00050
0.00045
0.00040
0.00035
0.00030
0.00025
0.00020
0.00015
0.00010
0.00005
0.00000
[90/90/F(0)/90/90], NCT301
[-60/60/F(0)/60/-60], NCT301
[-45/45/F(0)/45/-45], NCT301
[90/90/F(0)/90/90], CYCOM5276-1, 250 μm
[-60/60/F(0)/60/-60], CYCOM5276-1, 250 μm
[90/90/F(0)/90/90], CYCOM5276-1, 100 μm
[-60/60/F(0)/60/-60], CYCOM5276-1, 100 μm
composite carrier, με
standard deviation on composite carrier

b

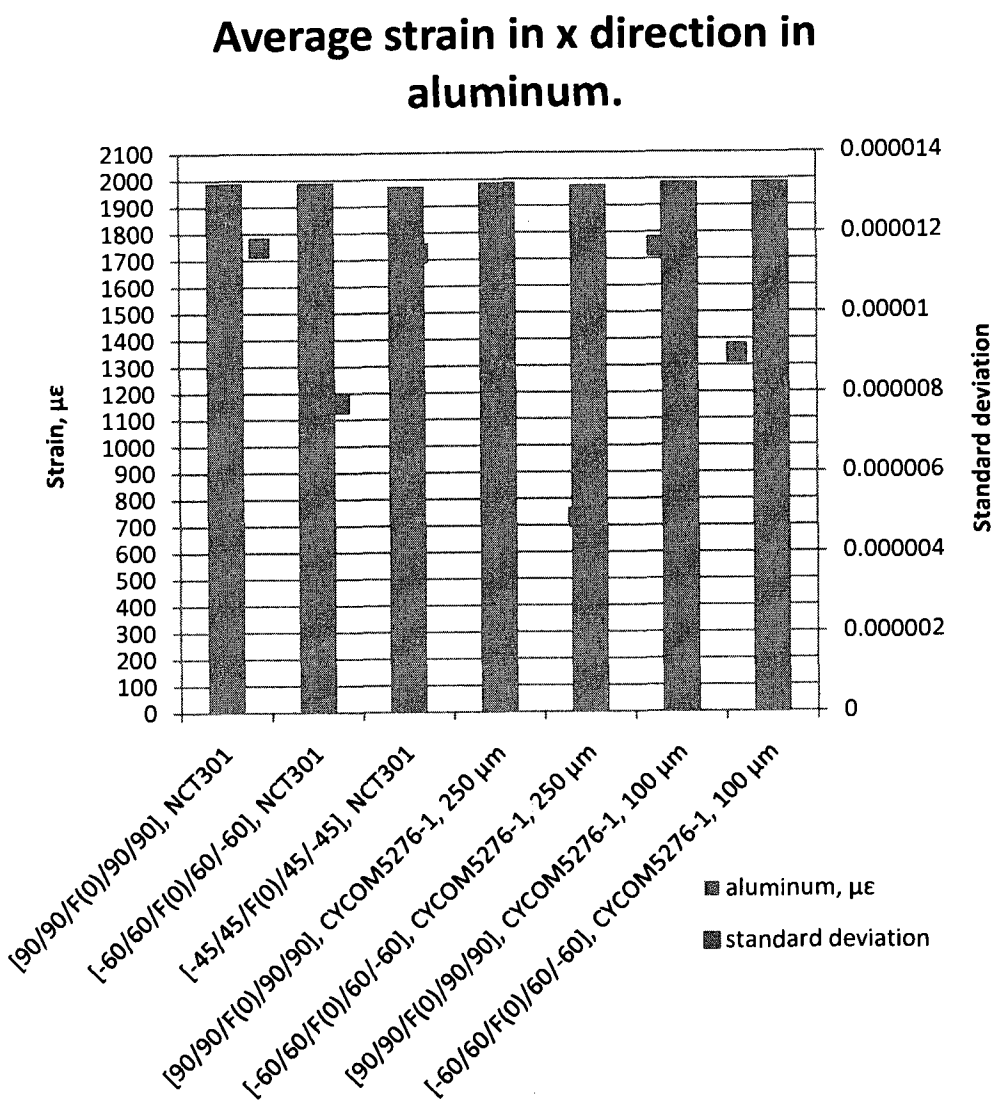

c

Figure 4.12. Average strain in x direction for CYCOM5276-1 and NCT 301 and [90/90/F(0)/90/90], [-60/60/F(0)/60/-60], and [-45/45/F(0)/45/-45] designs with deviation a) in optical fiber; b) on composite carrier; c) in aluminum.

The illustrated results showed that average strain in x direction in optical fiber almost the

same for [90/90/F(0)/90/90] and [-60/60/F(0)/60/-60] designs with NCT301 composite material and comparable with [90/90/F(0)/90/90] design using CYCOM5276-1. CYCOM5276-1 is stiffer than NCT301; therefore, [-60/60/F(0)/60/-60] design did not illustrate the same value of the strain it was slightly less. The values of the strain for composite carrier are less than strain readings in optical fiber and aluminum. The average strain in optical fiber was between values of the strain on aluminum and strain on composite package.

In summary, package [90/90/F(0)/90/90] illustrated the best performance in strain transmission from the aluminum. However, [-60/60/F(0)/60/-60] design has improved strain values for NCT 301 composite material and can be preferable for practical applications because of the fragility of the [90/90/F(0)/90/90] design in x direction. The average strain results will be compared with the results from tensile tests in the following Chapter 5.

CHAPTER 5.

RESULTS AND DISCUSSION

Optical sensors embedded in graphite/epoxy were studied in this work. The research for appropriate composite carrier with embedded optical sensor was investigated. Four different lay-ups were tested. The experimental results were evaluated and optimizations were made. The static tensile tests were repeated with successful composite package designs, different composite materials, and different adhesive materials.

The results revealed that packaged sensors with [90/90/F(0)/90/90] and [-60/60/F(0)/60/-60] lay-ups demonstrated higher transmission of the strain from the mechanical material to the composite carrier. Static tests for maximum 2000 με were repeated 3 times for each packaged optical sensor in case of CYCOM®5276-1 material and 6 times repeated in case of NCT301 material. Maximum axial force of 21 kN was applied on aluminum samples on which composite carriers were adjusted using EPON 824/EPI-CURE 3432. The thicknesses of adhesive layer 250 μm and 100 μm were applied to adjust the composite carriers fabricated from CYCOM®5276-1 material, and thickness of adhesive layers100 μm was used in case of fabricated composite packages from NCT301 composite material. Thin adhesive layer improved transmission of the strain into composite package. The results of the simulations for created models in ANSYS and results from static tensile tests were compared in order to obtain performance of the new optical package.

The greater uncertainty in the embedded sensitivity was attributed to unknown exact gauge length of the embedded sensor and appearance of kinks on the mirror surface and optical fiber. In addition, the composite package design and material on which composite carrier will be applied as well as the most suitable adhesive and its thickness were the factors for alteration in strain values from Michelson interferometer as this was discussed in this thesis.

5.1 Strain Measurements

5.1.1 Error calculations in Michelson interferometer embedded in composite package.

The error calculation is based on the formula (32) described in Chapter 2. The Table 5.1 illustrates the error results for phase shift in Michelson interferometer for fabricated and tested composite carriers.

Table 5.1. Error results in phase shift for composite carriers.

Composite material		Theoretical phase shift, $\delta=\Delta\varphi$	Practical phase shift, $\delta'=\Delta\varphi_{pr}$	Error, 100%* $\frac{\delta-\delta'}{\delta'}$,%
CYCOM®5276-1, 250 μm	[90/90/F(0)/90/90]	789.6	726.5876	8.67
	[-60/60/F(0)/60/-60]	768.9226	728.0909	5.6
CYCOM®5276-1, 100 μm	[90/90/F(0)/90/90]	758.2572	696	8.9
	[-60/60/F(0)/60/-60]	776.184	703.8521	10.28
NCT301, 100 μm	[90/90/F(0)/90/90]	842.9214	786.2849	7.2
	[-60/60/F(0)/60/-60]	796.3288	796.1686	0.02
	[-45/45/F(0)/45/-45]	856.601	117.4615	629.26

The results showed that error in phase shift based on strain from aluminum is small or almost zero for NCT301 composite material in composite carriers with [-60/60/F(0)/60/-60] and [90/90/F(0)/90/90] lay-ups. Composite material with less stiffness and lay-up designs [90/90/F(0)/90/90] and [-60/60/F(0)/60/-60] are appropriate composite carriers for mechanical structure with the stiffness similar to the aluminum. Large error in [-45/45/F(0)/45/-45] composite package from NCT301 material due to the large difference in phase shift between theoretical and practical values. This happened due to the stiff package. Optical sensor embedded inside composite carrier was not strained to 2000 με.

5.1.2 Comparing experimental and simulations results for strain measurements.

The results of the average strain from tensile tests in optical fiber, on composite package, and on aluminum sample were compared with the results from ANSYS simulations. Figure 5.1 illustrates these data.

Average strain results from tensile tests and ANSYS simulations for [90/90/F(0)/90/90].

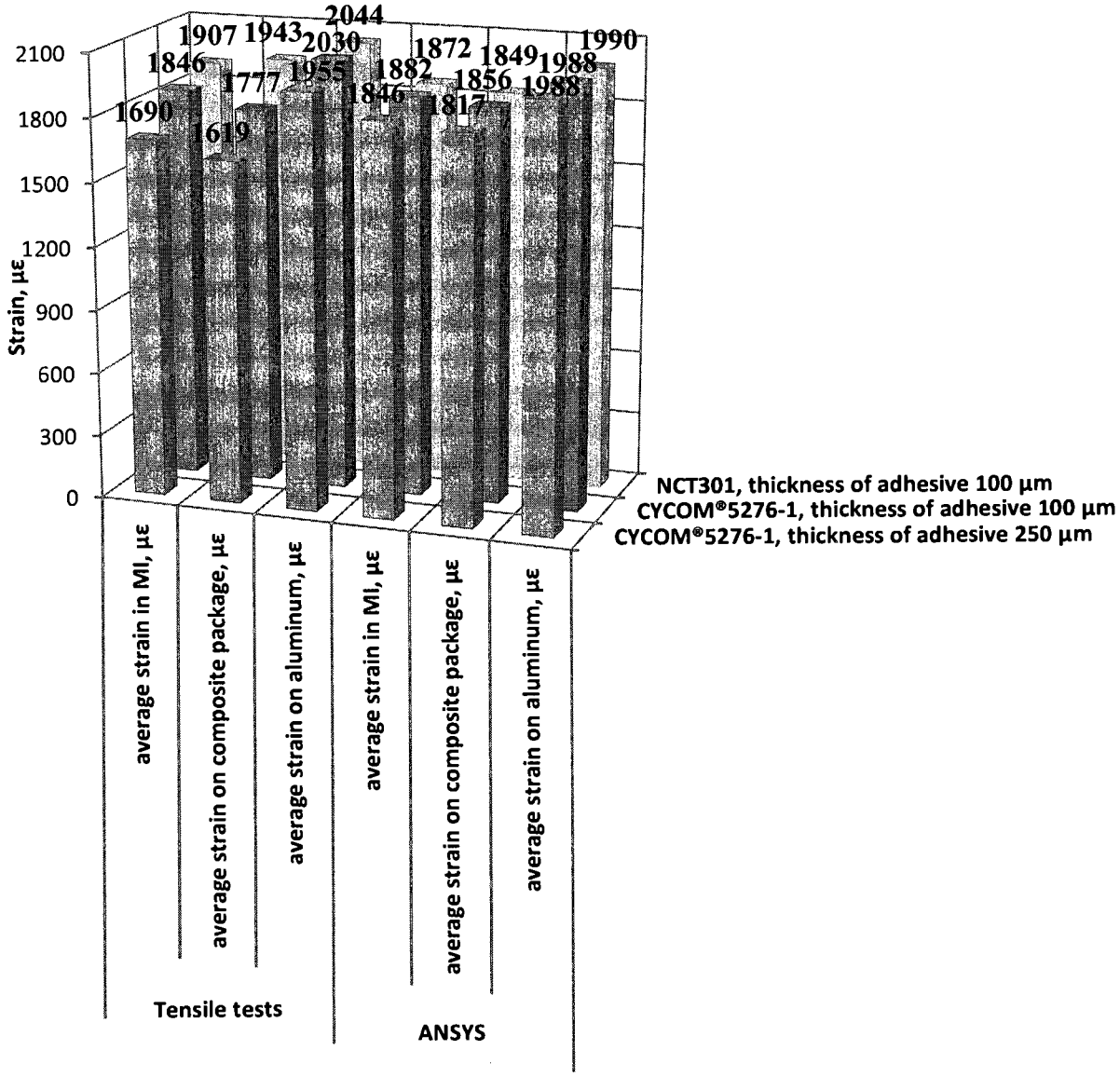

a

Average strain results from tensile tests and ANSYS simulations for [-60/60/F(0)/60/-60].

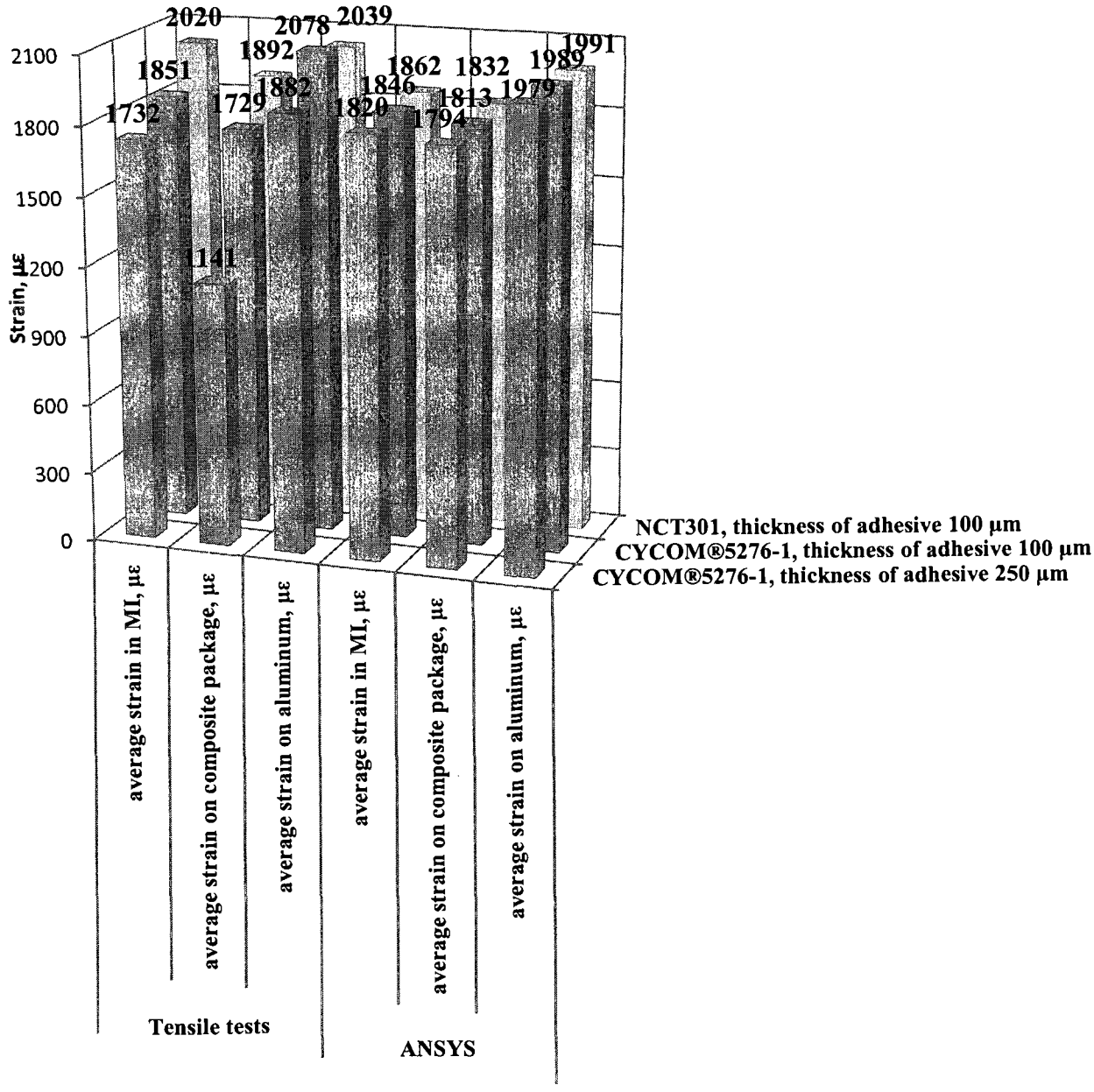

b

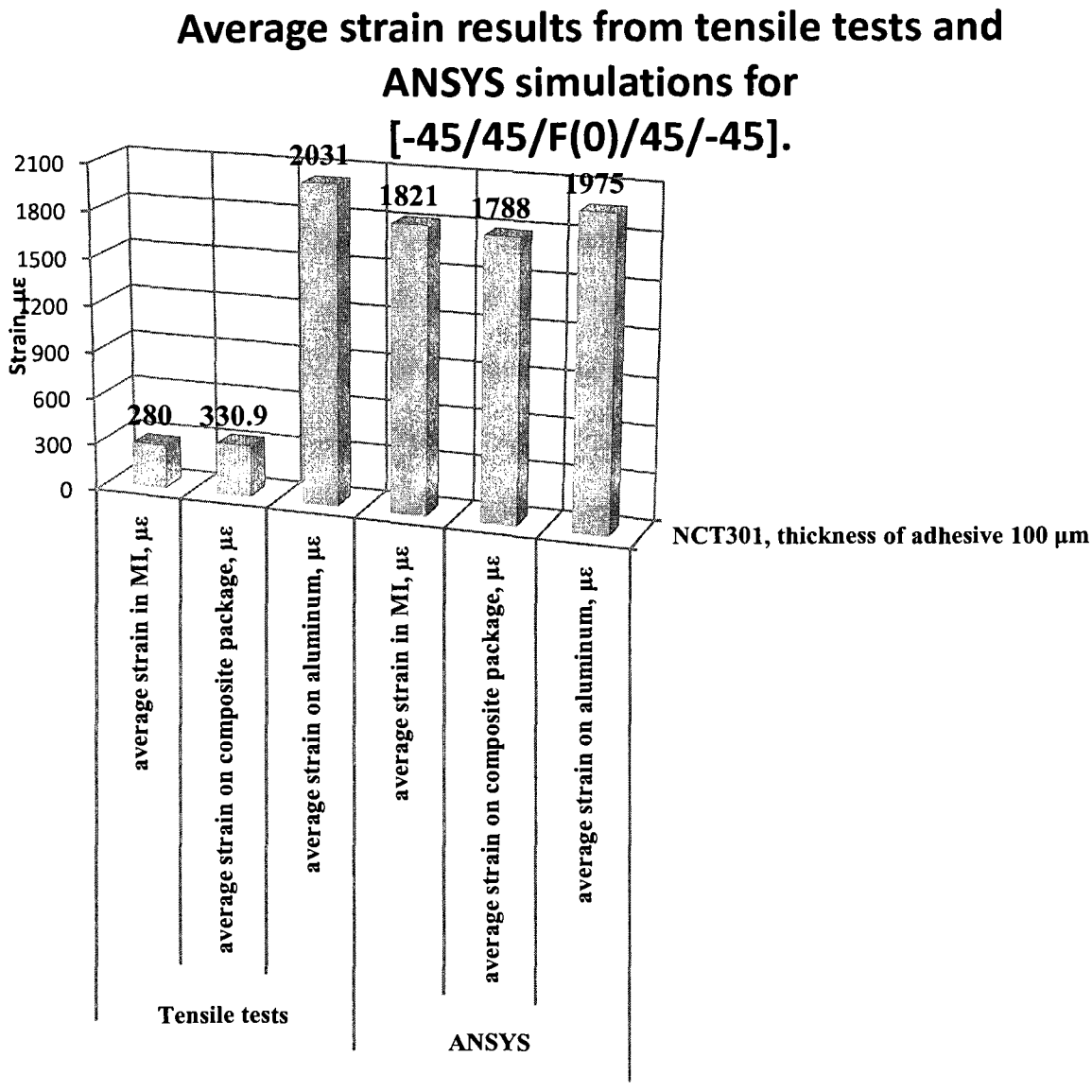

c

Figure 5.1. Average strain data from tensile tests and ANSYS simulations for a) composite package [90/90/F(0)/90/90], b) composite package [-60/60/F(0)/60/-60], c) composite package [-45/45/F(0)/45/-45].

The results show that the differences between simulation outputs and tensile tests for measuring strain exist. In case of [90/90/F(0)/90/90] and [-60/60/F(0)/60/-60] composite packages strain on composite carrier from tensile tests was smaller than simulated results for CYCOM®5276-1,and the same strain was larger for NCT301 composite material. In case of [-45/45/F(0)/45/-45] composite package strain on composite carrier from tensile tests was smaller than simulated results for NCT301.

The differences between simulations and tensile tests were due to the fact that average values were used for comparison. The edges of the composite carriers as it was observed in ANSYS simulations tend to bend due to the applied strain in adhesive layer. This feature gives decreased average value for strain on the composite package. Indeed, NCT301 was the match for aluminum due to smaller Young's modulus in axial direction. Figure 5.2 illustrates the strain calibration between aluminum, composite package, and Michelson interferometer, MI, in CYCOM®5276-1.

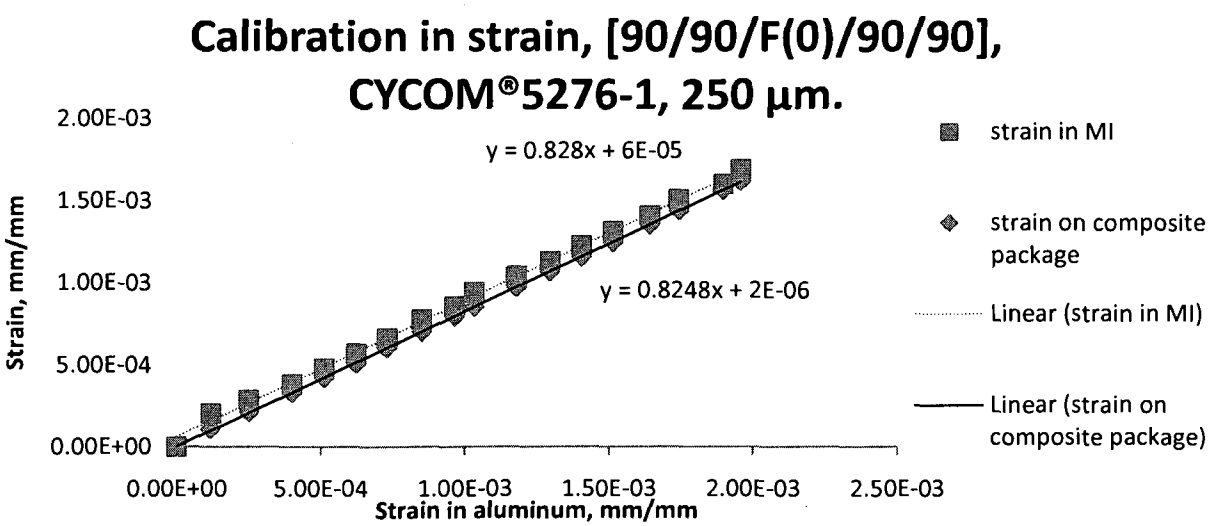

a

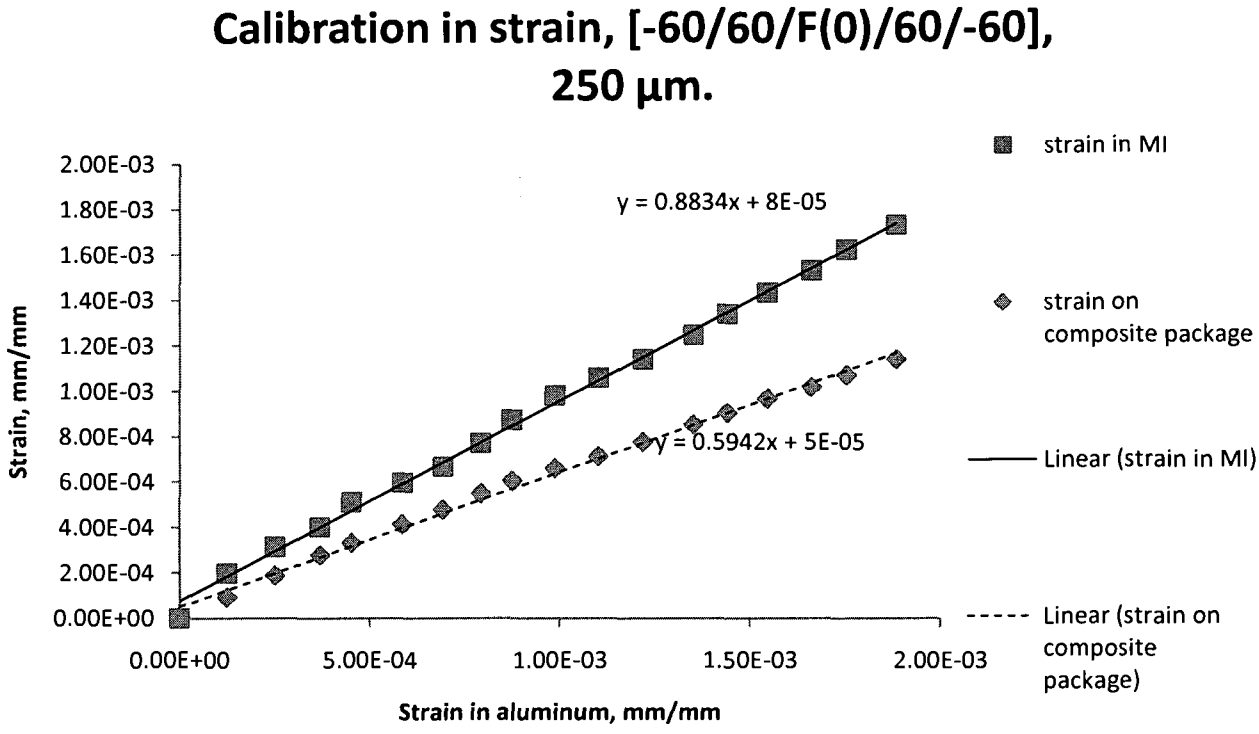
Calibration in strain, [-60/60/F(0)/60/-60], 250 µm.
y = 0.8834x + 8E-05
y = 0.5942x + 5E-05
Strain, mm/mm
Strain in aluminum, mm/mm
2.00E-03
1.80E-03
1.60E-03
1.40E-03
1.20E-03
1.00E-03
8.00E-04
6.00E-04
4.00E-04
2.00E-04
0.00E+00
0.00E+00
5.00E-04
1.00E-03
1.50E-03
2.00E-03
strain in MI
strain on composite package
Linear (strain in MI)
Linear (strain on composite package)

b

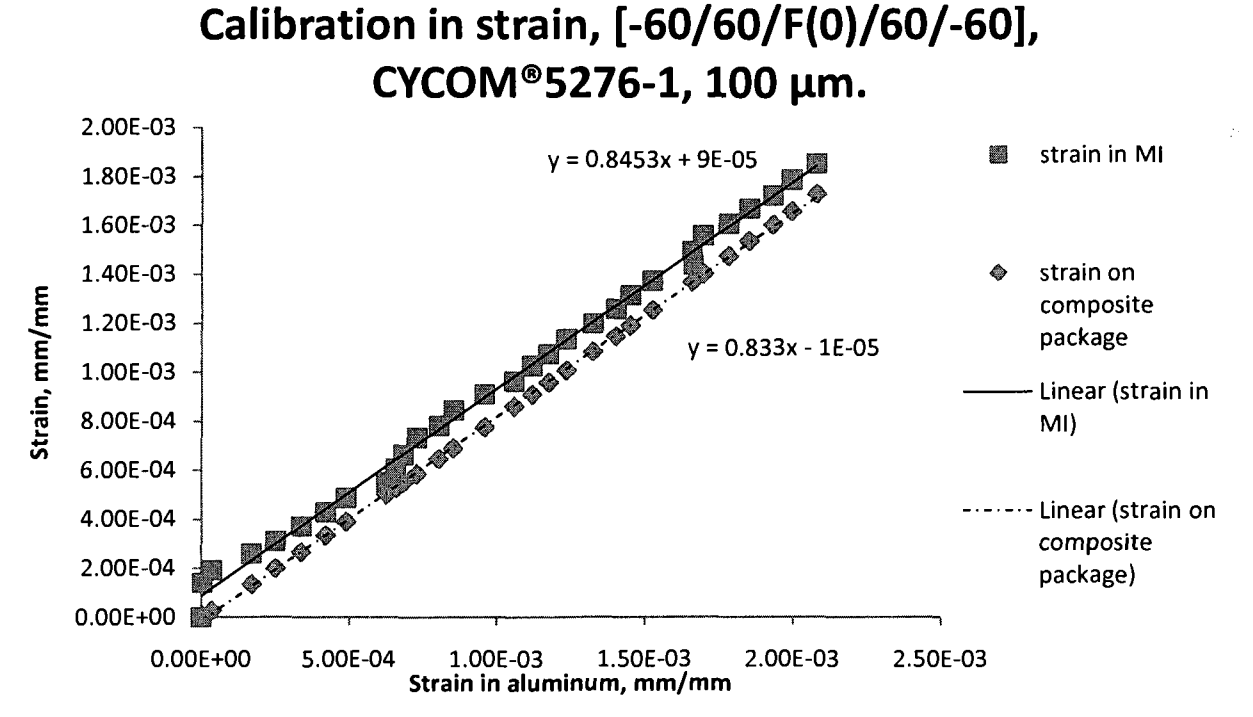
Calibration in strain, [-60/60/F(0)/60/-60], CYCOM®5276-1, 100 µm.
y = 0.8453x + 9E-05
y = 0.833x - 1E-05
Strain, mm/mm
Strain in aluminum, mm/mm
2.00E-03
1.80E-03
1.60E-03
1.40E-03
1.20E-03
1.00E-03
8.00E-04
6.00E-04
4.00E-04
2.00E-04
0.00E+00
0.00E+00
5.00E-04
1.00E-03
1.50E-03
2.00E-03
2.50E-03
strain in MI
strain on composite package
Linear (strain in MI)
Linear (strain on composite package)

c

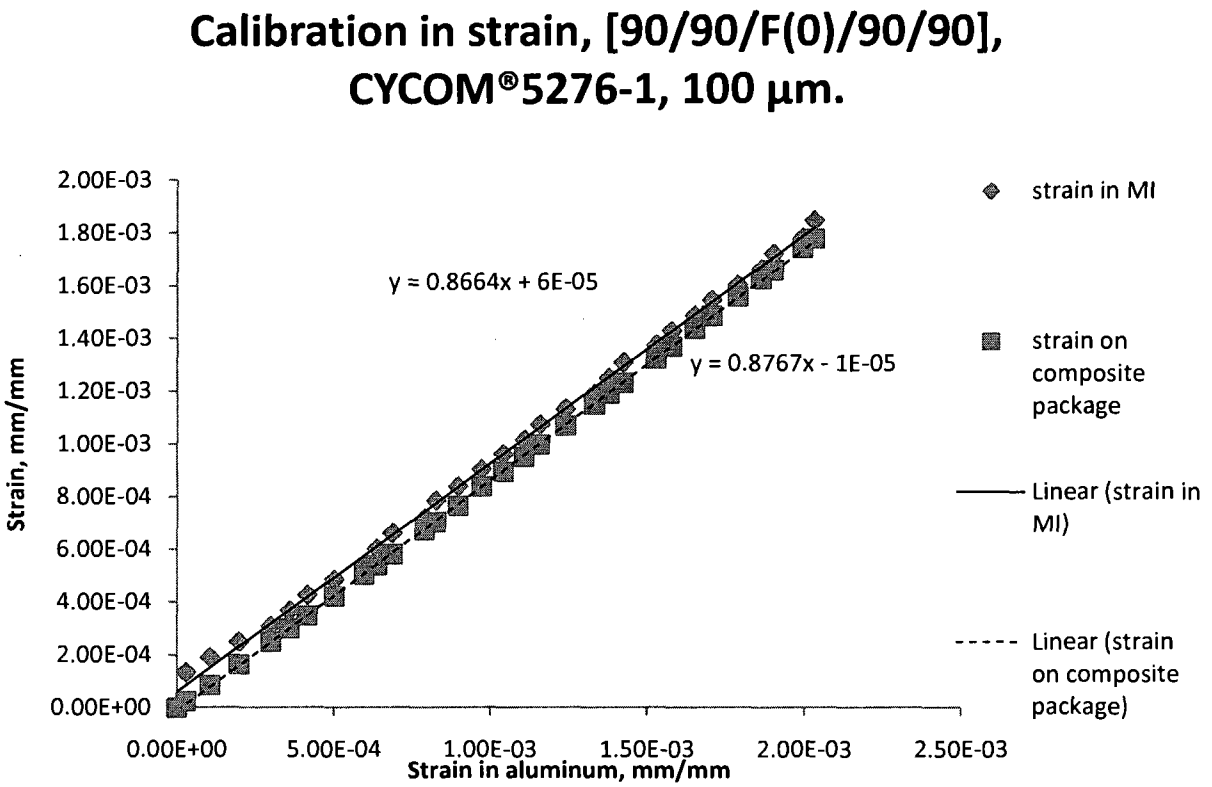

d

Figure 5.2. Calibration between strain in aluminum and in MI in CYCOM®5276-1 for a) [90/90/F(0)/90/90] design and b) [-60/60/F(0)/60/-60] design for adhesive layer 250 µm, and c) [-60/60/F(0)/60/-60] design, and d)[90/90/F(0)/90/90] design for adhesive layer 100 µm.

From the results of the calibration the slope which is close to one is for [-60/60/F(0)/60/-60] design with adhesive layer 250 µm and [90/90/F(0)/90/90] design with adhesive layer 100 µm.

Figure 5.3 illustrates calibration between strain in aluminum and in MI for composite packages from NCT301.

Calibration in strain, [-60/60/F(0)/60/-60], NCT301, 100 µm.

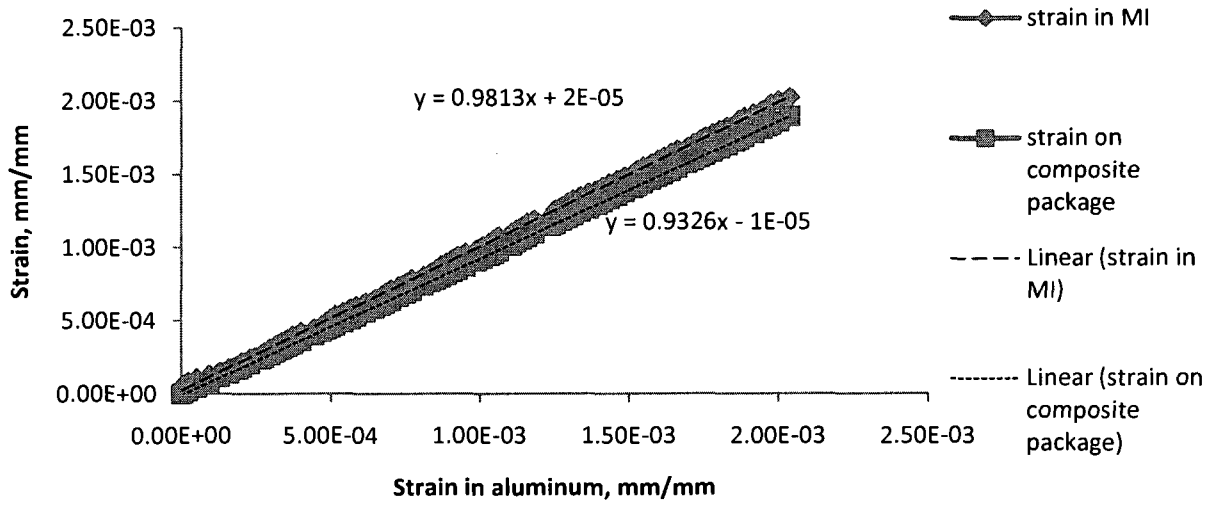

a

Calibration in strain, [-45/45/F(0)/45/-45], NCT301, 100 µm.

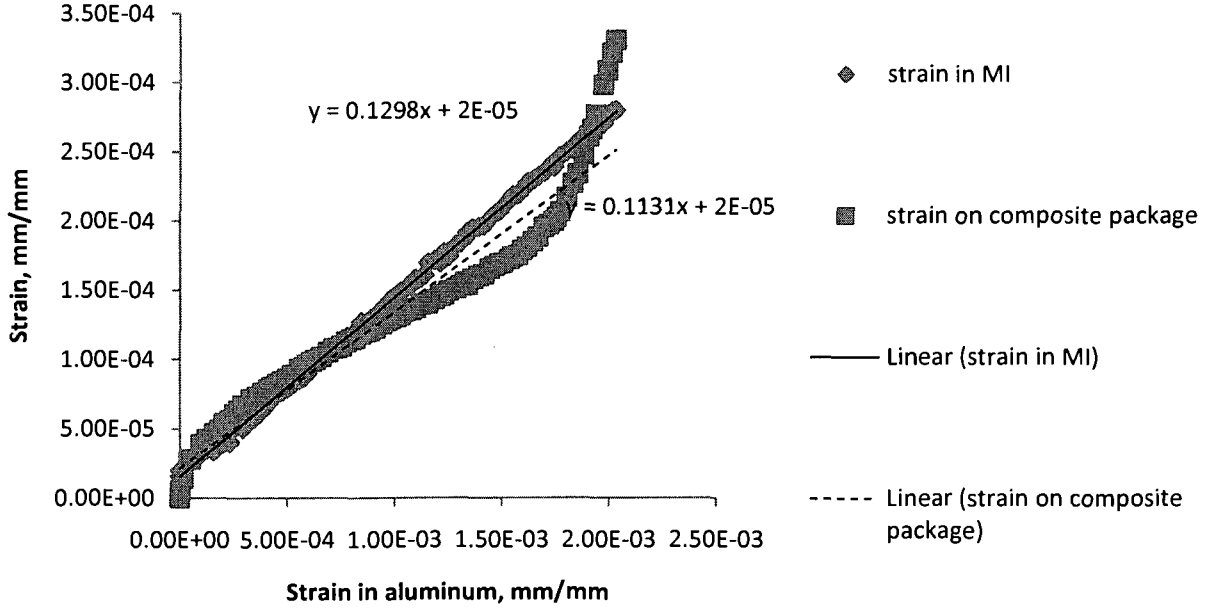

b

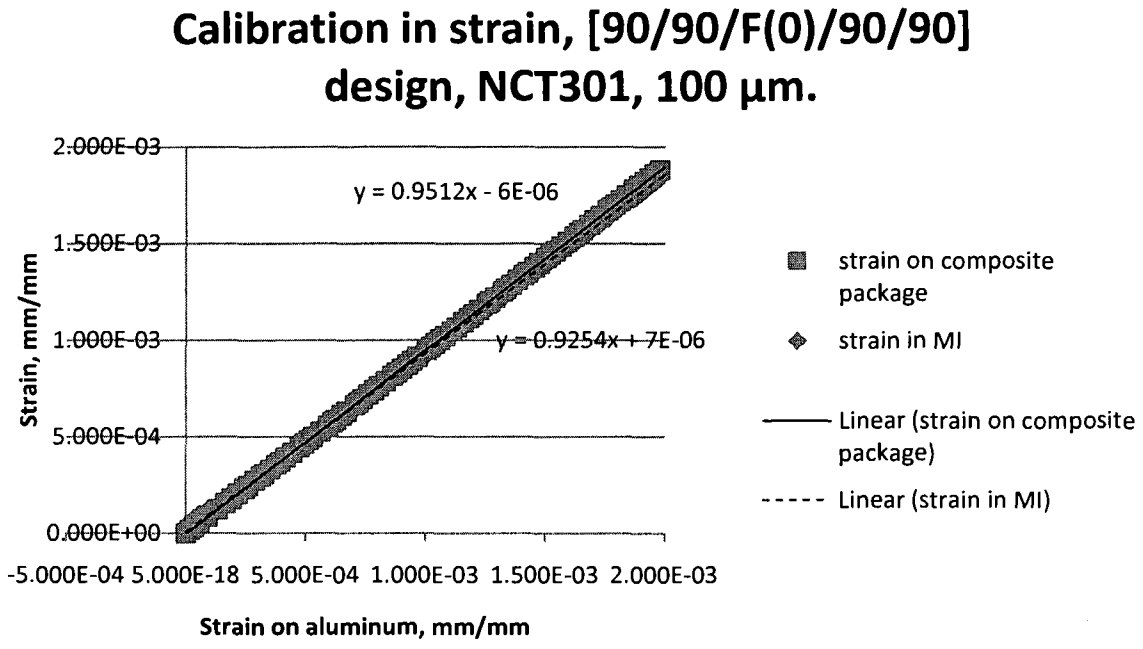

c

Figure 5.3. Calibration between strain in aluminum and in MI in NCT301 for a) [-60/60/F(0)/60/-60] design, b) [-45/45/F(0)/45/-45] design, and c) [90/90/F(0)/90/90] design for adhesive layer 100 µm.

Calibration results for composite packages fabricated from NCT301 material illustrated slope closer to 1 than the packages from CYCOM®5276-1 composite material. Indeed, the values of the slopes are 0.93 and 0.98 for [90/90/F(0)/90/90] and [-60/60/F(0)/60/-60] designs respectively. Consequently, these packages had nearly the same strain as aluminum sample, and optical sensor embedded inside composite package had strain values almost like aluminum. Designed packages with 0.9 calibration slope can be implemented on the aluminum structures where value of the strain can be calculated based on calibration results.

5.2 Discussion

The goal of this work was to study on an optimal composite package design which will protect optical fiber from environmental hazard, be applicable for different mechanical structures with high and low stiffness, and can be applied on different geometrical structures. The results of this work showed that for mechanical structures like aluminum NCT301composite packages with laminate designs [90/90/F(0)/90/90] and [-60/60/F(0)/60/-60] will be appropriate ones. The geometry of this package design illustrates the capability of the composite carrier to be applied on any geometry where flat area 5cm by 3 cm available. The composite package [90/90/F(0)/90/90] exhibits fragility in axial direction; therefore, laminate design [-60/60/F(0)/60/-60] is preferable, this design provides stiffness to the bending. The calibrations between strain in aluminum and strain in Michelson interferometer illustrated that slope close to one in [-60/60/F(0)/60/-60] and [90/90/F(0)/90/90] designs of the composite packages. The drop of the sensitivity between of the fiber and composite package can be due delamination inside the package resin layers between the layers in composite laminate, and high stiffness of the composite package. If package has high Young's modulus along the applied force it will reinforce the weak mechanical structure through adhesive layer. The thickness of the adhesive layer will cause to the differences in strain in aluminum substrate and in composite package. Thin layer illustrated better transmission of the strain from aluminum to the composite package.

CHAPTER 6

SUMMARY AND FUTURE WORKS

The objective of this thesis was to develop and characterize the composite carrier with embedded optical sensor for mechanical applications.

Fabrication and static tensile tests were performed for evaluation of the optical sensor embedded inside composite package. Initially four lay-up designs were proposed such as [90/90/F(0)/90/90], [-60/60/F(0)/60/-60], [-45/45/F(0)/45/-45], and [0/0/F(0)/0/0]. The adhesives were tested using the proposed designs and optimal adhesive which provided adequate strength was EPON862/EPI-CURE3234 15.4% of weight. The thickness of the adhesive layer was investigated, and the thickness of adhesive layer 100 μm was shown the best results in strain transmission from aluminum to the composite carrier. The materials and the fabrication of the composite structures were part of the study in this thesis. One of the materials used in this work was CYCOM®5276-1. This composite material has high Young's modulus in axial direction and it is used in airplane industry. This material was used for the first series of fabrications. This material showed good performance for package lay-up [90/90/F(0)/90/90], 1619 με reading on the composite package for aluminum strain 1955 με in case of the thickness of the adhesive 250 μm, and 1777 με strain reading on the composite package for aluminum strain 2030 με in case of the thickness of the adhesive 100 με. Another laminate design which was close to good performance was [-60/60/F(0)/60/-60] lay-up, 1141 με strain reading on the

composite carrier for aluminum strain 1882 με in case of the thickness of the adhesive layer 250 μm, and 1729 με on the composite carrier for aluminum strain 2078 με in case of the thickness of the adhesive layer 100 μm. Next composite material used in this work was NCT301. This material is weaker than the first composite material, and used for structural applications in sporting goods, marine, medical, and industrial manufacturing. However, NCT301 revealed high compatibility with aluminum in terms of axial strain. The thickness of the adhesion layer was 100 μm for the tensile tests with this material. The best lay-ups as before even with smaller difference between strain readings on composite package and on aluminum sample were [90/90/F(0)/90/90] and [-60/60/F(0)/60/-60]. In case of [90/90/F(0)/90/90] strain reading on the package was 1943 με for aluminum strain 2044 με. Finally, for [-60/60/F(0)/60/-60] lay-up design strain reading on composite carrier was 1892 με for aluminum strain 2039 με. The readings in strain were improved. The strain readings were obtained from electrical strain gauges on the aluminum and on composite package. Static tensile tests were performed by applying axial force on the aluminum sample. The maximum force was 21 kN in order to reach 2000 με. The tests were repeated 3 times for CYCOM®5276-1 material and repeated 6 times for NCT301 composite. The optical sensors were fabricated by depositing aluminum on the tips of the fiber. For uniform and thick layer of aluminum the metallization was repeated three times. Fabricated sensors were embedded inside composite materials. The length of the sensor was around 4 cm. The optical set up was included 2x2 coupler, optical laser source, optical spectrum analyzer. The LabView was used for acquisition of the reflected signals from Michelson interferometer. Optical network did not provide adequate information. The assumptions for lost cycles were

made for calculations of the phase shift. The strain readings from Michelson interferometer were slightly higher for those on the composite package compare to those on aluminum.

Suggestions for future works include more tests of the composite carrier with embedded optical sensor to establish dependence of the designed package sensor on temperature and humidity in any environment.

Contributions:

Three conference articles were written based on the results of this thesis:

1) S. Spitsina, S. V. Hoa, M. Kahrizi, "Design and Fabrication of an Optical Sensor to Monitor Composite Material Structures", proceedings Thirteenth Canadian Semiconductor Technology Conference, August, 2007

2) S. Spitsina, S. V. Hoa, M. Kahrizi, "Design and Fabrication of Optical Sensor/Composite Packaging for Strain Monitoring", IIIrd CREPEC Colloquium, December, 2007

3) S. Spitsina, S. V. Hoa, M. Kahrizi, "Design and implementation of Composite Packages for Optical Sensors to Measure strains in Mechanical Structures", IVth CREPEC Colloquium, December, 2008

- Design of the lay-up in the laminate of the composite package for applications where mechanical structures have low stiffness
- The most appropriate adhesive and adhesive layer thickness

- ANSYS simulations for composite packages with embedded optical fiber using geometry from microscopic observations

REFERENCES

[1] Composite carrier assembly having an encapsulated sensor and an associated fabrication method, by Alexander L. Kalamkarov and Stephen Bruce Fitzgerald (2000, Apr. 4). *Patent 6047094* [Online]. Available: http://www.freepatentsonline.com/6047094.html.

[2] Optical fiber having a Bragg grating in a wrap that resists temperature-induced changes in length, by Peter C. Ogle, CIDRA Corporation. (2002, Oct. 15) *Patent* US 6466716 B1 [Online]. Available: http://www.freepatentsonline.com/ US6466716.html?query=PN/6466716%20OR%20US%206466716%20B1& stemming =on.

[3] Subsea integrity monitoring using fibre optic strain sensors, by D. Roberts. Available: http://www.subseasurveillance.com/integrity_monitoring.aspx, as of 14/04/2008.

[4] B. Glisic and D. Inaudi, "Sensing tape for easy integration of optical fiber sensors in composite structures" [Online]. Available: http://www.smartec.ch/Bibliography, as of 14/04/2008.

[5] Anonymous, Mistras 2001 User's Manual, *"Sensors and Preamplifiers"*, pp. 1-2, 2007.

[6] M. Liu, K. J. Hsia, and J.-K. Shang, "Driving Forces for Interfacial Fatigue Crack Growth by Piezoelectric Actuator", *Journal of Intelligent Material Systems and Structures*, vol. 16, pp. 557-566, 2005.

[7] Anonymous, Strain gauges, *All about Circuits* [Online]. Available: http://www.allaboutcircuits.com/vol_1/chpt_9/7.html, as of 25/03/2008.

[8] I. Balać, M. Milovančević, P. Uskoković, and R. Aleksić, "Stress Field Analysis Around Optical Fiber Embedded in Composite Laminae under Transverse Loading", *FME Translations, vol. 34(1)*, pp. 53-56, 2006. Available: http://www.mas.bg.ac.yu/istrazivanje/biblioteka/publikacije/Transactions_FME/Volume34/1/8.%20Balac%20Igor.pdf as of 3/12/2008.

[9] C. Freudenrich, How Fiber Optics Work, *How Stuff Works* [Online]. Available: http://electronics.howstuffworks.com/fiber-optic.htm as of 11/03/2008.

[10] Anonymous, Optical Fiber, *Answers* [Online]. Available: http://www.answers.com/topic/optical-fiber as of 6/03/2008.

[11] Mr. Zeon, Optical fiber types, *Wikipedia, the free encyclopedia* [Online]. Available: http://en.wikipedia.org/wiki/Image:Optical_fiber_types.svg as of 6/03/2008.

[12] T. G. Giallorenzi, J. A. Bucaro, A. Dandridge, G. H. Sigel, Jr., J. H. Cole, S. C. Rashleigh, and R. G. Priest, "Optical Fiber Sensor Technology", *IEEE transactions on microwave theory and techniques*, MTT-30, vol. 82 (4), pp. 472-511, 1982.

[13] Anonymous, Overview of Fiber Optic Sensors [Online]. Available: http://www.bluerr.com/papers/Overview_of_FOS2.pdf, as of 10/03/2008.

[14] G. Zhou and L. M. Sim, "Damage detection and assessment in fibre-reinforced composite structures with embedded fibre optic sensors – review", *Smart Materials and Structures*, vol. 11, 2002, pp. 925-939, [Online]. Available: http://www.iop.org/EJ/abstract/0964-1726/11/6/314, as of 6/09/2006.

[15] G. B. Hocker, "Fiber-optic sensing of pressure and temperature", *journal of Applied Optics*, vol. 18 (9), pp. 1445-1448, 1979.

[16] C. D. Butter and G. B. Hocker, "Fiber optics strain gauge", *journal of Applied Optics*, vol.17 (18), pp. 2867-2869, 1978.

[17] R. Kashyap and B. K. Nayar, "An All Single-Mode Fiber Michelson Interferometer Sensor", *journal of Lightwave Technology*, vol. LT-1 (4), pp.619-624, 1983.

[18] R. D. Turner, T. Valis, W. D. Hogg, and R. M. Measures, "Fiber-Optic Strain Sensors for Smart Structures", *journal of Intelligent Material Systems and Structures*, vol. 1, pp. 26-49, 1990.

[19] K.-J. Krath, B. Scholl, and H. J. Schmitt, "Fiber Optical Interferometer for Spectral Analysis", *IEEE Photonics Technology Letters*, vol. 4 (2), pp. 206-208, 1992.

[20] L. Yuan and L. Zhou, "Sensitivity coefficient evaluation of an embedded fiber-optic strain Sensor", *Sensors and Actuators*, A 69, pp.5-11, 1998.

[21] T. Valis, E. Tapanes, K. Liu, and R. M. Measures, "Passive-Quadrature Demodulated Localized-Michelson Fiber-Optic Strain Sensor Embedded in Composite Materials", *Journal of Lightwave Technology*, vol. 9 (4), pp. 535-544, 1991.

[22] N. Narendran, A. Shukla, and S. V. Letcher, "Determination of Fracture Parameters Using Embedded Fiber-Optic Sensors", *j. Experimental Mechanics*, pp. 360-365, 1991.

[23] R. McBride, T. A. Carolan, J. S. Barton, S. J. Wilcox, W. K. D. Borthwick, and J. D. C. Jones, "Detection of acoustic emission in cutting processes by fibre optic interferometry", *Meas. Sci. Technol.*, vol. 4, pp. 1122-1128, 1993.

[24] I. B. Kwon, C. G. Kim, and C. S. Hong, "Simultaneous sensing of the strain and points of failure in composite beams with an embedded fiber optic Michelson sensor", *journal Composites Science and Technology*, vol. 57, pp. 1639-1651, 1997.

[25] H. Tsuda, J. Takahashi, K. Urabe, and T. Ikeguchi, "Damage monitoring of carbon fiber-reinforced plastics with Michelson interferometric fiber-optic sensors", *journal of Materials Science*, vol. 34, pp. 4163-4172, 1999.

[26] H. Tsuda, J.-H. Koo, and T. Kishi, "Detection of simulated acoustic emission with Michelson Interferometric fiber-optic sensors", *journal of Materials Science Letters*, vol. 20, pp. 55-56, 2001.

[27] S. L. Loret, P. Rastogi, L. Thevenaz, and D. Inaudi, "Measurement of dynamic deformations using a path-unbalanced Michelson-interferometer-based optical fiber sensing device", *Optical Engineering*, vol. 42 (3), pp. 662-669, 2003.

[28] D.A. Krohn, "Smart Skins and Structures", *Fiber Optic Sensors: fundamentals and applications*, 2nd ed., Instrument Society of America, p.105, 1992.

[29] Y. Zhao and Y. Liao, "Discrimination methods and demodulation techniques for Fiber Bragg grating sensors", *Optics and Lasers in Engineering*, vol. 41 (1), pp. 1-18, 2004.

[30] K.O. Hill and G. Meltz, "Fiber Bragg Grating Technology Fundamentals and Overview", *Journal of Lightwave Technology*, vol. 15 (8), pp. 1263-1276, 1997.

[31] N. Fürstenau, D. D. Janzen, and W. Schmidt, "In-flight strain measurements on Structurally integrated composite plates using fiber-optic interferometric strain gauges", *Smart Mater. Struct.*, vol. 2, pp. 147-156, 1993

[32] D. W. Jensen, J. Pascual, and J. A. August, "Performance of graphite/bismaleimide laminates with embedded optical fibers. Part I: uniaxial tension", *Smart Mater. Struct.* , vol. 1, pp.24-30, 1992.

[33] D. W. Jensen, J. Pascual, and J. A. August, "Performance of graphite/bismaleimide laminates with embedded optical fibers. Part II: uniaxial compression", *Smart Mater. Struct.*, vol. 1, pp.31-35, 1992.

[34] M. Surgeon and M. Wevers, "Static and dynamic testing of a quasi-isotropic composite with embedded optical fibers", *Composites: Part A*, vol. 30, pp. 317-324, 1999.

[35] F. L. Matthews, "Specimen preparation", *Mechanical Testing of Advanced Fibre Composites edited by J. M. Hodgkinson*, CRC Press LLC and Woodhead Publishing Ltd, 2000.

[36] D. A. Krohn, Phase-Modulated Sensors, *Fiber Optic Sensors, Fundamentals and Applications*, second edition, Instrument Society of America, 1992.

[37] D. A. Krohn, *Fiber Optic Sensors, Fundamentals and Applications*, second edition,1992.

[38] M. J. F. Digonnet and B. Y. Kim, Fiber Optic Components, *Optical Fiber Sensors : Principles and Components*, edited by J. Dakin and B. Culshaw, Artech House, inc., 1988.

[39] D. A. Jackson and J. D. C. Jones, Interferometers, *Optical fiber Sensors: Systems and Applications*, edited by B. Culshaw and J. Dakin, Artech House, Inc., 1989.

[40] V. Annovazzi-Lodi and S. Merlo, Single-Mode Fiber-Optic Sensors , *Single-Mode Optical Fiber Measurement : Characterization and Sensing*, edited by G. Cancellieri, Artech House, Inc., 1993.

[41] S. O. Kasap, Wave nature of light, *Optoelectronics and Photonics, Principles and Practices*, Prentice-Hall, Inc., 2001.

[42] S. O. Kasap, Polarization and Modulation of Light, *Optoelectronics and Photonics, Principles and Practices*, Prentice-Hall, Inc., 2001.

[43] Y. Fan and M. Kahrizi, "Characterization of a FBG strain gage array embedded in Composite structure", *Sensors and Actuators A*, vol. 121, pp. 297-305, 2005.

[44] S. O. Kasap, Dielectric Waveguides and Optical Fibers, *Optoelectronics and Photonics, Principles and Practices*, Prentice-Hall, Inc., 2001.

[45] Anonimous, Corning® SMF-28e fiber, Product data sheet [Online]. Available: http://www.corning.com/opticalfiber/products/SMF-28e_fibers.aspx, as of 2/04/2008.

[46] Anonimous, 96% Silica Glass, Material Properties, MatWeb, [Online]. Available: http://www.matweb.com/search/DataSheet.aspx?MatGUID= a028dc09086e4e6f9885e90ae49ecc32, as of 2/04/2008.

[47] Edward E. Tapanes, "Static and Dynamic Strain Measurements within Composite Materials Using a Localized Michelson Fiber Optic Sensor", M. Sc. thesis, University of Toronto, Canada,1990.

[48] J. S. Sirkis and A. Dasgupta, Optical Fiber/Composite Interaction Mechanics, *Fiber Optic Smart Structures*, edited by E. Udd, John Wiley & Sons, Inc., 1995.

[49] O. O. Ochoa and J. N. Reddy, Mechanics of Composite Laminates, *Finite Element Analysis of Composite Laminates*, Kluwer Academic Publishers and copyright Holders, 1992.

[50] J. S. Hansen, Introduction to Advanced Composite Materials, *Fiber Optic Smart Structure*, edited by E. Udd, John Wiley & Sons, Inc., 1995.

[51] Q. Bérnard, M. Fois, and M. Grisel, Tool Preparation in Autoclave Manufactoring of Thermoset Matrix Composites and its Relevance to Adhesion, *journal of Adhesion*, vol. 83 (11), pp. 987-1001, 2007.

[52] C. Zhang, "Random delamination of graphite/epoxy laminated composites: stress, analysis, failure criteria, experimental characterization and stochastic modeling", Ph. D. thesis, Mechanical Engineering, Concordia University, Canada, 2001.

[53] B. Jiang, C. Liu, C. Zhang, B. Wang, and Z. Wang, The effect of non-symmetric distribution of fiber orientation and aspect ratio on elastic properties of composites, *Composites: Part B*, vol. 38, issue 1, pp. 24-34, 2007, [Online]. Available: www.sciencedirect.com, as of 23/06/2008.

[54] Md Ibrahim, "Effect of Notch Size on the Reliability of Composite Laminates Based on Stochastic Finite Element Analysis and Experimental Investigation", M. of Sc. thesis, Mechanical Engineering, Concordia University, Canada, 2005.

[55] James W. Dally, William F. Rilley, Strain-Gage Adhesives and Mounting Methods, *Experimental Stress Analysis*, 3rd edition, McGraw-Hill, 1991.

[56] J. W. Dally and W. F. Riley, Strain-gage adhesives and mounting methods, *Experimental Stress Analysis*, 3rd edition, McGraw-Hill, inc., 1991.

[57] R.T. Cassidy, Acrylics, *Engineered Materials Handbook*, vol.2, ASM Inter-National, 1988.